ABSTRACT

MUKAI, YUSUKE. Inkjet-Printed Wearable Antennas for Hyperthermia Treatment. (Under the direction of Minyoung Suh).

Hyperthermia therapy is a cancer treatment, where body tissue is exposed to heat to damage and kill cancer cells. It has been known that cancer cells are deactivated and killed at the temperature of 40 to 42 °C and higher temperature can cause more damage to cancerous tissue. Heat produced during a hyperthermia treatment can be also beneficial to promote the effects of traditional cancer treatments such as radiotherapy and chemotherapy. The current challenges of hyperthermia treatment include an adequate heating technique with reasonable heat management and longer treatment duration.

The goal of this research was to present an inkjet-printed wearable microstrip patch antennas for a patient-friendly hyperthermia device. To achieve this goal, three research phases were undertaken. The first part of this research aimed to investigate the electrical properties of the inkjet-printed silver ink on the PET film. Because of the high electrical resistivity of the inkjet silver print, additional post-treatment, such as electroless copper plating, salt sintering and UV-flash sintering, were incorporated to reduce the electrical resistivity. The lowest electrical resistivity of 7.5×10^{-8} Ω·m was obtained by the UV-flash sintering, and therefore, the UV-flashed print was selected as the antenna conductor for the further research.

The second part of this research aimed to design, fabricate and evaluate the inkjet-printed microstrip patch antenna. Firstly, the dimension of a 2.45 GHz microstrip patch antenna was calculated with MATLAB® based on the empirical equations. Then, the 3D full-wave electromagnetic field simulation was performed with CST Studio Suite® to optimize the antenna dimension. Next, the microstrip patch antenna was fabricated by the conductive inkjet printing, and the S_{11} of the fabricated antenna was measured by the vector network analyzer.

The fabricated antenna had a S_{11} of -4.8 dB at 2.49 GHz, and this was significantly higher than the simulated S_{11} of -10.3 dB at 2.42 GHz. The factors attributed to the difference between the simulation and measurement included the approximate estimation of the dielectric properties of the substrate and additional resistive loss by silver conductive epoxy paste, and the effects of the dielectric loss were examined with the further simulation.

The last part of this research investigated to see if it was possible to improve S_{11} by reducing conductor loss. Firstly, to facilitate the repetitive printing for better resistance, the antenna dimension was modified to have a wider feed line and gaps. Then, antennas with different conductor thickness were fabricated. The measurement revealed that S_{11} was decreased from -5.2 dB to -5.7 dB by increasing the thickness of the ground plane. Therefore, it was suggested that a thicker conductor could be a one of the possible approaches for a better antenna efficiency.

Inkjet-Printed Wearable Antennas for Hyperthermia Treatment

by
Yusuke Mukai

A thesis submitted to the Graduate Faculty of
North Carolina State University
in partial fulfillment of the
requirements for the Degree of
Master of Science

Textiles

Raleigh, North Carolina

2016

APPROVED BY:

Jacob J. Adams

Xiangwu Zhang

Minyoung Suh
Chair of Advisory Committee

DEDICATION

To Neta

for her support

BIOGRAPHY

Yusuke Mukai was born on February 23rd, 1992 in Osaka, Japan. He received a Bachelor of Engineering degree in Chemistry in March, 2014 from Shinshu University, Nagano, Japan. He joined North Carolina State University in August, 2014 to pursue a Master of Science degree in Textiles. He expects to graduate in May, 2016.

ACKNOWLEDGMENTS

First and foremost, I would like to express my sincere appreciation to my adviser, Dr. Minyoung Suh, whose expertise, understanding, generous guidance and support made it possible to work on a topic of great interest to me. I would also like to extend my sincere appreciation to the members of advisory committee, Dr. Jacob J. Adams and Dr. Xiangwu Zhang, for their valuable advice and kindness to give me the opportunity to work in their laboratories to complete this work.

My appreciation goes to Ms. Judy Elson for assisting me in the operation of the scanning electron microscope. I am thankful to Ms. Teresa White for assisting me in the operation of the thickness tester and stereo microscope. I am grateful to Mr. Vivek Bharambe for assisting me in the operation of the vector network analyzer. I am thankful to Mr. Hasan Shahariar for the valuable discussion. I would also like to thank all my friends who have supported and encouraged me to complete this work. Last but not least, I would like to offer special thanks to my family in Japan.

TABLE OF CONTENTS

LIST OF TABLES

LIST OF FIGURES

Chapter 1 INTRODUCTION

Hyperthermia treatment is a cancer treatment, where cancerous tissue is exposed to heat to shrink cancer tumors. From cytological studies, it has been known that cancer cells are deactivated and killed at the temperature of 40 to 42 °C (Pang, 2016), and higher temperature and longer heating duration can cause more damage to cancerous tissue (Dewey et al., 2009). However, the temperature applied in clinical practice is typically within the range of 42 °C to 45 °C to minimize the damage to normal cells (Soares, Ferreira, Igreja, Novo & Borges, 2012).

Heat produced during a hyperthermia treatment can be beneficial, not only to damage and kill cancer cells, but also to promote the effects of traditional cancer treatments. For example, a number of clinical experiments were performed to examine the effects of hyperthermia treatment combined with radiotherapy (Van der Zee et al. 2000; Hurwitz et al., 2005) and chemotherapy (Tang & McGoron, 2010), concluding that the effects of the traditional cancer therapies can be enhanced by a hyperthermia treatment. Therefore, hyperthermia treatments have been favorably performed along with the traditional cancer therapies (National Cancer Institute, 2011).

Hyperthermia treatment is generally classified into three types based on the size, numbers and locations of cancer tumors: local hyperthermia treatment; regional hyperthermia treatment; and whole-body hyperthermia treatment (National Cancer Institute, 2011). Local hyperthermia treatment targets a small area such as a single tumor (Van der Zee, 2002), and regional hyperthermia treatment targets larger areas of tissue such as a body cavity, organ or rib (National Cancer Institute, 2011). Whole-body hyperthermia treatment targets metastatic cancer tumors which has spread throughout the body (National Cancer Institute, 2011). Each hyperthermia treatment requires a different heating technique to treat tumors adequately.

A hyperthermia treatment is not a new technique. The initial concept of hyperthermia treatment may date back to the 4th century B.C., when Hippocrates treated surface tumors on human skin with a hot iron (Pang, 2016; El-Radhi, Carroll & Klein, 2009). A more reliable record of a hyperthermia treatment can be found in the medical research report by Busch (1866) who observed apparent shrinkage of cancer tumors after a high fever in 1866. In 1935, Warren (1935) reported the favorable effects of artificial temperature on cancer tumors. Despite the long history of application, the progress of hyperthermia treatment in clinics has been largely frustrated by lack of a heating technique (Vernon et al, 1996).

The first issue is the heat management during a hyperthermia treatment. Heat produced during a hyperthermia treatment diffuses to the normal tissue surrounding the cancer tumor, and this makes it difficult to control the heating region. Therefore, it is highly encouraged to attain reasonable heat management during the hyperthermia treatment.

The patient discomfort and treatment duration of hyperthermia treatment is the second issue. The current hyperthermia treatment in clinics impose various types of burden onto patients. For example, radiofrequency hyperthermia (RFHT) and microwave hyperthermia (MWHT) limit the physical mobility of patients during the treatment, and perfusion and ablation techniques are invasive where surgical insertion of a perfusion tube or ablation probe is involved. Therefore, it is highly encouraged to establish a hyperthermia technique which enables a longer and patient-friendly treatment.

With the recent developments in materials science and microwave engineering, microstrip patch antennas have received a great deal of attention for a patient-friendly MWHT (Wang, Yin, Li & Li, 2014). Typically, a microstrip patch antenna is fabricated with printed-circuit-board (PCB) processes. This conventional photolithography method is favorable for its capability to produce mechanically durable and stable structure. In contrast, with the inkjet printing technology, the printing process has become quicker, simpler and higher-resolution at lower manufacturing costs in exchange for lower durability and higher electrical resistivity (Curto, Ramasamy, Suh, & Prakash, 2015).

To incorporate the inkjet printing technology into the antenna fabrication, this research implemented three different experiments. The first experiment aimed to reduce the electrical resistance and resistivity of inkjet-printed silver ink by different post-treatments. In the second part of this research, a 2.45 GHz antenna was designed by 3D full-wave electromagnetic field simulation. Then, inkjet-printed microstrip patch antenna was fabricated and analyzed in comparison between calculated and measured antenna performance. The last part of this research focused on the effects of the conductor thickness on the antenna performance, and the potential of inkjet-printed microstrip patch antennas was discussed for the wearable and patient-friendly hyperthermia application.

Chapter 2 LITERATURE REVIEW

2.1 Hyperthermia Techniques

A number of different heating techniques have been proposed for local, regional, and whole-body hyperthermia treatments. To produce heat at different locations, different strategies have been developed and examined; perfusion heating (National Cancer Institute, 2011), radiofrequency ablation (RFA) (Haemmerich & Wood, 2006; Zorbas & Samaras, 2014), radiofrequency hyperthermia (RFHT) (Ma & Jiang, 2010), microwave ablation (MWA) (Simo et al., 2013), microwave hyperthermia (MWHT) (Ma & Jiang, 2010), magnetically induced interstitial hyperthermia (MHT) (Salunkhe, Khot & Pawar, 2014), and ultrasound hyperthermia (USHT) (Dewhirst et al., 2003; Diederich & Hynynen, 1999). Table 2-1 summarizes the current hyperthermia techniques with the energy generation mechanisms, applicators, favorable tumor locations, and invasiveness. Common operating frequencies of the hyperthermia techniques are shown in Figure 2-1 along with the general definitions of the electromagnetic and acoustic spectra (National Cancer Institute, 2011; Haemmerich & Wood, 2006; Ma & Jiang, 2010; Simo et al., 2013; Dewhirst et al., 2003; Salunkhe et al., 2014; Visser, 2012; Ensminger & Bond, 2011), where lower frequencies generally have less concentration of energy but deeper tissue penetration within the treatment.

Table 2-1. Summary of the current hyperthermia techniques.

Technique	Mechanism	Applicator	Location	Invasiveness
Perfusion	Heating blood	Perfusion	Superficial ~ Deep	Invasive
RFA	Dielectric heating	Electrode	Superficial	Invasive
RFHT	Dielectric heating	Electrode	Superficial ~ Deep	Non-invasive
MWA	Dielectric heating	Unipole antenna	Superficial	Invasive
MWHT	Dielectric heating	Aperture antenna	Superficial	Non-invasive
USHT	Frictional heating	Transducer	Superficial ~ Deep	Non-invasive
MHT	Induction heating	Coil	Superficial ~ Deep	Non-invasive

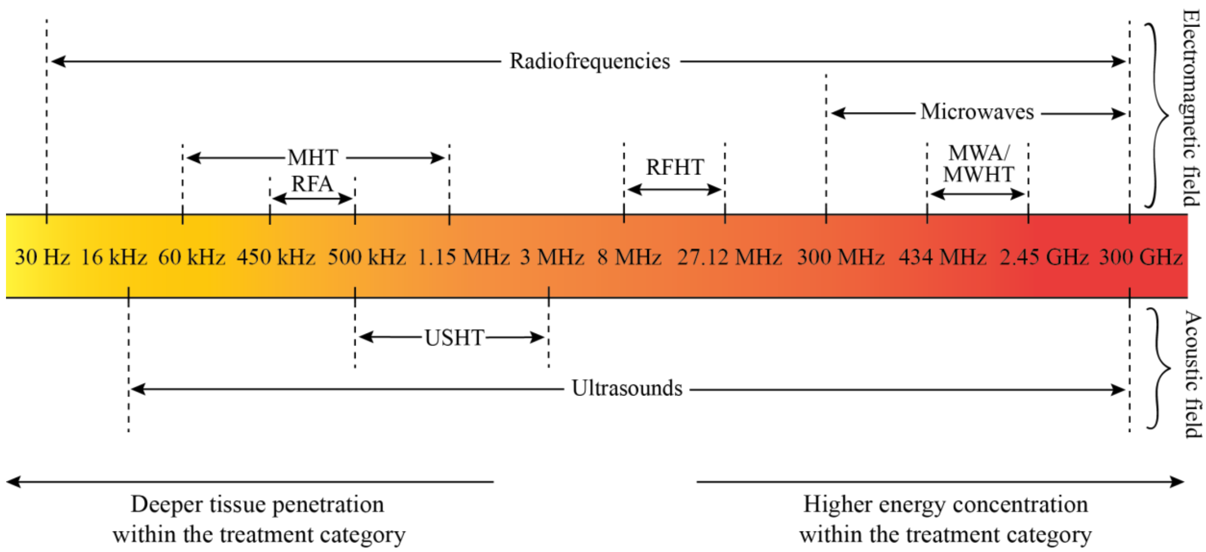

Figure 2-1. Operating frequencies of the current hyperthermia techniques.

2.1.1 Perfusion systems

Perfusion, also known as hemoperfusion, or haemoperfusion, is an external tubing system to heat cancer tumors via blood. In this type of hyperthermia, a patient's blood is removed, heated and perfused back into limb or organ in a series flow (National Cancer Institute, 2011). Advantages of this method include that anti-cancer drugs can be given through blood during perfusion heating, and enhanced effects of the drugs can be expected because of a higher temperature (National Cancer Institute, 2011). In a typical perfusion system, a heating region is difficult to be localized, and therefore, this technique is often chosen for regional and whole-body cancer treatments.

2.1.2 Dielectric-heating systems

Dielectric-heating systems use dielectric heat to treat cancer tumors. In this system, time-varying electric fields, such as radiofrequencies and microwaves, are applied toward cancerous tissue, and heat is produced via ionic conduction and dipolar polarization losses (Figure 2-2) (Kappe, Dallinger & Murphree, 2009). An operating frequency for the high frequency hyperthermia is selected based on the size and location of cancer tumors. For example, lower frequencies tend to produce less heating energy but achieve better penetration of heat into a deep and large tumor (Poulou, Botsa, Thanou, Ziakas & Thanos, 2015; Li, Rong, Jin, Wang & Tang, 2011). On the other hand, higher frequencies can deliver larger amount of energy at a time, and this allows more localized and intensive heating of superficial tumors (Salahi et al., 2012). There are four major hyperthermia techniques categorized in this system.

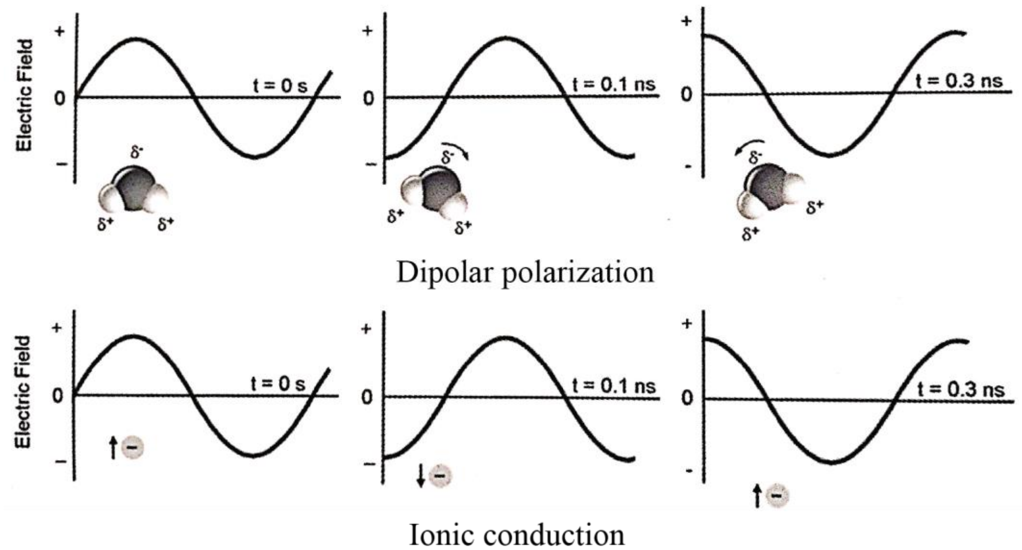

Figure 2-2. Two main heating mechanisms: dipolar polarization and ionic conduction losses. Reprinted from "Practical Microwave Synthesis for Organic Chemists" (p.13), by C. O. Kappe, D. Dallinger & S. S. Murphree, 2009, Darmstadt, Germany: Wiley. Copyright 2009 by Wiley-VCH Verlag GmbH & Co. KGaA.

Radiofrequency ablation (RFA) is an invasive hyperthermia technique to treat a single tumor with radiofrequency electric field. In RFA, an electrically conductive needle (Figure 2-3), called an RFA probe, is inserted into a lesion, and the tissue is heated by 450 to 500 kHz radiofrequency electric field (Haemmerich & Schutt, 2011). A typical RFA procedure requires guidance of medical imaging technology, such as ultrasound imaging, magnetic resonance imaging or computed tomography in order to monitor the surgical insertion of the probe (Ma & Jiang, 2010). Although RFA treats from superficial to deep tumors, it is preferably used to treat bone, kidney, liver, lung and prostate, where the probe has relatively easier access (Society of Interventional Radiology, 2015).

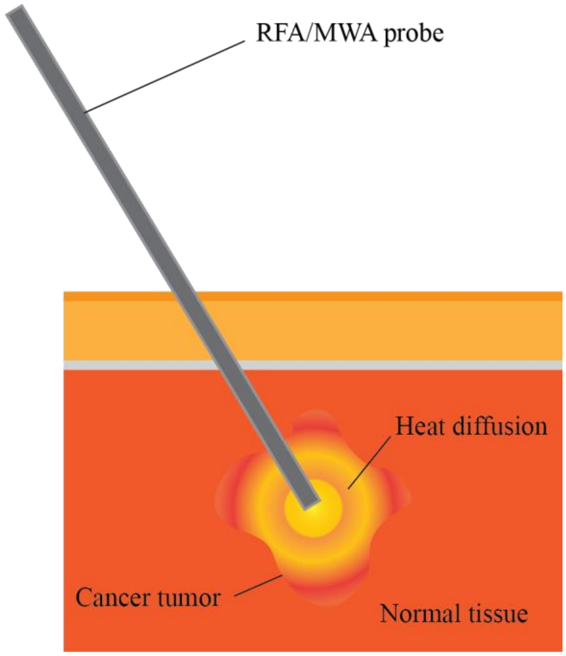

Figure 2-3. RFA/MWA probe surgically inserted into a cancer tumor.
Redrawn from "Nonsurgical Treatments for Metastatic Cancer in Bones" by Society of Interventional Radiology, 2015. Retrieved September 10, 2015, from http://www.sirweb.org/patients/bone-cancer/

Radiofrequency hyperthermia (RFHT) is a non-invasive hyperthermia technique to treat a single or multiple cancer tumors. In RFHT, a pair of parallel-opposed electrodes is placed around target tissue, and 8, 13.56 or 27.12 MHz radiofrequency electric field is applied in order to cause the dielectric heat within the tissue (Ohguri et al., 2011; Ma & Jiang, 2010). With this technique heat is also produced at the electrodes, and therefore, a saline pad or water bolus is usually required in order to cool the skin down (Kim, Hernandez & Lee, 2015; Dewhirst et al., 2003). Figure 2-4 shows a typical RFHT device with a pair of electrodes.

Figure 2-4. Radiofrequency (8 MHz) hyperthermia device (Thermotron RF-8).
Retrieved March 23rd, 2016, from: http://www.vinita.co.jp/medical_div/medical/product/
Copyright 2016 by Yamamoto Vinita Co., Ltd.

Microwave ablation (MWA) is a probe-based local hyperthermia technique similar to RFA. In MWA, a needle-shaped unipole antenna (Figure 2-3) is inserted into a single tumor and typically a 915 MHz or 2.45 GHz microwave is applied to the lesion (Liang, Yu & Yu, 2015). Advantages of MWA include more predictable ablation zone than RFA because of its higher energy concentration (Poulou et al., 2015).

Microwave hyperthermia (MWHT) is a non-invasive local and regional hyperthermia technique. In MWHT, typically a 434 MHz, 915 MHz or 2.45 GHz microwave is emitted from an aperture antenna toward cancerous tissue in order to produce the dielectric heat within the tissue (Ma & Jiang, 2010). Figure 2-5 shows a typical microwave hyperthermia device with an aperture antenna.

Figure 2-5. Microwave (915 MHz) hyperthermia device (Nova KJ-9001). Retrieved March 23, 2016, from: http://f02.s.alicdn.com/kf /HTB1YqGxFVXXXXXBXFXX.PRXFXXX6.pdf. Copyright by Xuzhou Nova Medical Equipment Co., Ltd

2.1.3 Frictional-heating systems

Ultrasound hyperthermia (USHT) is a non-invasive local and regional hyperthermia technique based on frictional heat. In USHT, low-frequency acoustic fields typically within the range of 500 KHz to 3 MHz is applied by an ultrasound transducer toward tumors. Then, the emitted acoustic waves interact with tumor tissue, and frictional heat is produced (Ma & Jiang, 2010). Although the energy produced by the ultrasound is lower than the ones produced by the dielectric heating methods, USHT is advantageous in terms of their excellent penetration into the body composition (Diederich & Hynynen, 1999).

2.1.4 Induction-heating systems

Induction heating systems use the magnetic field and magnetic nanoparticles to produce heat within a tumor. The concept of magnetically induced interstitial hyperthermia (MHT) was originally proposed by Gilchrist et al. (1957) with magnetic materials in 1957, and reintroduced by Gordon, Hines and Gordon (1979) with magnetic nanoparticles in 1979. In MHT, magnetic nanoparticles are accumulated within a tumor either by surgical injection or in a drug delivery system (Figure 2-6), and the magnetic field within the range of 60 kHz to 1.15 MHz (Salunkhe et al., 2014) is applied (Soares et al, 2012; Lee et al., 2011). Then, dissipation of magnetic energy occurs in the form of heat by the magnetic nanoparticles. MHT is especially effective in a local hyperthermia because of its capability of higher heat concentration at the target location (Kozissnik et al., 2013).

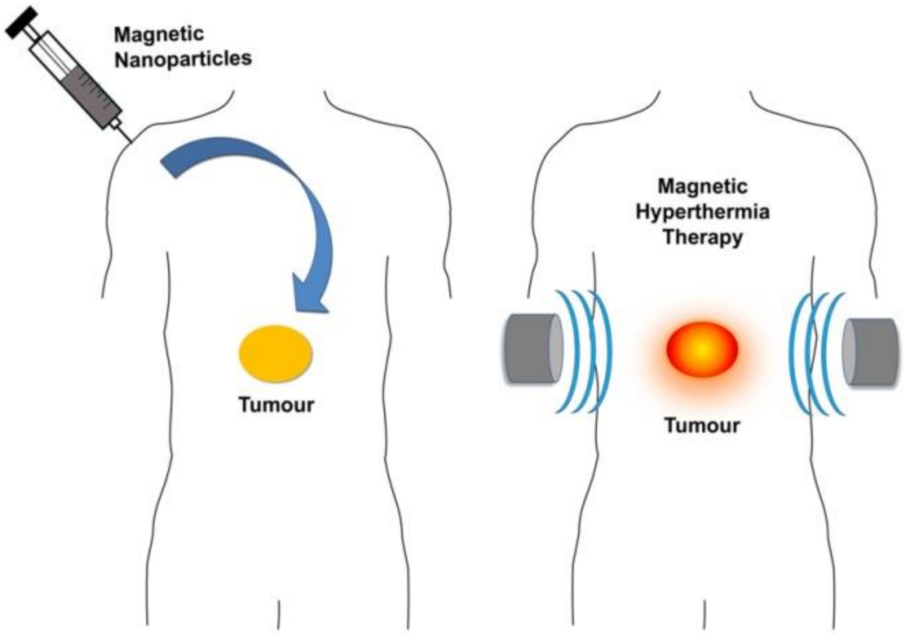

Figure 2-6. Hyperthermia treatment in a magnetic nanoparticle system.
Reprinted from "Coating Nanomagnetic Particles for Biomedical Applications" (p.165) by A. Andrade & R. Ferreira, 2011. In "Biomedical Engineering - Frontiers and Challenges" by R. Fazel (Ed.), Intech Open Access. Retrieved January 5, 2016, from: http://www.intechopen.com/books/biomedical-engineering-frontiers-and-challenges/coating-nanomagnetic-particles-for-biomedical-applications. Copyright 2011 by Intech Open Access.

2.2 Problems in the Current MWHT and Its Solution

Although the current MWHT techniques performed in clinics have the advantages, there are several drawbacks to be addressed. In this section, problems and solutions in MWHT are reviewed.

2.2.1 Limited distance of heat delivery

In MWHT, the microwave cannot propagate to deep tissue due to its short wavelength, and only superficial tumors can be treated. One of the examples to ease the problem is to use a coaxial dipole antenna in a way of endo scope. In this method, an endoscopic coaxial antenna is installed though esophagus, and the antenna emits microwaves toward a cancer tumor (Figure 2-7) (Saito, Takahashi & Ito, 2013). Although this method is only applicable for tumors which can be accessed by a coaxial antenna probe, the organs in deeper locations can be non-invasively treated by microwaves.

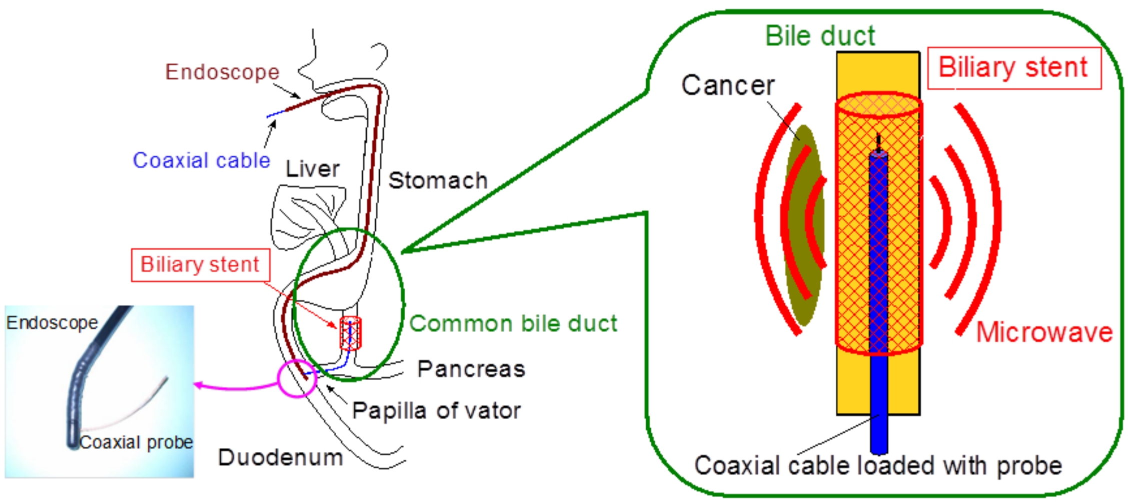

Figure 2-7. Hyperthermia device with a coaxial antenna.
Reprinted from "Microwave thermal therapy using biliary stent fed by coaxial probe" by Ito & Saito Laboratory, 2014. Retrieved December 03, 2014, from: http://www.ap.tu.chiba-u.jp/contents/research/thermal/en Copyright 2014 by Ito & Saito Laboratory.

2.2.2 Patient discomfort and treatment duration

The current devices used in MWHT (Figure 2-5) limit the patient's mobility, and this imposes significant discomfort during the treatment. As a consequence, most of the current hyperthermia treatments can be performed for 30 to 60 minutes to minimize a treatment burden to the patient (Diederich & Hynynen, 1999). However, according to the cytological studies (Dewey, 2009; Dewey et al., 1977), the cellular response to the hyperthermia treatment increases as the duration of the treatment increases (Figure 2-8), and the duration of the current treatment is insufficient. Hence, a hyperthermia technique which enables patients to get treated for a longer period of time with more comfort is highly encouraged for a better treatment result.

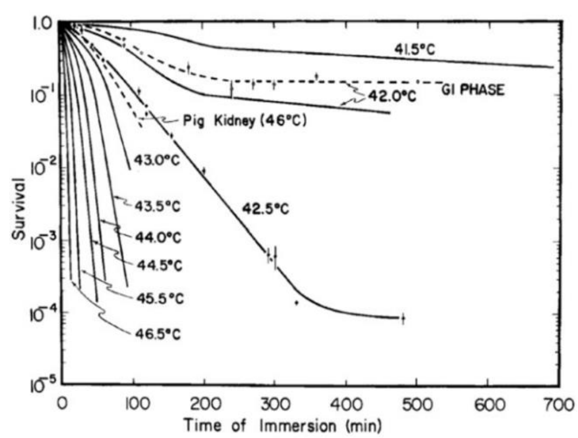

Figure 2-8. Survival curves for asynchronous Chinese hamster ovary (CHO) cells treated at different temperatures for varying lengths of time.
Reprinted from "Cellular Responses to the Combinations of Hyperthermia and Radiation" by W. C. Dewey, L. E. Hopwood, S. A. Sapareto & L.E. Gerweck, 1977, p. 464, Radiology, 123(2), 463–474. Copyright 1997 by W. C. Dewey, L. E. Hopwood, S. A. Sapareto and L.E. Gerweck.

In recent years, flexible and wearable antennas for MWHT have been proposed to ease the current issues associated with the aperture antennas. For example, Topsakal, Asili, Chen, Demirci & Younan (2014) prototyped a PMMA/PDMS-based microstrip patch antenna array operating at 915 MHz. Microstrip patch antennas are compact, and they have an excellent potential for wearable hyperthermia applications.

2.2.3 Heat management

Heat management during a hyperthermia treatment has been largely suffered because of the difficulties in controlling the heating region. For example, MWHT uses the dielectric heat, where the amount of heat production is determined by the dielectric properties of the body composition. Hence, in order to control the temperature, the dielectric properties of the treating regions need to be correctly understood. In a typical MWHT, microwaves travel through the skin, subcutaneous fat, bones, blood, and so on, and these structures of the human body make it challenging to estimate the dielectric properties. In addition, the diversity of patients in gender and age makes it further complicated to standardize the dielectric properties of the body composition.

Over the past few decades, a number of different measurement methods have been established to investigate the dielectric properties of various materials. The measurement methods can be divided into the two categories; non-resonant or resonant methods (Cheng, Ong, Neo, Varadan & Varadan, 2004).

The non-resonant methods such as the transformer technique are involved in measurements at a broad range of frequencies. In this type of method, reflection and/or transmission of EM waves from and/or through a material are measured (Sankaralingam & Gupta, 2010). Although relatively larger sample size is required for the non-resonant methods, advantages include the simplicity of the measurement and the broad range coverage of frequencies. A number of investigations on the dielectric properties of the body tissue have been performed based on the non-resonant systems (Lazebnik et al., 2007; Sugitani et al., 2014).

The resonant methods involve measurements at a single frequency or several discrete frequencies (Cheng, Ong, Neo, Varadan & Varadan, 2004). The common resonant methods include the resonator technique and resonance perturbation technique. The resonator technique appreciates the fact that the resonant frequency and quality factor of a dielectric resonator with given dimensions are determined by its permittivity and permeability, and the resonance perturbation technique is based on the resonance-perturbation theory (Sankaralingam & Gupta, 2010). Although the resonant methods can measure only at discrete frequencies, advantages of the resonant methods include higher accuracy, suitability for low loss materials, and reasonable measurements with small sample size.

2.3 Fabrication Methods of Electrically Conductive Textile Materials

Electrically conductive textile materials can be defined as fibers, yarns, fabrics and polymer films with excellent electrical conductivity. This type of materials has been specifically used in the electronic textile industries for the applications in antennas, sensors, capacitors, actuators, solar cells, wireless communication systems and so on. Due to the increasing needs in electrically conductive textile materials, there are a number of different fabrication techniques established over the past few decades. Currently, there are two major approaches to fabricate electrically conductive textile materials.

2.3.1 Conductive yarns

As one method to fabricate electrically conductive fabrics that combine excellent mechanical properties and electrical properties, conductive wires and yarns such as metal yarns, conductive polymer yarns and carbon nanotube (CNT) yarns have been investigated (Alagirusamy et al., 2013; Lii, Huang, Tsui & Lee, 2002; Fugetsu et al., 2009; Kim et al., 2004; Schwarz et al., 2011). Conductive yarns are further processed by the traditional textile techniques such as weaving, knitting, or embroidery to create electrical conductivity in textile fabrics (Suh et al., 2013).

2.3.1.1 Metal yarns

A metal yarn is a bundle of micro fibers composed of high-conductive metal such as silver, copper, aluminum or gold twisted with polymer fibers. Metal yarns have great advantages due to their structural condition, ability to flex and conform to most desired shapes (Varnaite-Zuravliova, Kavaliauskiene, Baltusnikaite, Valaseviciute & Verbiene, 2014). Having excellent permanent conductivity among all conductive yarns, metal yarns offer a great opportunity to develop a new generation of multifunctional textiles (Lou, 2005; Varnaite-Zuravliova et al., 2014).

2.3.1.2 Conductive polymer yarns

A conductive polymer yarn is a bundle of a polymer fibers that show reasonable electrical conductivity. Since Shirakawa et al. (1977) discovered the first conductive polymer material in 1977, a number of studies have been carried out in the domain of conductive polymers. Until now, various applications and opportunities of conducting polymers such as polyaniline, polythiophene, polypyrrole have been introduced with their unique electric, magnetic and optical properties (Ma et al., 2013). One of the most important properties of conductive polymers is their processability as soft yarns. Conductive polymer yarns have excellent mechanical properties such as flexibility, strechability and bendability, and thus, they can be easily woven, knitted or embroidered by the traditional textile techniques. The current challenges associated with conducting polymers include their limited conductivity and requirements for special manufacturing environment because of their reactivity to oxygen (Cummins & Desmulliez, 2012).

2.3.1.3 Carbon nanotube yarns

A CNT yarn is a bundle of CNT fibers. Since the discovery of CNTs in 1990’s (Krucińska, Wieslawa. & Urbaniak-Domagala, 2011), CNTs have been well recognized for their exceptional mechanical, electronic, photonic and optical properties (Lepró, Lima, &

Baughman, 2010). CNT yarns have been produced by a spinning technique such as forest spinning, direct spinning or solution spinning, where different spinning method gives different properties to the fabricated yarns. Forest spinning is a two-step technique, where carbon nanotubes are firstly aligned vertically to form a “forest”, and carbon nanotube yarns are obtained by pulling out the forest (Park & Lee, 2012). Although relatively long yarns can be obtained in the continuous form, industrial scalability and low reproducibility limit their applications in the industry.

Direct spinning is a one-step technique, where vapor-phase CNTs are directly spun in a similar to the “cotton candy construction” (Park & Lee, 2012). Unlike forest spinning, unlimited length of continuous CNT yarns can be obtained at low cost.

Solution spinning is another technique where CNTs are dispersed in polymer solution, which extruded at high temperature (Jayasinghe et al., 2011; Vigolo et al., 2000). Due to the mixed polymers in the spinning solution, CNT yarns obtained by solution spinning have high level of impurities and marginal alignment, resulting in decreased mechanical and electrical properties (Ericson et al., 2004).

The technologies associated with CNTs are relatively new, and the development of CNT yarn processings are still in its infancy. However, the unique mechanical and electrical features of CNT yarns are highly expected to offer a great potential for the further development of conductive textiles (Foroughi et al., 2012).

2.3.2 Conductive printing

While conductive yarns can be integrated into textile fabrics through the traditional textile techniques, conducting printing is a printing-based technique which can add conductive layers onto fabric and polymer film surfaces. In this section, screen printing and inkjet printing techniques are reviewed.

2.3.2.1 Screen printing

Screen printing is a low-cost printing technique commonly used in the textile industries. Since Vasilantone (1969) filed a patent of a stencil printing machine in 1967, the screen printing had become widely known as an industrial standard in printing.

In a typical screen printing process, a pre-established stencil frame is used for stabilization, and the frame lies on top of the printing substrate (Locher & Troster, 2007). Then, ink is pressed through the stencil by a scraper, allowing precise deposition of ink onto planar and uneven surfaces of substrates (Locher & Troster, 2007).

A wide range of inks can be used in the screen printing, including conductive materials, such as metal nanoparticles (Paul, Torah, Beeby, Yang & Tudor, 2014; Paul, Torah, Beeby & Tudor, 2014; Kazani et al., 2012; Yang, 2013; Locher & Troster, 2007), conductive polymers (Seeberg et al., 2011), carbon nanotubes (CNTs) (Krucińska, Skrzetuska, & Urbaniak-Domagala, 2012; Krucińska et al., 2010), or combination of CNTs and conductive polymers (Khumpuang, Miyake & Itoh, 2011).

Generally, the screen printing can produce very durable and stable print on a wide range of substrates. For example, the screen printing can create excellent water-resistant and abrasion-resistant layers of the printed ink (Kazani et al., 2012). In addition, screen printing is a technique capable of high-volume production in a sequential manufacturing system. Therefore, screen printing techniques have been preferably used to fulfill the industrial needs.

2.3.2.2 Inkjet printing

Inkjet printing is a technique to place ink droplets, which are ejected from a nozzle, onto a desired location of a substrate (Park et al., 2013). Since its introduction in the nineteenth century inkjet printing has become one of the most important techniques in the publishing and graphics industries (Cummins & Desmulliez, 2012). In recent years, inkjet printing has become of increasing interest in organic electronics, nanotechnology, and tissue engineering, in terms of its ability to precisely and spatially control the deposition of various materials on sheet substrates (Romaguera, Madec & Yeates, 2009; Lin et al., 2013). Conductive inkjet printing is a low cost and environment-friendly system to produce conductive ink patterns on a flexible substrate by a low cost inkjet printer. Commonly used conductive inks are categorized into metal nanoparticle inks, conducting polymer inks, graphene inks, carbon nanotube inks and reactive metal inks.

a. Metal nanoparticle inks

Metal nanoparticle inks are the most common inks for conductive inkjet printing. A typical nanoparticle ink is a suspension of metal nanoparticles either in water or organic solvent such as toluene, ethylene glycol or cyclohexanone (Cummins, & Desmulliez, 2012). Silver nanoparticles and copper nanoparticles are the most common nanoparticles in conductive ink.

b. Conductive polymer inks

Conductive polymers, such as poly (3, 4-ethylenedioxythiophene) polystyrene sulfonate (PEDOT: PSS) or polyaniline (PANI), have been used in conductive inkjet printing. Conductive polymers usually show lower conductivity than metals, and require the inert atmospheric conditions due to their high susceptibility to moisture and oxygen during printing process (Cummins & Desmulliez, 2012). However, conductive polymers have potential advantages of being flexible, wearable, and washable, and more resistant to fatigue than the metallic equivalents (Seeberg et al., 2011; Tang & Stylios, 2006). Therefore, conductive polymers are recommended for flexible organic or hybrid electronic devices such as transistors, displays, photovoltaic, cells, electroluminescent lamps and sensors (Perinka et al., 2013).

c. Graphene inks

Graphene is a sheet-structured carbon material. Free electrons in graphene contribute to high electrical conductivity and excellent fatigue properties (Huang, Huang, Liang, Wan & Chen, 2011; Geim & Novoselov, 2007; Bunch, 2007; Li & Kaner, 2008). Unique properties of graphene because of its sheet structure make it of great interest for a wide variety of applications such as transparent conductors, photovoltaic and chemical and biological sensors (Cummins & Desmulliez, 2012).

d. CNT inks

CNTs have high electrical conductivity, high aspect ratio, high strength, small diameter and chemical stability (Lin et al., 2013; Lyth & Silva, 2015). In addition, CNTs are avantageous due to its predefined morphology that simplifies the ink preparation process (Lin et al., 2013). Generally, CNTs are functionalized to disperse in an aqueous solution, and oxidation process is required to establish hydrophilic groups (Lin et al., 2013). CNTs have been widely used for electronic devices.

e. Reactive metal inks

Reactive metal inks are alternative means of metal nanoparticle inks. Inkjet printing of reactive metal inks involves ejections of two different inks which react to form metallized pattern after printed on a substrate (Smith & Morrin, 2012; Cummins & Desmulliez, 2012). In this method, there is no particles present in the ink solutions. Therefore, reactive systems are advantageous in terms that the inkjet printer does not suffer from the nozzle clogging. However, a typical inkjet printing with reactive inks requires several cycles of printing to obtain sufficient conductivity (Petukhov Kirikova, Bessonov & Bailey, 2014). Also, removal of unwanted bi-products on the substrate may be required after printing (Smith & Morrin, 2012).

2.4 Key Factors for Conductive Inkjet Printing

The behavior of ink droplets has an important role in conductive inkjet printing. One of the most important parameters for conductive inks is fluid properties, which determine jettability and resolution of the ink (Cummins & Desmulliez, 2012). Fluid properties are generally characterized by density, dynamic viscosity and surface tension of liquid. For example, Derby (2010) defined the ideal ink fluid properties by characterizing its fluid density (ρ), dynamic viscosity (η) and surface tension (γ) in relation to Reynolds (*Re*), Weber (*We*), and Ohnesorge (*Oh*) numbers, which were:

$$Re = \frac{v\rho a}{\eta} \cdots\cdots\cdots\cdots \text{(Equation 2-1)}$$

$$We = \frac{v^2 \rho a}{\gamma} \cdots\cdots\cdots\cdots \text{(Equation 2-2)}$$

$$Oh = \frac{\sqrt{We}}{Re} = \frac{\eta}{v\rho a^2} \cdots\cdots\cdots\cdots \text{(Equation 2-3)}$$

where v is the velocity and a is the nozzle diameter. Based on these equations, Derby (2010) visualized printable fluid properties (Figure 2-9). Figure 2-9 assesses ink properties by Reynolds, Webber and Ohnesorge numbers, and the printable fluid is defined in the center quadrangle.

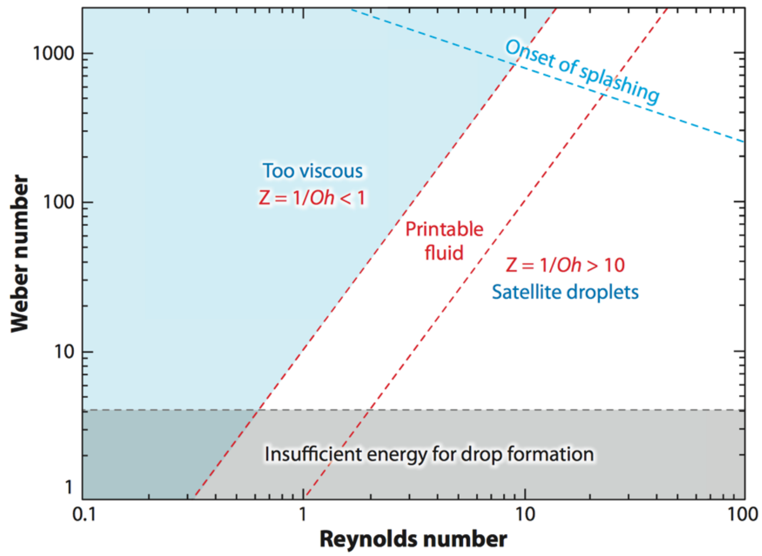

Figure 2-9. Ink parameters.
Reprinted from "Inkjet Printing of Functional and Structural Materials: Fluid Property Requirements, Feature Stability, and Resolution" by B. Derby, 2010, 40(1), 395-414. Copyright 2010 by Annual Reviews.

Surface wettability is another important factor to achieve good print quality in conductive inkjet printing. Wettability of a substrate can be defined as the ratio of hydrophilicity to hydrophobicity. In conductive inkjet printing, wettability of the substrate determines the contact angle of ink and a substrate, affecting final shape and morphology of the print (Park et al., 2013). For example, hydrophilic surface leads to relatively wide pattern widths and hence low resolution, whereas hydrophobic surface yields higher resolution, but hydrodynamic instabilities such as droplet merge and line bulge (Park et al., 2013).

A contact angle of the ink droplet and the substrate surface can be addressed by surface energies. For example, Young's equation (Equation 2-4) describes the contact angle of an ink droplet on a smooth surface (Figure 2-10), and is given by:

$$cos\theta_0 = \frac{\gamma_{SA} - \gamma_{SL}}{\gamma_{LA}} \cdots\cdots\cdots \text{(Equation 2-4)}$$

where θ_0 is the contact angle, γ_{SA} and γ_{SL} are the surface energies of the solid against air and liquid, γ_{LA} is the surface energy of the liquid against air (Ji, H. et al, 2013).

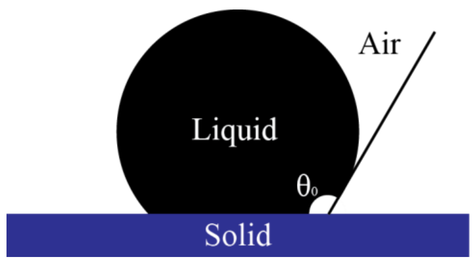

Figure 2-10. Young's model.
Redrawn from "Biomimetic Superhydrophobic Surfaces" (p.2), by H. Ji, G. Chen, J. Hu, M. Wang, C. Ming & U Zhao, 2013, Dispersion Science and Technology, 34(1), 1-21.

In 1936, Wenzel (1936) developed an equation for a rough surface:

$$cos\theta = \frac{r(\gamma_{SA} - \gamma_{SL})}{\gamma_{LA}} = rcos\theta_0 \cdots\cdots\cdots \text{(Equation 2-5)}$$

where θ was introduced as the apparent contact angle in the Wenzel's model and r is the surface roughness factor (Figure 2-11) (Ji et al, 2013). In the Wenzel's model, the surface is filled with liquid, assuming a hydrophilic surface. On the other hand, Cassie (1944) developed an equation for a hydrophobic surface:

$$cos\theta_C = f_S cos\theta_S + f_A cos\theta_A \text{ ·········· (Equation 2-6)}$$

where θ_C is the apparent contact angle in Cassie mode, f_S is the fraction for solid-liquid contacting area, f_A is the fraction for air-liquid contacting area, θ_S is the contact angle for solid-liquid interface, and θ_S is the contact angle for air-liquid interface. In Cassie's theory, the surface was considered a composite surface by assuming vapor pockets to be trapped underneath the droplet (Figure 2-11) (Ji et al, 2013).

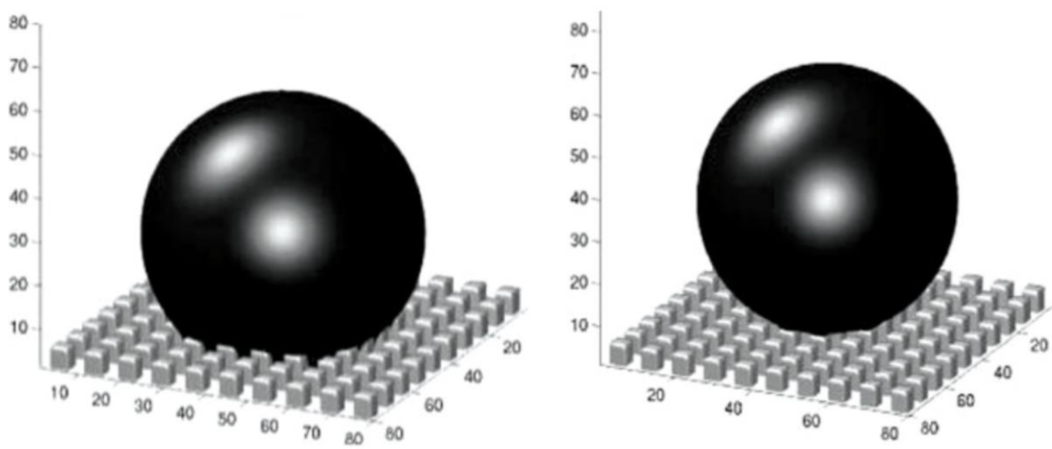

Wenzel's model Cassie's model

Figure 2-11. Wenzel's and Cassie's models.
Reprinted from "Biomimetic Superhydrophobic Surfaces" (p.2), by H. Ji, G. Chen, J. Hu, M. Wang, C. Ming & U Zhao, 2013, Dispersion Science and Technology, 34(1), 1-21. Copyright 2013 by Taylor & Francis Group, LLC.

Wenzel's and Cassie's models have been widely used to control the surface wettability of substrates. For example, hydrophilicity was increased by UV (Olkkonen et al., 2014) or plasma (Petukhov et al., 2014) treatments based on the Wenzel's model, and hydrophobicity was increased by fluorocarbon treatment (Wu et al., 2010; Dalvi & Rossky, 2010) based on the Cassie's model.

Conductive inkjet printing is an emerging technology for simple, low cost and environmental-friendly manufacturing of conductive materials, which may replace the conventional methods such as screen printings. However, conductive inkjet printing involves restrictions in ink and substrate properties, and it is still in its infancy to inkjet-print conductive ink on fabrics and polymer films. There are still issues to be resolved, such as low ink adhesion, nozzle clogging and high electrical resistivity.

2.5 Sintering

Sintering, also known as curing, is a chemical process to bond contacting particles into a solid object (German, 2014). When metal nanoparticle ink is deposited onto a substrate by an inkjet printer, metal nanoparticles form tangential contact to each other and air is trapped between the nanoparticles (Figure 2-12). Hence, electrical resistivity of inkjet-printed metal nanoparticles is much higher than the one of their bulk equivalents. In order to obtain electrical resistivity close to the intrinsic electrical resistivity of the bulk material, sintering is required to coalesce metal nanoparticles (Figure 2-12) (Volkman et al., 2011; Magdassi, Grouchko, Berezin & Kamyshny, 2010; Qin. & Watanabe, 2014; Layani et al., 2012; Ma, 2014; Cauchois et al., 2011).

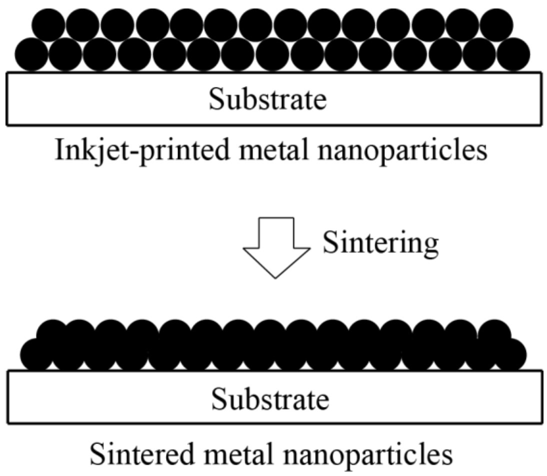

Figure 2-12. Sintering of inkjet-printed metal nanoparticles.

In the early models of the solid-state sintering analysis (German, 2010), the neck size between two identical spheres has been investigated, where the size of the neck becomes 1.26 times larger than the original sphere diameter after complete sintering (Figure 2-13). Based on the measurements of the neck area in the thermodynamic experiments, it was revealed that the rate of particle coalescence depends on the temperature, the material properties and the particle size. Smaller particles and higher temperature can lead to faster sintering (Li & Pan, 2012).

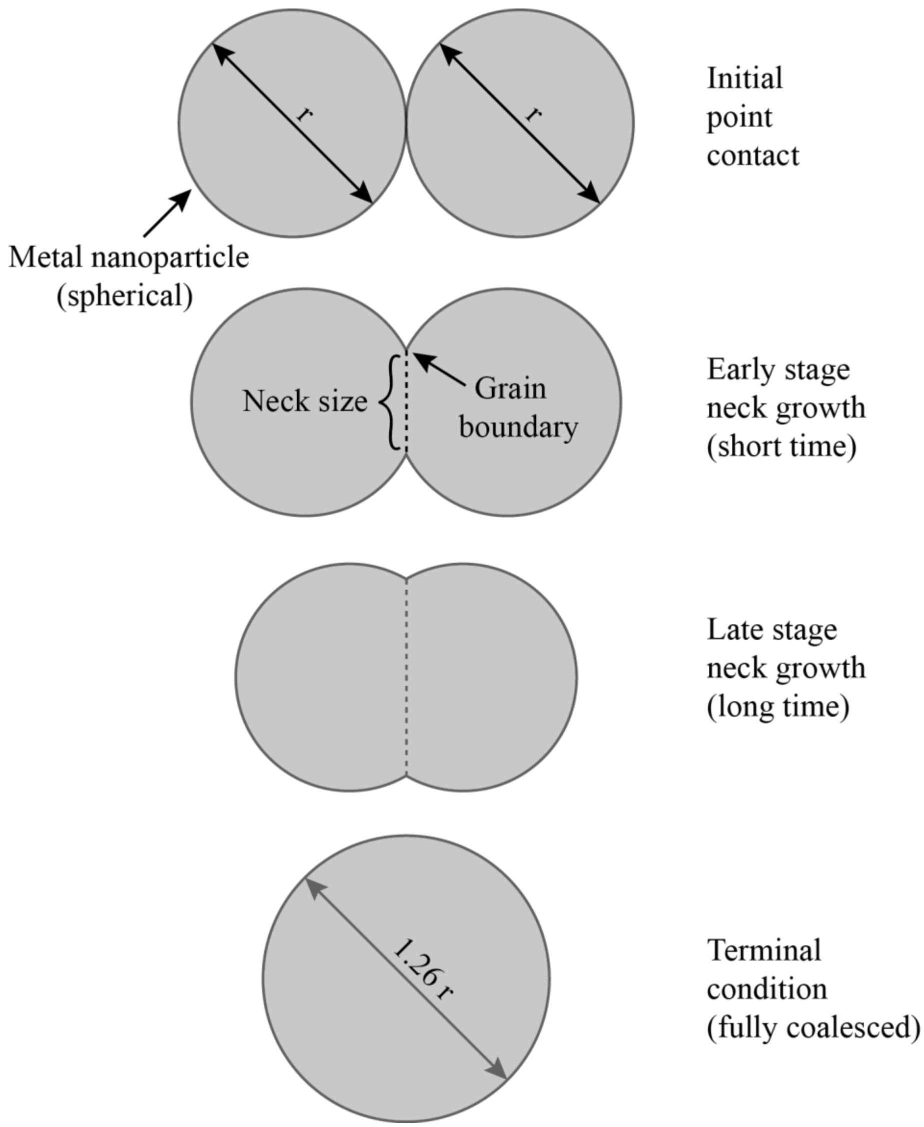

Figure 2-13. Sintering mechanism of two metal nanoparticles.
Redrawn from "Thermodynamics of Sintering" (p.6), by R. M. German. In "Sintering of Advanced Materials" by Z.Z. Fang (Ed.), 2010, Cambridge, UK: Woodhead.

Further investigations on the sintering phenomena (Rahaman, 2010) revealed that sintering at solid-state occurs at least in six steps (Figure 2-14): surface diffusion, lattice diffusion from the surface, vapor transport (vaporization/solidification), grain boundary diffusion, lattice diffusion from grain boundary, and plastic flow, where the later stage of the sintering (i.e., grain boundary diffusion, lattice diffusion from the grain boundary, and plastic flow) are associated with densifcation. On the other hand, the earlier stage (i.e., surface diffusion, lattice diffusion from the surface and vapor transport) occur without densifcation, concluding that a porous structure is produced when the non-densifying mechanisms dominate, and a dense structure is favourably produced when the densifying mechanisms dominate (Rahaman, 2010).

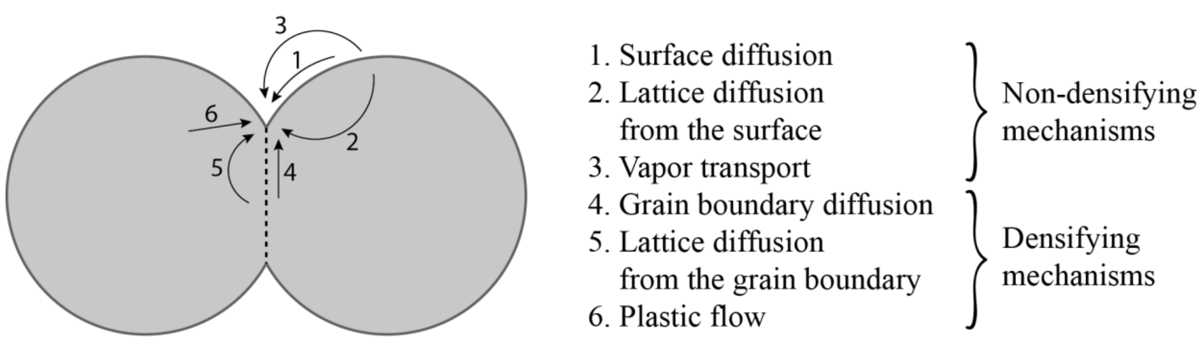

Figure 2-14. Sintering mechanism in 6 steps.
Redrawn from “Kinetics and Mechanism of Densification” (p.35), by M. N. Rahaman. In “Sintering of Advanced Materials” by Z.Z. Fang, 2010, Cambridge, UK: Woodhead.

Although the removal of free surface area within the particles also contributes to the reduction of surface energy, this does not guarantee the complete coalescence of the particles (German, 2010). Therefore, external force is almost always required to drive the densification process. In a common sintering process of printed metal nanoparticles, heat or chemical energy is applied to facilitate the grain growth, and this also promotes a greater mechanical adhesion of the printed metal nanoparticles to the substrate (Cummins. & Desmullliez, 2012).

2.5.1 Thermal sintering

Thermal sintering is a heating technique to sinter metal nanoparticles. Common thermal sintering techniques are convection oven sintering, microwave sintering, spark plasma sintering (SPS) and UV sintering.

One of the most traditional way of sintering metal nanoparticles is the convection oven sintering. In this method, sintering takes place under the circulation of heated air providing the constant temperature. The convection oven sintering process usually takes a long time because the coalescence of metal nanoparticles occurs at slow speed. High temperature typically within the range of 100 to 300 °C is required for the convection oven sintering, and only heat-resistant substrate can be treated.

Due to the increasing demand for a rapid sintering method, microwave sintering has been introduced (Cauchois et al., 2011; Perelaer et al., 2009). In this method, heat is instantly produced by microwaves, contributing to short sintering duration. Microwave sintering is only applicable when the substrate does not affect to microwaves. If the substrate transmits microwaves, localized sintering on printed metal nanoparticles can be achieved, and damage to the substrate can be minimized (Cummins & Desmullliez, 2012; Perelaer et al., 2012).

Spark plasma sintering (SPS) is another rapid sintering method based on the resistive heating. In this method, a voltage is applied to produce an electrical current, and the resistive heat is produced within the printed track (Ma et al., 2013). This type of direct heating enhances densification over the grain growth, and enables very high heating and cooling rates (Suarez. et al., 2013). Because conductive regions are selectively heated, damage to the substrate is minimized. This method allows applications to heat-sensitive substrates, such as paper, textile fabrics and polymer films.

UV sintering is a photonic sintering based on the UV radiation. UV light ranging from 200 to 400 nm is known to induce effective coalescence of metal nanoparticles due to its high energy capacity. UV sintering has been widely used in the field of printed electronics, where short processing time, efficient energy delivery, and localized heat load are expected (Sandmann, Notthoff & Winterer, 2013).

UV-flash sintering is a recently developed sintering technique based on the UV-pulse. In this method, substrate is exposed to intense energy bursts of UV radiation for a very short time (< 1 sec), and the coalescence is instantly achieved (Dharmadasa, Dharmadasa & Druffel, 2014). Therefore, the damage to the substrate is minimized and a wide range of heat-sensitive substrates such as paper, polymer films and textile fabrics can be treated.

2.5.2 Electrolyte sintering

Electrolyte sintering is a chemically driven sintering method by the physical contact of metal nanoparticles with a solution of electrolytes. In this method, printed metal nanoparticles are either dipped in or covered with an electrolyte solution. During electrolyte sintering, electrical charges on electrolytes softens metal nanoparticles, enhancing coalescence of printed metal nanoparticles (Magdassi et al., 2010).

Recently, inorganic salts such as sodium chloride and magnesium chloride solutions have been reported to have the ability to decrease electrical resistance of printed silver nanoparticles (Zapka, Voit, Loderer & Lang, 2008; Layani et al., 2012). The mechanism to decrease electrical resistivity was not clearly explained by Zapka et al. (2008), but it was suggested that the effects of the electrolyte solutions in the sintering process was based on the electrical charges at the surface of the printed silver nanoparticles by Magdassi et al. (2010). One of the advantages of this method is that the coalescence of silver nanoparticles can take place at the room temperature. Although the mechanism of electrolytes in sintering has not been understood, salt sintering has received a great deal of interest because of its simple way of treating printed metal nanoparticles.

The use of polyelectrolyte was introduced by Magdassi et al. (2010) as a room-temperature sintering agent to induce coalescence of printed metal nanoparticles. According to Magdassi et al. (2010), polydiallyldimethylammonium chloride (PDAC) solution was reported to have the ability to lower electrical resistivity of printed silver nanoparticles. The proposed mechanism of polyelectrolyte sintering is similar to the one for the salt sintering, where coalescence of printed silver nanoparticles is induced by electrical charges of electrolytes (Magdassi et al., 2010).

2.6 Electroless Plating

Electroless plating is a chemical plating technique, which involves the deposition of metal nanoparticles from a plating solution onto surfaces without applying electric voltage or external energy (Chang, Chang & Liang, 2014). The driving force for the reduction of metal ions and their deposition on a substrate is supplied by a reducing agent and ionization energy.

To initiate deposition of metal nanoparticles on a non-conductive substrate, the substrate surface is firstly treated by a sensitizer such as an aqueous solution of tin dichloride (Mallory & Hajdu, 1990). This allows the deposition of the sensitizer (Sn^{2+}) on the substrate, and the sensitized substrate can now work as a reaction site for metal deposition (Figure 2-15). Once the metal layer starts being formed on the substrate, the deposited metal nanoparticles begin functioning as a reaction site for sequential metal deposition (auto-catalytic reaction) (Figure 2-15). The auto-catalytic reaction continues as long as the plating solution is supplied.

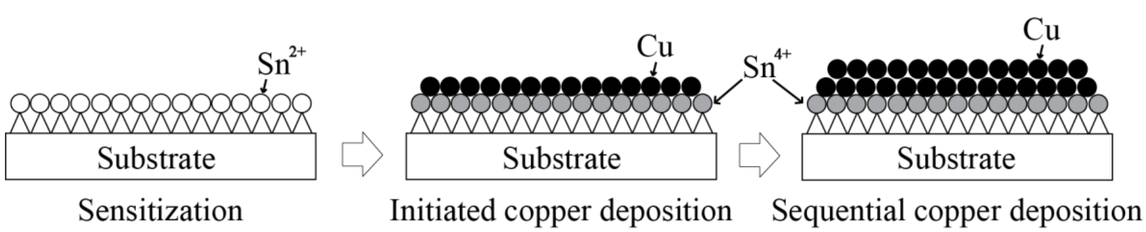

Figure 2-15. Sensitization and electroless plating of non-conducting substrate. Redrawn from "Electrochemistry at the Nanoscale" (p. 291) by P. Schmuki & S. Virtanen, 2009, New York, NY: Science+Business Media, LLC.

When compared to conventional electroplating methods, electroless plating has several advantages. For example, uniform thickness of nano- or micro-scale plating can be achieved through electroless plating, while non-uniform current distribution in the plating cell can cause non-uniform plating during electroplating (Ghali, 2010). In addition, in electroless plating the speed of deposition and the layer thickness can be easily controlled by adjusting the concentration, pH, temperature of the plating solution and plating duration. Also, the location of the deposition can be controlled by designating the sensitizing area on the substrate. Furthermore, electroless plating often results in desirable characteristics including less porosity and more corrosion resistance (Wei & Roper, 2014). Therefore, electroless plating has been used in a wide variety of fields such as the chemical processing industry, food industry, oil and gas industry, automotive industry, aerospace industry and electronics industry (Parkinson, n.d.).

Recently, it was claimed that electroless plating can be directly applied on inkjet-printed silver print (Kao & Chou, 2007). In the proposed process, inkjet-printed silver nanoparticles were dipped in a plating bath containing copper cations (Cu^{2+}) and a reducing agent, triggering auto-catalytic deposition of copper. Kao (2007) reported that the electrical resistance of the inkjet silver print was significantly decreased by electroless copper plating.

2.7 Antennas

With the booming of wireless communications as a driving force, the field of antenna engineering has undergone significant breakthroughs with the numerical electromagnetic modeling techniques (Chen & Wang, 2015). As a result, antennas have been used in a wide range of applications including computer and internet wireless communications, civil infrastructure systems, space and aircraft engineering, and medical and health care devices. In this section, history, concepts and theories of antennas are reviewed.

2.7.1 Fundamental concepts of antenna

In 1864, James Clark Maxwell predicted the existence of electromagnetic (EM) waves (Pelosi, 2014). Since then, EM waves have been the core technology in the areas of telecommunication, wireless network system, GPS, sensors, radars, and other appliances, where antennas are used as a device to transmit and/or receive EM waves (Collin, 2001).

An antenna is defined as ‘a means for radiating or receiving radio waves’ by the IEEE standard definition (IEEE Standard 145, 1983), and Balanis (2005) translated this into “the transitional structure between free-space and a guiding device” (Figure 2-16). Therefore, antenna is a device to transmit or receive EM waves.

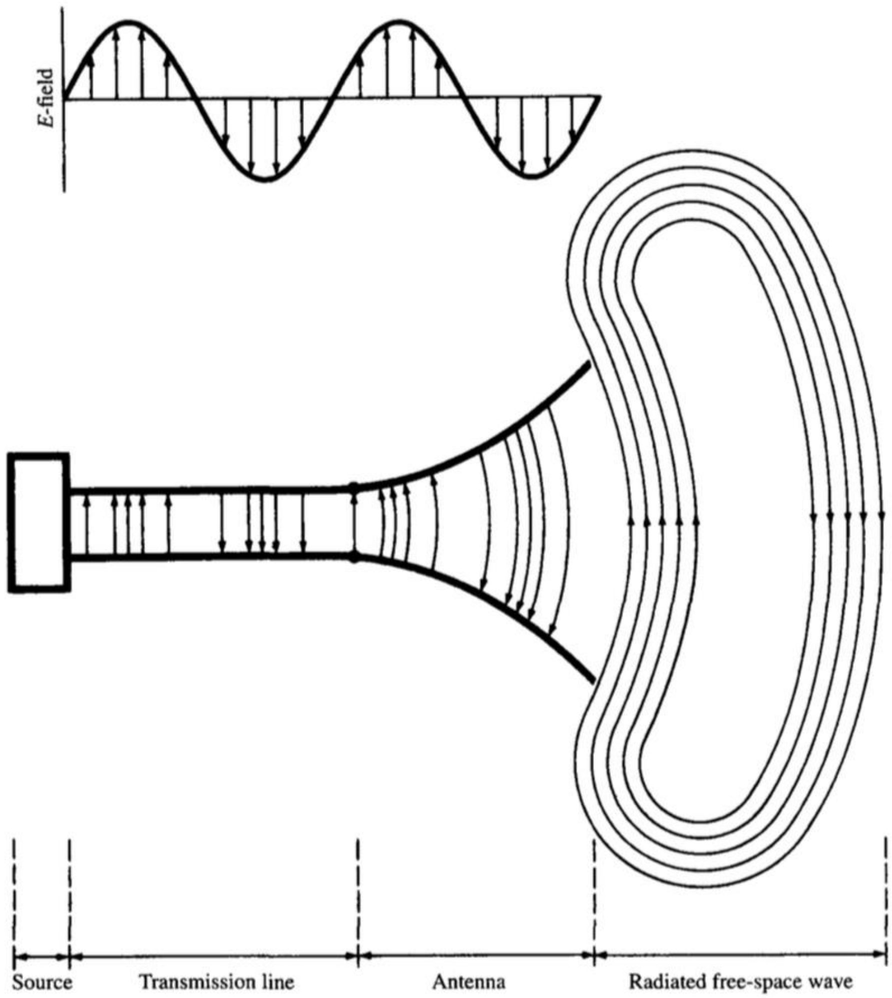

Figure 2-16. “Antenna as a transition device”.
Reprinted from “Antenna Theory: Analysis and Design” (p.12), by C. A. Balanis, 2005, Hoboken, NJ: Wiley. Copyright 2005 by John Wiley & Sons, Inc.

2.7.2 Skin effect

Skin effect is a phenomenon where electric current prefers to flow along the surface of a conductor at higher frequencies. While direct current flows uniformly through a conductor in D.C., the density of alternating current drops off exponentially from surfaces at higher frequencies (Figure 2-17). If electric current density in a conductor is represented by $\vec{J}$, then:

$$\vec{J} = \text{constant} \qquad \text{in D.C. conduction} \cdots\cdots\cdots \text{(Equation 2-7)}$$

$$\vec{J} = \vec{J}_s e^{-\frac{d}{\delta}} \qquad \text{in A.C. conduction} \cdots\cdots\cdots \text{(Equation 2-8)}$$

where $\vec{J}_s$ is the current density at the surface of the conductor, *d* is the distance from the surface toward the center of the conductor, and δ is the skin depth (Brooks, 2009).

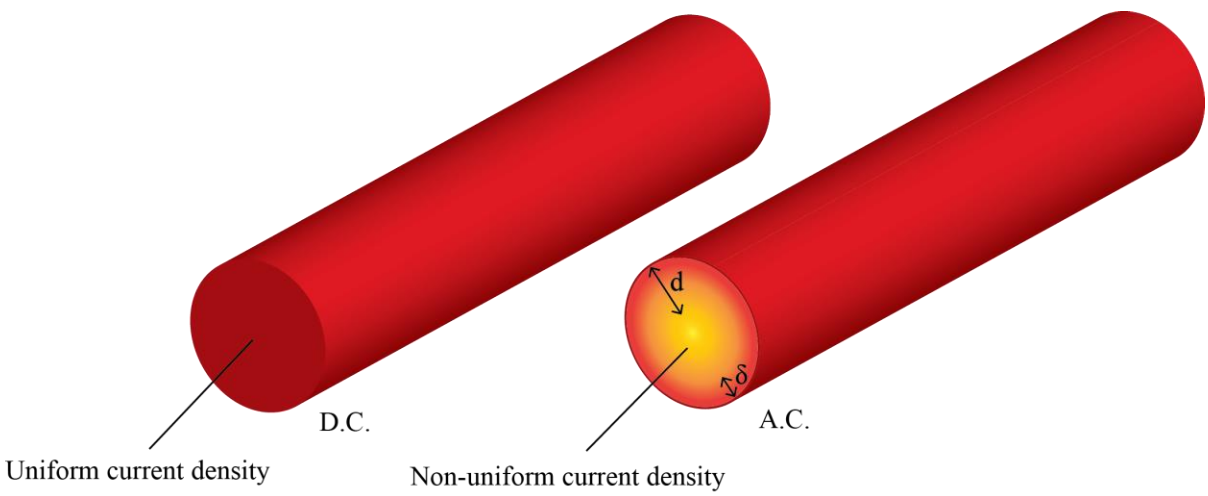

Figure 2-17. Schematic cross sections of cylindrical conductors in D. C. and A. C. Redrawn from "Engineering Electromagnetics" (p.640), by N. Ida, 2015, New York, NY: Springer.

The skin depth is the distance where $J = J_s e^{-1}$, and is given by:

$$\delta = \sqrt{\frac{\rho}{\pi f \mu_0 \mu_r}} \cdots\cdots\cdots \text{(Equation 2-9)}$$

where μ_r is the relative magnetic peameability of the conductor, μ_0 is the permeability of free space, f is the frequency of the current, and ρ is the electrical resistivity of the conductor (Glisson, 2011). As Equation 2-9 suggests that the skin depth decreases with higher frequency, signal loss due to the skin effect should be considered at higher frequencies.

2.7.3 Antenna types

Wire antennas, linear or curved, are the oldest type of antennas having a simple structure both electrically and mechanically. Although gain obtained with wire antennas are small when the space available for antennas is limited, wire antennas are probably the most popular antennas often used in automobiles, buildings, ships, aircrafts, space crafts, and so on (Balanis, 2005).

Traveling-wave antennas such as beverage antennas, rhombic antennas and Yagi-Uda antennas are a class of antennas which uses a traveling wave on a guiding structure as the main radiating mechanism (Losito & Dimiccoli, 2012). This type of antennas shows a high gain, and therefore, traveling-wave antennas are suitable for the application in TV antennas and military radars.

Reflector antennas are widely used in radio astronomy, deep-space communication, microwave communication and satellite tracking because of their very high gain (Balanis, 2005). Parabolic antennas, also known as satellite dish antennas, and corner reflector antennas are classified into this category.

Log periodic antennas such as conical metal strip antennas are wideband antennas, which exhibit essentially constant characteristics over the frequency range (Balanis, 2005). This type of antennas has specific applications such as power short wave broadcasting, and electromagnetic compatibility measurements, where it is required to receiver a wide range of frequencies.

Aperture antennas such as horn antennas and waveguides (Figure 2-18), are wide-band antennas with a simple structure due to the absence of resonant elements. Aperture antennas are preferably used in the application such as the aircraft and the space craft, where antennas are mounted on the surface of the craft body and covered with dielectric material for its protection from environmental hazards (Balanis, 2005).

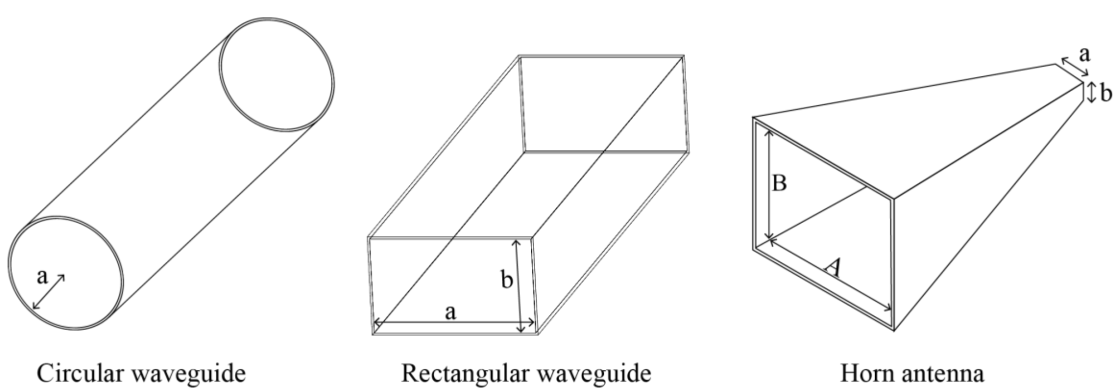

Figure 2-18. Schematic diagrams of aperture antennas.

A microstrip patch antenna is a microstrip radiator printed on a grounded low-permittivity substrate, and feeding is achieved either via microstrip or through coaxial cable with an inner conductor which terminates on the patch (Elliott, 2003). Microstrip patch antennas can be any shape, but regular geometric shapes such as rectangles (Figure 2-19) or circular discs are most commonly used (Elliott, 2003). Microstrip patch antennas are an essentially bi-directional antennas, and they are configured using a back reflector (Zubir, Rahim, Ayop & Majid, 2010).

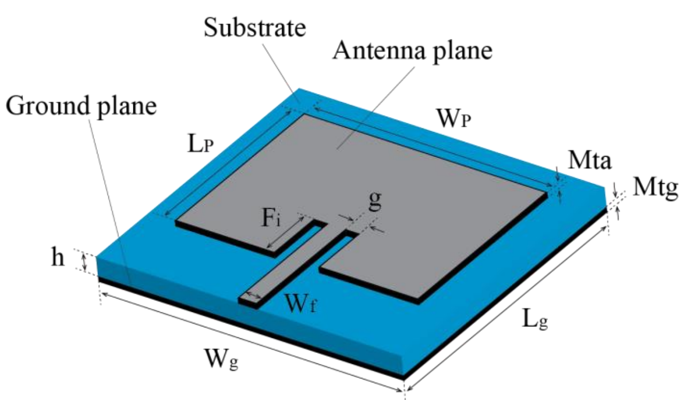

L_P	Length of the antenna plane
W_P	Width of the antenna plane
W_f	Width of the feed line
g	Gap of the feed line
F_i	Inset feed point
h	Height of the substrate
L_g	Length of the ground plane
W_g	Width of the ground plane
Mta	Thickness of the antenna plane
Mtg	Thickness of the ground plane

Figure 2-19. Schematic diagram of a rectangular microstrip patch antenna.

An array antenna is a set of connected individual antennas, and used when radiation characteristics cannot be achieved by a single element. The elements are generally arranged in a way that the radiation from the elements adds up to yield the maximum in particular directions, and/or minimum in others, as desired (Balanis, 2005). Figure 2-20 shows an example of a typical antenna array composed of microstrip patch antennas.

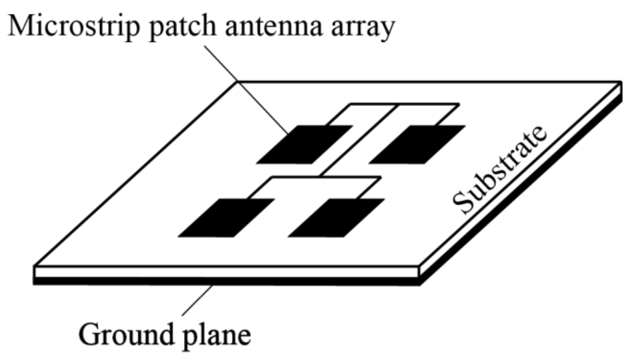

Figure 2-20. Schematic diagram of a microstrip patch antenna array.

2.7.4 Microstrip patch antennas

The concept of the microstrip patch antenna may date back to 1950s when Grieg & Engelmann (1952) introduced a transmission technique with a microstrip line (Figure 2-21). The earlier microstrip lines and patch antennas were specialized devices developed in laboratories, because there was no commercially available printed circuit boards or adequate substrates with controlled dielectric constants at that time (Bancroft, 2009).

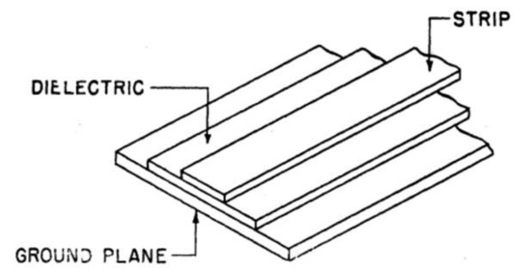

Figure 2-21. Schematic diagram of a microstrip transmission line.
Reprinted from “Microstrip-A New Transmission Technique for the Kilomegacycle Range” by D. D. Grieg and H. F. Engelmann, 1952, Proc, IRE, 40(12), p. 1645. Copyright 1952 by D. D. Grieg and H. F. Engelmann.

These days, microstrip patch antennas become more available in various applications. Especially, with the development in the printing technologies and polymer engineering, the topic of wearable wireless systems with the microstrip patch antenna has received a great deal of interest with expectations to fulfill the psychological, physical, functional, and managerial requirements (Suh, 2011; Suh et al., 2013). Microstrip patch antennas are beneficial to such applications because of their easy impedance matching, fabrication simplicity and low profile, in the sense that the substrate can be fairly thin and bent easily to conform to a curved surface (Losito & Dimiccoli, 2012). On the other hand, drawbacks of the microstrip patch antenna include narrower bands with lower efficiency compared with the other types of antennas (Balanis, 2005).

Rectangular microstrip patch antennas are probably the most popular microstrip patch antenna implemented in diverse R&D sectors, and a numbers of full-wave analysis methods have been devised for rectangular microstrip patch antennas (Bancroft, 2009). However, the full-wave models require a considerable investment in time and effort, and thus, not convenient for computer-aided design (CAD) implementation (Bancroft, 2009). There are two simplified models conveniently used to design rectangular microstrip patch antennas.

2.7.4.1 Transmission-line model

The transmission-line model is the simplest and easiest model used for analysis of the rectangular microstrip patch antenna. The transmission-line model gives less accurate results than the other models (Balanis, 2005), but it gives great physical insight.

In the transmission-line model radiation originates from the fringing electric field at the either end (radiating slots) of the antenna (Figure 2-22 & Figure 2-23). Hence, the fringing at the edges makes the length of the microstrip antenna electrically longer than its physical dimension (Bancroft, 2009), and the elongated length is called the effective length (L_{eff}). In addition, a part of the fringing electric field is created outside the substrate, and this lowers the dielectric constant of the substrate (Bancroft, 2009), and the lowered dielectric constant is called the effective dielectric constant (ε_{reff}).

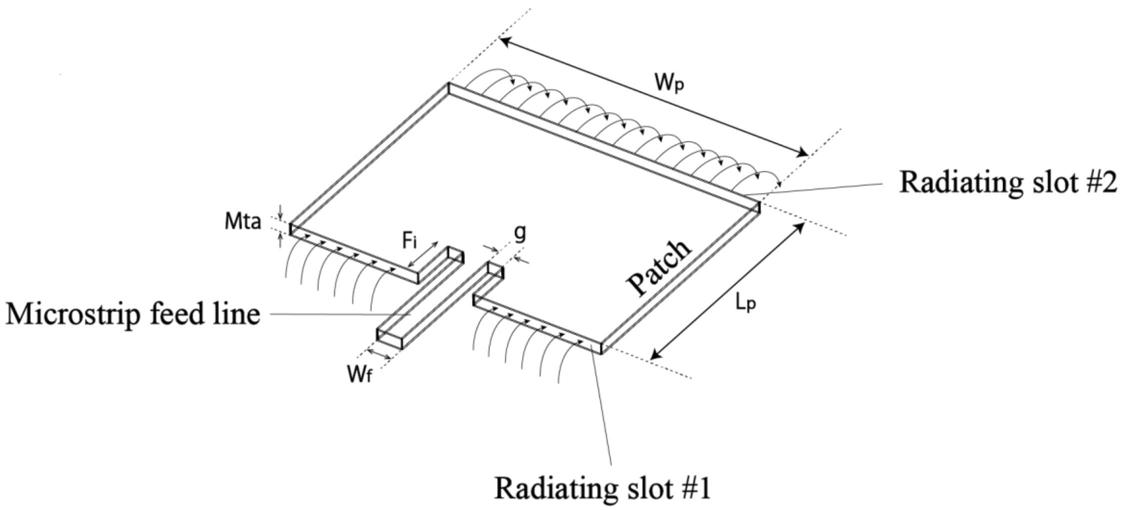

Figure 2-22. Rectangular microstrip patch antenna in the transmission-line model.
Redrawn from "Microstrip and Printed Antenna Design" (p. 11) by R. Bancroft, 2009, Raleigh, NC: SciTech.

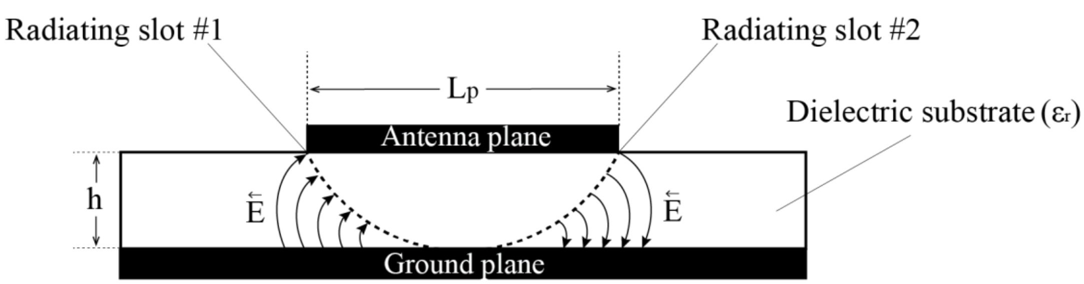

Figure 2-23. Cross section of a rectangular microstrip patch antenna in the transmission-line model.
Redrawn from "Antenna Theory: Analysis and Design" (p.812) by C. A. Balanis, 2005, Hoboken, NJ: Wiley.

In the transmission-line model, the width of the patch (W_p) is given by:

$$W_p = \frac{C}{2f_o\sqrt{\frac{\varepsilon_r+1}{2}}} \cdots\cdots\cdots \text{(Equation 2-10) (Bahl \& Bhartia, 1980)}$$

where f_o is the operating frequency, ε_r is the dielectric constant of the substrate, and *C* is the speed of light in vacuum. The length of the patch (L_p) is given by:

$$L_p = L_{eff} - 2\Delta L \cdots\cdots\cdots \text{(Equation 2-11) (Hammerstad, 1975)}$$

where L_{eff} is the effective length of the patch and ΔL is the extension of the length by the fringing effect. The effective length of the patch (L_{eff}) is given by:

$$L_{eff} = \frac{C}{2f_o\sqrt{\varepsilon_{reff}}} \cdots\cdots\cdots \text{(Equation 2-12) (Kumar \& Ray, 2003)}$$

where ε_{reff} is the effective dielectric constant of the substrate. The effective dielectric constant of the substrate is given by:

$$\varepsilon_{reff} = \frac{\varepsilon_r+1}{2} + \frac{\varepsilon_r-1}{2}\left(1+12\frac{h}{W_p}\right)^{-\frac{1}{2}} \quad \text{for } \frac{W_p}{h} > 1 \cdots\cdots\cdots \text{(Equation 2-13) (Balanis, 1989)}$$

where h is the height of the substrate. The extension of the length to each direction is given by:

$$\Delta L = 0.412h\frac{(\varepsilon_{reff}+0.3)\left(\frac{W_p}{h}+0.264\right)}{(\varepsilon_{reff}-0.258)\left(\frac{W_p}{h}+0.8\right)} \cdots\cdots\cdots \text{(Equation 2-14) (Hammerstad, 1975)}$$

The resonant input impedance (Z_{in}) is given by:

$$Z_{in} = R_{in} = \frac{1}{2G} \cdots\cdots\cdots \text{(Equation 2-15) (Balanis, 2005)}$$

where R_{in} is the resonant input resistance and G is the conductance of the slot. The conductance is given by:

$$G = \frac{W_P}{120\lambda_0}\{1 - \frac{1}{24}(k_0 h)^2\} \cdots\cdots\cdots \text{(Equation 2-16)}$$

$$k_0 = \frac{2\pi f}{c} \cdots\cdots\cdots \text{(Equation 2-17) (Balanis, 2005)}$$

where λ_0 is the wavelength.

2.7.4.2 Cavity model

Since its introduction in 1979 (Lo, Solomon & Richards, 1979), the cavity model has been widely used as a model analysis method for the rectangular microstrip patch antenna. In the cavity model (Figure 2-24), a microstrip patch antenna is a lossy resonant cavity bounded by electric walls on both of the top and bottom interfaces, and magnetic walls along the perimeter of the microstrip patch antenna (Chen & Wang, 2015). The cavity model assumes that the fields underneath the patch are the summation of various resonant modes, and the fringing fields along the perimeter is taken into account by extending a small offset distance out of the patch periphery (Chen & Wang, 2015). Therefore, the cavity model is conceptually more advanced than the transmission-line model, and typically produces more accurate results.

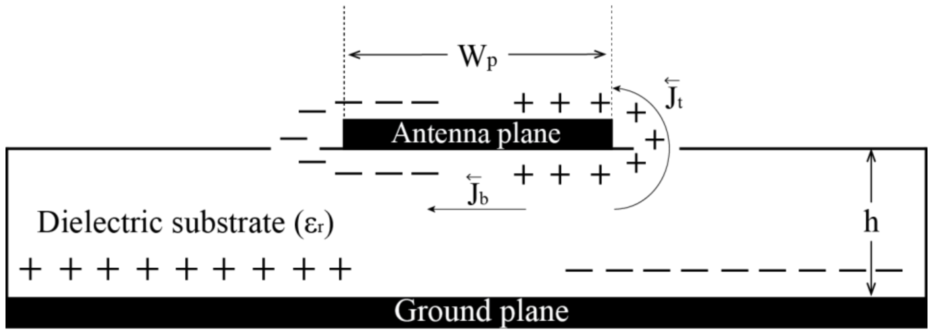

Figure 2-24. Cross section of a rectangular microstrip patch antenna in the cavity model. Redrawn from "Antenna Theory: Analysis and Design" (p.827) by C. A. Balanis, 2005, Hoboken, NJ: Wiley.

In the cavity model, cavity walls are considered to be lossless, as well as all the materials within the cavity walls. Normalized electric and magnetic field distributions are assumed beneath the patch (Figure 2-24). Under such circumstances, cavity would not radiate and its impedance would be purely reactive (Balanis, 2005). In order to account for the radiation, radiation resistance (R_r) and loss resistance (R_l) are introduced, and in order to make the lossy cavity to represent an antenna, effective loss tangent (δ_{eff}) is approximated to:

$$\delta_{eff} = \frac{1}{Q_T} = \frac{1}{Q_d} + \frac{1}{Q_c} + \frac{1}{Q_r} + \frac{1}{Q_{sw}} \cdots\cdots\cdots \text{(Equation 2-18)}$$

where Q_T is the total quality factor of the cavity, Q_d is the dielectric loss component, Q_c is the conductor loss component, Q_r is the radiation loss components, and Q_{sw} is the surface wave loss component (Bancroft, 2009). Quality factor for the dielectric loss, conductor loss, and radiation loss are given by:

$$Q_d = \frac{1}{tan\delta} \cdots\cdots\cdots \text{(Equation 2-19)}$$

$$Q_c = \frac{h}{\delta} \cdots\cdots\cdots \text{(Equation 2-20)}$$

$$Q_r = \frac{2\omega W_{es}}{P_r} \cdots\cdots\cdots \text{(Equation 2-21)}$$

$$Q_{sw} \propto Q_r \cdots\cdots\cdots \text{(Equation 2-22)}$$

where ω is the radian frequency, h is the height of the substrate, P_r is the power radiated from the cavity and W_{es} is the stored energy in the cavity (Bancroft, 2009). The surface wave loss component (Q_{sw}) is related to the radiation quality factor (Q_r) and can be negligible for very thin ($h \ll \lambda_0$) substrates (Carver & Mink, 1981; Pozar, 1990).

For antenna design implementation, the conductance of the two radiating slots can be derived by the cavity model:

$$G_1 = \frac{I}{120\pi^2} \cdots\cdots\cdots \text{(Equation 2-23) (Balanis, 2005)}$$

$$G_{12} = \frac{1}{120\pi^2}\int_0^{\pi} \left(\frac{sin\left(\frac{\frac{2\pi f}{c} W_p}{2}\right)}{cos\,\theta} \right)^2 J_0(k_0 L_p\, sin\,\theta\,) sin^3\,\theta d\theta$$

$$\cdots\cdots\cdots \text{(Equation 2-24) (Balanis, 2005)}$$

where

$$I = -2 + \cos x + xS_i(x) + \frac{\sin x}{x} \cdots\cdots\cdots \text{(Equation 2-25)}$$

$$x = \frac{2\pi f}{c} W_p \ \cdots\cdots\cdots \text{(Equation 2-26)}$$

G_1 and G_{12} are the conductance of two slots, and the plus $(+)$ sign is used for antisymmetric resonant voltage distribution mode beneath the patch and between the slots, whereas the minus $(-)$ sign is used for symmetric resonant distribution mode. J_0 is the Bessel function of first kind of order zero. Hence, a more accurate resonant input impedance than the transmission-line model can be obtained by:

$$Z_{in} = R_{in} \cos^2\left(\frac{\pi}{L_p} F_i\right) \cdots\cdots\cdots \text{(Equation 2-27) (Derneryd, 1978)}$$

where F_i is the inset feed, and the conductance gives the resonant input resistance:

$$R_{in} = \frac{1}{2(G_1 \pm G_{12})} \cdots\cdots\cdots \text{(Equation 2-28) (Balanis, 2005)}$$

2.7.4.3 Other empirical equations

The transmission-line and cavity models assume the infinite ground plane, and this is not realistic for antenna design implementation. The minimum size of the width (W_g) and length (L_g) of the ground plane are empirically calculated by:

$$W_g \geq W_p + 6h \cdots\cdots\cdots\cdot \text{(Equation 2-29)}$$

$$L_g \geq L_p + 6h \cdots\cdots\cdots\cdot \text{(Equation 2-30) (Kumar \& Ray, 2003)}$$

Next, the gap of the feed line (g) (Figure 18) can be approximated based on the effective dielectric constant and resonant frequency, and is given by:

$$g = \frac{c}{\sqrt{2\varepsilon_{reff}}} \frac{4.65\times10^{-12}}{f_o} \cdots\cdots\cdots\cdot \text{(Equation 2-31) (Matin \& Sayeed, 2010)}$$

The width of the feed line (W_f) can be approximated by:

$$W_f = \frac{2h}{\pi}\left[B - 1 - ln(2B-1) + \frac{\varepsilon_r - 1}{2\varepsilon_r}\left\{ln(B-1) + 0.39 - \frac{0.61}{\varepsilon_r}\right\}\right]$$

$$\cdots\cdots\cdots\cdot \text{(Equation 2-32) (Balanis, 1997)}$$

where

$$B = \frac{377\pi}{2Z_0\sqrt{\varepsilon_r}} \cdots\cdots\cdots\cdot \text{(Equation 2-33) (Balanis, 1997)}$$

and $Z_0 = \sqrt{\frac{\varepsilon_0}{\mu_0}}$ in the transverse electromagnetic (TEM) mode.

2.7.4.4 Substrate selection

For microstrip patch antennas, the thickness, dielectric constant and loss tangent of a substrate are selected based on the required radiated power and impedance bandwidth. A thicker substrate, for example, will increase the radiated power and improve impedance bandwidth (Garge, Bhartia, Bahl & Ittipboon, 2001). However, increasing the substrate thickness will also result in large dielectric and surface wave losses, and the rectangular microstrip patch antenna will stop resonating for substrate thickness greater than $0.11\lambda_0$ due to inductive reactance of the probe feed (Garge et al., 2001). For the dielectric constant, a smaller value will increase the radiated power by allowing the larger fringing field at the patch periphery (Kumar & Ray, 2003). However, it can also increase the size of the patch (Bahl & Bhartia, 1980; Balanis, 1989; Hammerstad, 1975). The loss tangent is the parameter that quantifies the loss of the substrate, and a substrate with a larger loss tangent creates a higher dielectric loss (Thierauf, 2011). Therefore, the thickness and dielectric constant of a substrate are chosen by the required physical and electrical properties, and a lower loss tangent is preferred for a better antenna performance.

2.7.4.5 Antenna evaluation

In order to evaluate the performance of an antenna in a two-port network problem (Figure 2-25), scattering parameters, or "s-parameters", are conveniently used. S-parameters:

$$[S] = \begin{bmatrix} S_{11} & S_{12} \\ S_{21} & S_{22} \end{bmatrix}$$

can be related to the reflection and transmission coefficients, and hence, they quantify the ratio of the reflected and transmitted energy. For a lossless environment, the energy transmitted into the device (S_{12} or S_{21}) describes the gain, and the energy reflected back from the device to the input port (S_{11} or S_{22}) describes the mismatch loss (Huang & Boyle, 2008). Therefore, by measuring the s-parameters, the antenna performance can be conveniently evaluated.

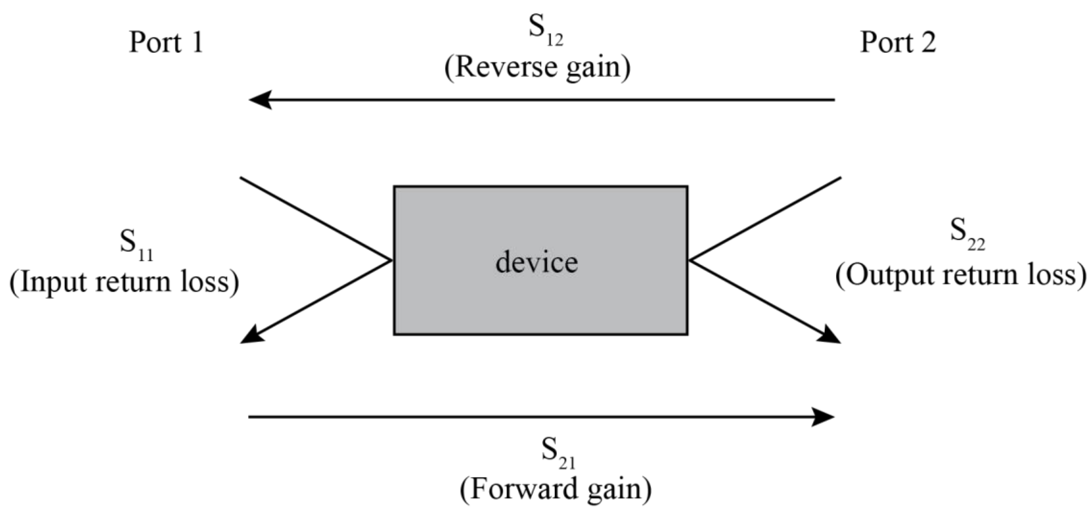

Figure 2-25. S-parameters.
Redrawn from “Antennas: From Theory to Practice” (p.256) by Y. Huang & K. Boyle, 2008, Chichester, UK: Wiley.

Chapter 3 EXPERIMENT (I):

Investigations of Electrical Properties of Inkjet-Printed Silver Ink on PET Film

In order to fabricate a microstrip patch antenna by conductive inkjet printing, it was required to obtain a conductor with reasonably low electrical resistance and resistivity. Hence, Experiment (I) was undertaken to obtain the lowest electrical resistance and resistivity of the inkjet-printed silver ink by different post-treatments. A flowchart of the experimental process is shown in Figure 3-1.

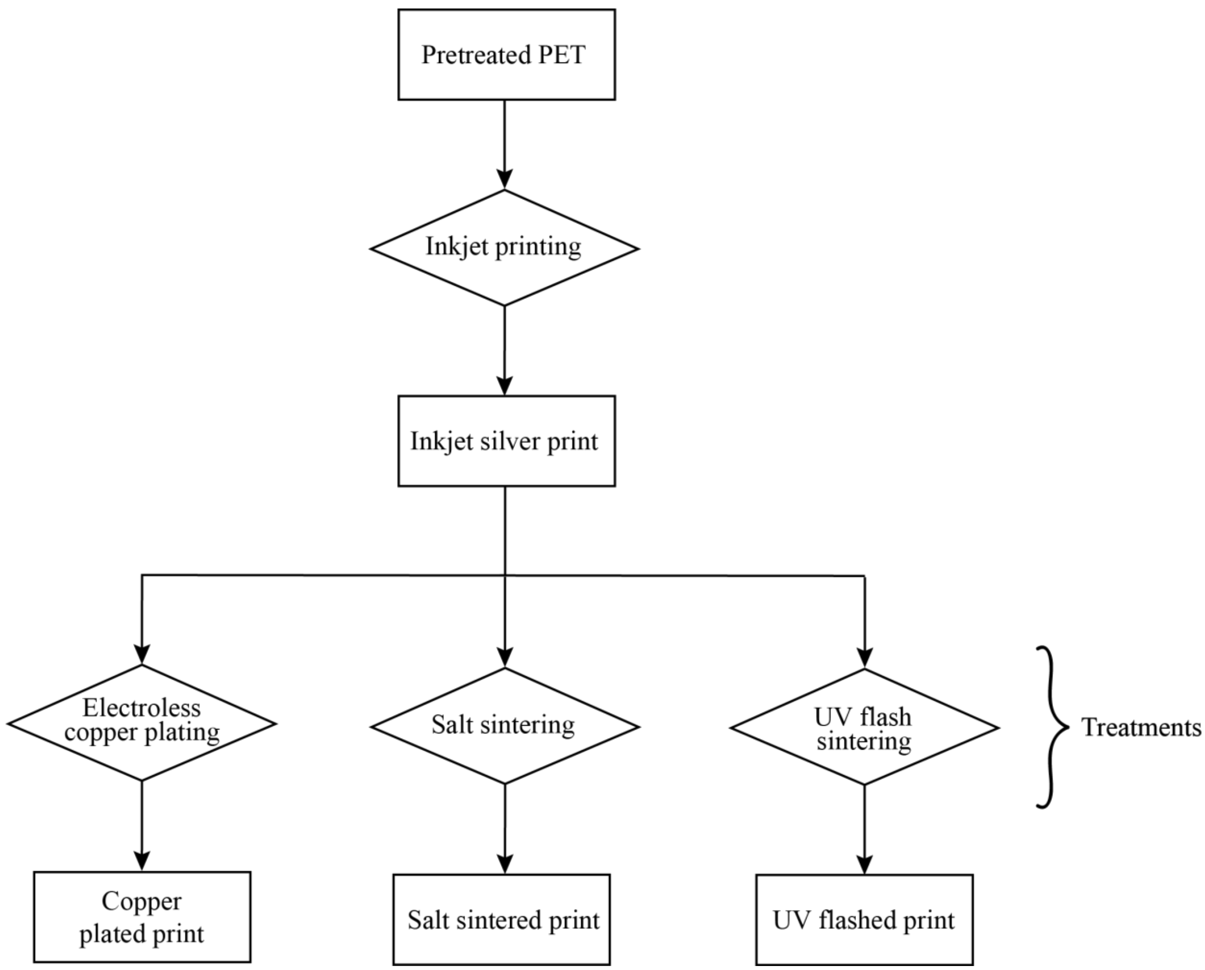

Figure 3-1. Flowchart of Experiment (I).

3.1 Research Questions and Hypotheses

The following research questions and statistical hypotheses were generated for Experiment (I).

3.1.1 Research question 1 (RQ1):

Can the electroless copper plating, salt sintering and UV-flash sintering decrease electrical resistance of the inkjet silver print?

• Null hypothesis for RQ1 ($\mathrm{H}_{0,1}$): The mean electrical resistance of the inkjet silver print ($\bar{R}_{\mathrm{Ag}}$), copper-plated print ($\bar{R}_{\mathrm{Copper}}$), salt-sintered print ($\bar{R}_{\mathrm{Salt}}$) and UV-flashed print ($\bar{R}_{\mathrm{UV}}$) are all equal. I.e.,

$$\mathrm{H}_{0,1}: \bar{R}_{\mathrm{Ag}} = \bar{R}_{\mathrm{Copper}} = \bar{R}_{\mathrm{Salt}} = \bar{R}_{\mathrm{UV}}$$

• Alterative hypothesis for RQ1 ($\mathrm{H}_{a,1}$): Not all the means of the electrical resistance are equal.

3.1.2 Research question 2 (RQ2):

Can the electroless copper plating, salt sintering and UV-flash sintering decrease electrical resistivity of the inkjet silver print?

• Null hypothesis for RQ2 ($\mathrm{H}_{0,2}$): The mean electrical resistivity of the inkjet silver print ($\bar{\rho}_{\mathrm{Ag}}$), copper-plated print ($\bar{\rho}_{\mathrm{Copper}}$), salt-sintered print ($\bar{\rho}_{\mathrm{Salt}}$) and UV-flashed print ($\bar{\rho}_{\mathrm{UV}}$) are all equal. I.e.,

$$\mathrm{H}_{0,2}: \bar{\rho}_{\mathrm{Ag}} = \bar{\rho}_{\mathrm{Copper}} = \bar{\rho}_{\mathrm{Salt}} = \bar{\rho}_{\mathrm{UV}}$$

• Alternative hypothesis for RQ2 ($\mathrm{H}_{a,2}$): Not all the means of the electrical resistivity are equal.

3.2 Experimental

3.2.2 Conductive inkjet printing

Firstly, the design of the inkjet silver print was drawn on Adobe® Illustrator® CC 2015.2.1 released by Adobe Systems Inc. (Sun Jose, CA). The dimensions of the inkjet silver print were 0.1 mm × 10 mm lines and 20 mm × 20 mm squares (Figure 3-2). For the linear prints, the lines were placed parallel to the direction of the printer nozzle movement. The full-scale design is available in Appendix A.

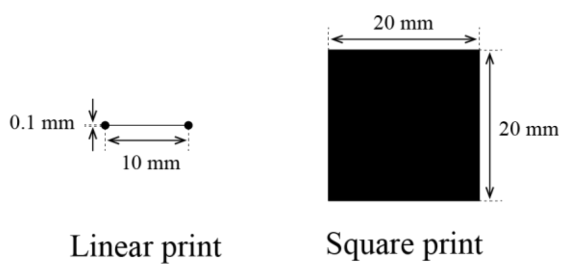

Figure 3-2. Print designs.

A piezoelectric inkjet printer (Epson® Stylus® C88+) (Table 3-1) supplied by Epson America Inc. (Long Beach, CA) was used for the conductive inkjet printing. A clean cartridge was filled with a conductive ink containing 25wt% silver nanoparticles and 1-15wt% ethylene glycol (Metalon® JS-B25P, NovaCentrix® Corporation, Austin, TX) (Figure 3-3) as shown in Figure 3-4, and installed into the printer. Then, a one-side pretreated PET film (Novele™ IJ-220) supplied by NovaCentrix® Corporation (Austin, TX) (Figure 3-3) was fed into the printer, and printed with the "best photo" and "matte paper" settings in the quality control panel. The printed films were dried at room temperature for 24 hours to evaporate the ink solvent.

Table 3-1. Printer specifications.

Resolution (dpi)	Numbers of nozzle	Ink droplet size (pL)
5760 × 1440	180	> 3

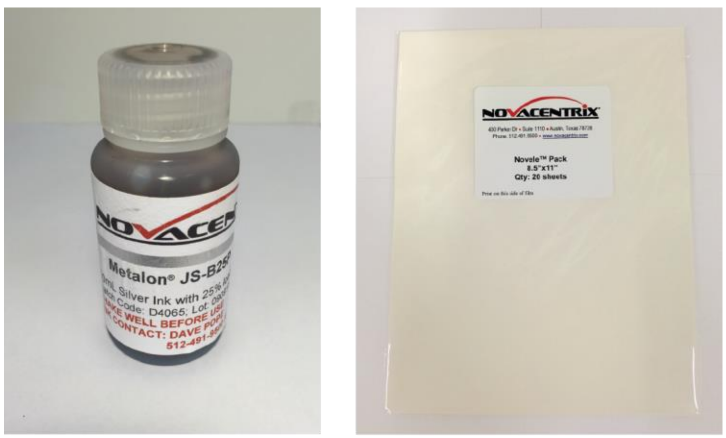

Silver ink — Pretreated PET film

Figure 3-3. Silver ink and pretreated PET film.

Table 3-2. Ink properties.

Silver content (wt%)	Viscosity (cP)	Surface tension (dyne/cm)	Particle size (nm)
25	5	31	75

Figure 3-4. Cartridge filled with the silver ink.

3.2.3 Electroless copper plating

In order to decrease the electrical resistance, electroless copper plating was performed on the inkjet silver print. The plating bath was prepared following Kao and Chou (2007). The electroless copper plating bath contained 24 g of 99% ethylenediaminetetraacetic acid (Sigma Aldrich Co. LLC (St. Louis, MO)), 0.029 g of 98.5% potassium ferrocyanide (Sigma Aldrich Co. LLC (St. Louis, MO)), 9 g of 98% copper (II) sulfate pentahydrate (Sigma Aldrich Co. LLC (St. Louis, MO)), and 11.3 mL of 37% formaldehyde solution (Sigma Aldrich Co. LLC (St. Louis, MO)) in 500 mL of deionized water, where the pH was adjusted to 12.8 by dissolving 97% sodium hydroxide anhydrous (Sigma Aldrich Co. LLC (St. Louis, MO)) (Kao & Chou, 2007).

Next, the inkjet silver print was immersed into the plating bath for 30 min at the room temperature (Figure 3-5). This allowed the formation of uniform copper layer over the inkjet silver print, as shown in Figure 3-6. Finally, the copper-plated print was gently rinsed with deionized water, and dried at the room temperature for 24 hours.

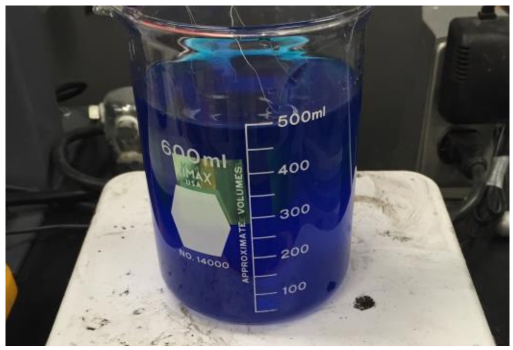

Figure 3-5. Electroless copper plating of the inkjet silver print.

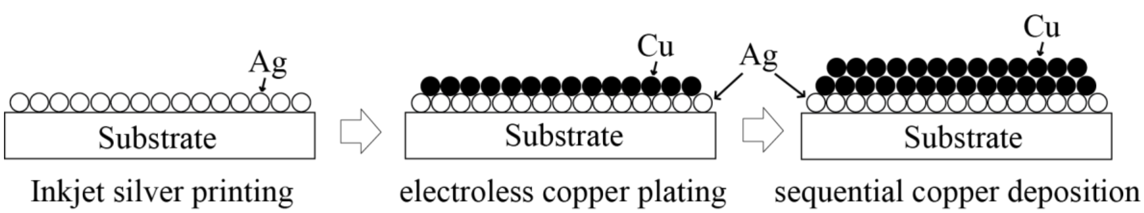

Figure 3-6. Cross-sectional diagram of the electroless copper plating.

3.2.4 Salt sintering

A salt sintering solution was prepared following Layani et al (2012). 1.75 g of sodium chloride anhydrous (99%) (Sigma Aldrich Co. LLC (St. Louis, MO)) was dissolved in 100 mL of deionized water, and 0.3 mol/L sodium chloride solution was obtained. Then, a clean cartridge was filled with the salt sintering solution, and installed into the nozzle. Then, the salt sintering solution was inkjet-printed on the top of the inkjet silver print. Finally, the obtained print was dried at the room temperature for 24 hours.

3.2.5 UV-flash sintering

The UV-flash sintering was performed by a sintering device (Sinteron 500^{TM} Photonic Curing R&D System) (Figure 3-7) supplied by Xenon Corporation (Wilmington, MA). The 3.8 kV UV-flash sintering lamp was installed with a lower cutoff wavelength of 370 nm. The distance from the lamp to the printed surface was set to the minimum distance of 25.48 mm. The size of the mechanical aperture was set to 8 mm on the lamp housing. All the surface of the inkjet silver print was treated by single UV pulse for 520 μs.

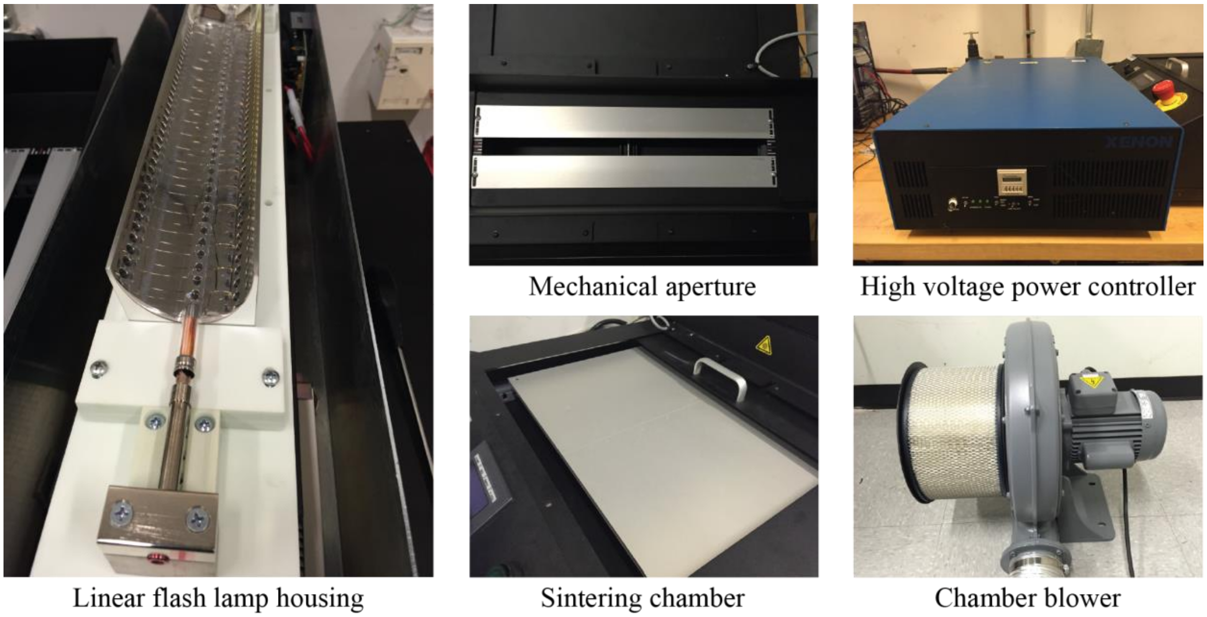

Figure 3-7. UV-flash sintering device.

3.2.6 Electrical resistance measurement and statistical analysis

For each treatment group, the electrical resistance of 20 samples of 0.1 mm × 10 mm line print was measured by a multimeter (Fluke® 179 True RMS Digital Multimeter) supplied by Fluke Inc. (Everett, WA). Then, the obtained data were analyzed with RStudio® 0.99.473, an open-source statistical software released by RStudio Inc. (Boston, MA).

One-factor ANOVA was performed to assess the overall difference of fixed effects by the different treatments. A fixed effects model of one-way ANOVA was used for the statistical testing. That was:

$$y_{ij} = \mu + \alpha_i + \varepsilon_{ij} \cdots\cdots\cdots \text{(Equation 3-1)}$$

where y is the response (electrical resistance), i is the index of the treatments, j is the index of the sample (individual print) within each treatment, μ is the reference level, α_i is the treatment effect, and ε_{ij} is the error term.

Next, the Tukey's honestly significant difference (HSD) test was performed to analyze the differences among the conductive prints. Confidence level of 99% was chosen.

3.2.7 Measurements of the physical dimensions

To obtain the dimensions of the conductive prints, a stereo microscope (Bausch & Lomb MonoZoom-7 Microscope) supplied by Bausch & Lomb Inc. (Rochester, NY) was operated to measure the width of the conductive prints. Then, an SEM (Phenom G1) supplied by Phenom World (Netherlands) was operated to measure the thickness of the conductive prints. The samples for the SEM were prepared by cutting the 20 × 20 mm square prints with scissors.

3.2.8 Electrical resistivity calculations and statistical analysis

The electrical resistivity (ρ) of a cuboidal conductor is defined by:

$$\rho = R\frac{A}{L} \cdots\cdots\cdots \text{(Equation 3-2)}$$

where R is the electrical resistance of the conductor in ohms, A is the cross sectional area of conductor in square meters, and L is the length of the conductor in meter (Figure 3-8).

Therefore, the electrical resistivity was calculated by the measured dimensions of the conductive prints.

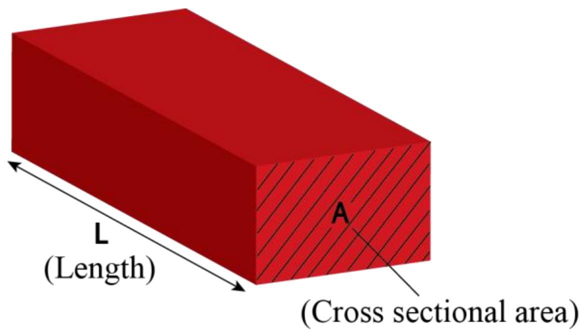

Figure 3-8. Schematic diagram of a cuboidal conductor.

One-factor ANOVA was performed to assess the overall difference of fixed effects by the different treatments. A fixed effects model of one-way ANOVA was used for the statistical testing. That was:

$$y_{ij} = \mu + \alpha_i + \varepsilon_{ij} \cdots\cdots\cdots \text{(Equation 3-3)}$$

where y is the response (electrical resistivity), i is the index of the treatments, j is the index of the sample (individual print) within each treatment, μ is the reference level, α_i is the treatment effect, and ε_{ij} is the error term.

Finally, the Tukey's HSD test was performed to analyze the differences among the conductive prints. Confidence level of 99% was chosen.

3.3 Results

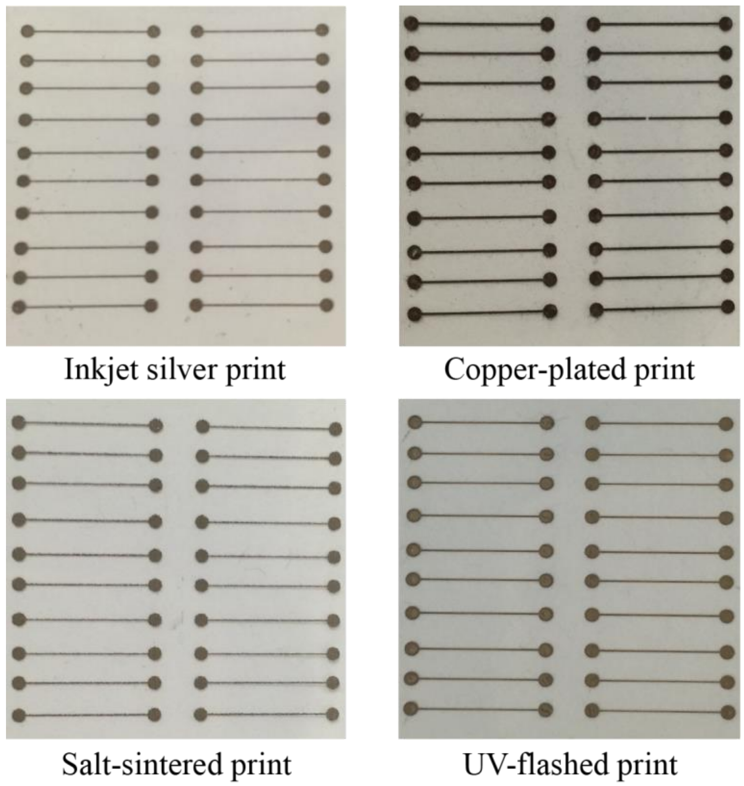

Figure 3-9. Top-view photographs of the linear prints.

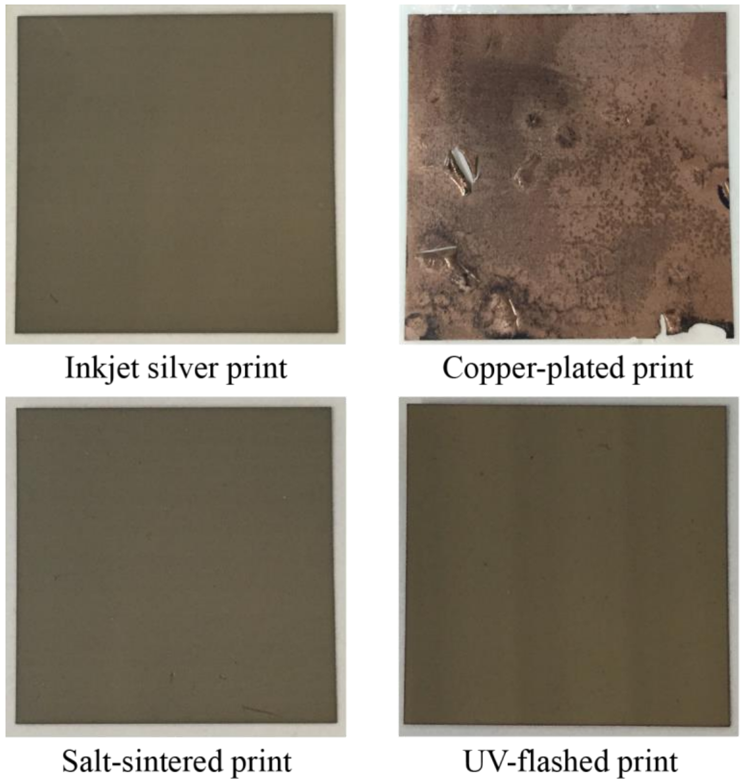

Figure 3-10. Top-view photographs of the square prints.

Figure 3-9 and Figure 3-10 display the photographs of the conductive prints before and after different treatments. Silver ink was successfully inkjet printed on the PET film. The sharpness of the edges was clear for the inkjet silver print, the salt-sintered silver print, and the UV-flashed print. However, numerous cracks were observed in the copper-plated print.

3.3.1 Electrical resistance

The results of the electrical resistance measurement are shown in Appendix B. The descriptive statistics are shown in Table 3-3.

Table 3-3. Descriptive statistics of the electrical resistance data.

Conductor type	n	Mean (Ω)	Variance	Standard deviation
Inkjet silver print	20	46.8	1.82	1.35
Copper-plated print	20	4.5	1.61	1.27
Salt-sintered print	20	37.9	5.00	2.24
UV-flashed print	20	7.5	0.03	0.18

Next, the electrical resistance data was analyzed by one factor ANOVA with the statistical hypothesis, which was:

$H_{0,1}$: $\bar{R}_{\text{Ag}} = \bar{R}_{\text{Copper}} = \bar{R}_{\text{Salt}} = \bar{R}_{\text{UV}}$

$\text{H}_{\text{a},2}$: Not all the means of the electrical resistance are equal.

The ANOVA table is given in Table 3-4. The one-factor ANOVA F-test suggests that there was significant differences among the print types at $p < 0.0001$.

Table 3-4. One-factor ANOVA of the electrical resistance data.

Source	df	SS	MS	F	Pr (> F)
Conductor type	3	27284	9095	4290	< 0.0001
Error	76	161	2		
Total	79	27445			

To examine the difference among the conductor types, the Tukey's HSD test was performed for post hoc analysis. Table 3-5 shows the Tukey's HSD test. The Tukey's HSD test suggests that all of the six combinations were significantly different in terms of electrical resistance ($p < 0.0001$). In addition, it was also found that all of the three treatments decreased the electrical resistance of the inkjet silver print, and the lowest electrical resistance was 4.5 Ω obtained by the electroless copper plating. The second best electrical resistance was 7.8 Ω obtained by the UV-flash sintering.

Table 3-5. Tukey's HSD test of the electrical resistance data.

Comparison	Difference	Lower	Upper	P-value
Copper-plated print – inkjet silver print	-42.29	-44.772	-40.808	< 0.0001
Salt -sintered print – inkjet silver print	-8.875	-10.357	-7.393	< 0.0001
UV-flashed print – inkjet silver print	-39.255	40.737	-37.773	< 0.0001
Salt-sintered print – copper-plated print	33.415	31.933	34.897	< 0.0001
UV-flashed print – copper-plated print	3.035	1.552	4.517	< 0.0001
UV-flashed print – salt-sintered print	-30.38	-31.862	-28.898	< 0.0001

3.3.2 Dimensions

First of all, Table 3-6 shows the dimensions of the fabricated conductive lines. The width was measured by the stereo microscope, and the thickness was measured by the SEM. Because the length is determined by the placement of the multimeter probes, the designed value of 1.0×10^{-4} mm is shown in the table. The top-view images of the stereo microscope are shown in Figure 3-11, and the cross-sectional images of the SEM are shown in Figure 3-12.

Table 3-6. Dimensions of the conductive prints.

Conductor type	Length (m)	Width (m)	Thickness (m)
Inkjet silver print	1.0×10^{-2}	1.0×10^{-4}	1.3×10^{-6}
Copper-plated print	1.0×10^{-2}	1.0×10^{-4}	4.5×10^{-6}
Salt-sintered print	1.0×10^{-2}	1.0×10^{-4}	1.3×10^{-6}
UV-flashed print	1.0×10^{-2}	1.0×10^{-4}	1.0×10^{-6}

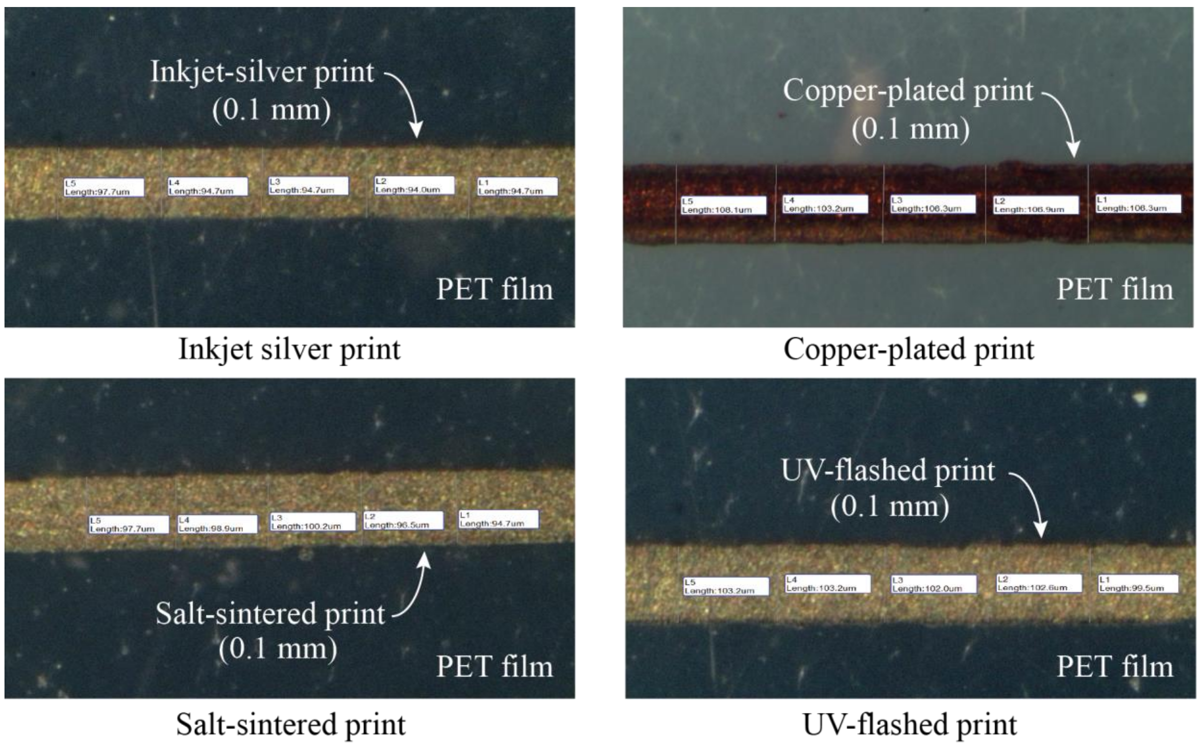

Figure 3-11. Stereo microscopic images of the linear prints from top-view.

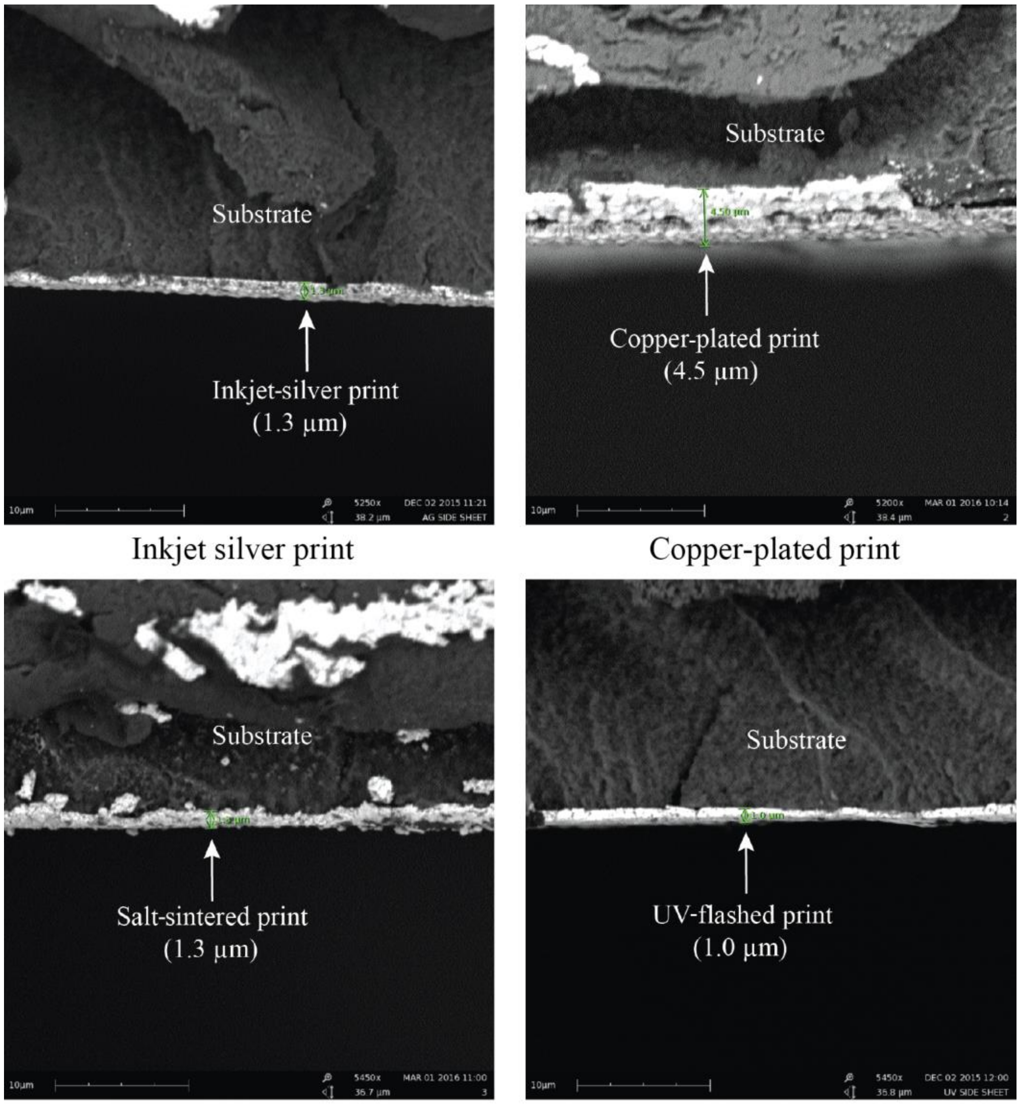

Inkjet silver print | Copper-plated print | Salt-sintered print | UV-flashed print

Figure 3-12. SEM images of the square prints from cross-sectional view.

The stereo microscope images indicates that the widths of the conductive lines were nearly the same as the designed value of 0.1 mm. The length of the conductive prints are determined by the placement of the multimeter, and thus, it was not measured.

From the cross sectional observations of the conductive prints, it was found that the copper-plated print had a significant thickness increase. This suggests that the relatively thick (< 3 μm) copper layer was formed over the silver layer. On the other hand, a slight thickness reduction was observed in the UV-flashed print. This suggests that the inkjet silver print was successfully coalesced by the UV pulse. However, there was no significant difference in thickness by the salt-sintering.

3.3.3 Electrical resistivity

The results of the electrical resistivity calculation are shown in Appendix C. The descriptive statistics are shown in Table 3-7.

Table 3-7. Descriptive statistics of the electrical resistivity data.

Conductor type	n	Mean (Ω·m)	Variance	Standard deviation
Inkjet silver print	20	6.1×10^{-7}	2.83×10^{-16}	1.69×10^{-8}
Copper-plated print	20	2.0×10^{-7}	3.26×10^{-15}	5.71×10^{-8}
Salt-sintered print	20	5.3×10^{-7}	1.00×10^{-15}	3.17×10^{-8}
UV-flashed print	20	7.5×10^{-8}	3.37×10^{-18}	1.83×10^{-9}

The electrical resistivity data was analyzed by one factor ANOVA with the statistical hypothesis, which was:

$H_{0,2}$: $\bar{\rho}_{\mathrm{Ag}} = \bar{\rho}_{\mathrm{Copper}} = \bar{\rho}_{\mathrm{Salt}} = \bar{\rho}_{\mathrm{UV}}$

$\mathrm{H}_{\mathrm{a},2}$: Not all the means of the electrical resistivity are equal.

The ANOVA table is given in Table 3-8. The one-factor ANOVA F-test suggests that there was significant difference among the print types at $p < 0.0001$.

Table 3-8. One-factor ANOVA of the electrical resistivity data.

Source	df	SS	MS	F	Pr (> F)
Conductor type	3	3.95×10^{-12}	1.32×10^{-12}	1155.7	< 0.0001
Error	76	8.66×10^{-14}	1.14×10^{-15}		
Total	79	4.03×10^{-12}			

To examine the difference among the conductor types, the Tukey's HSD test was performed for the post-hoc analysis. Table 3-9 shows the Tukey's HSD test of the electrical resistivity data. The Tukey's HSD test suggests that all of the six combinations were significantly different in terms of the electrical resistivity ($p < 0.0001$). In addition, it was also found that all of the three treatments decreased the electrical resistivity of the inkjet silver print, and the lowest electrical resistivity was 7.5×10^{-8} Ω·m obtained by the UV-flash sintering.

Table 3-9. Tukey's HSD test of the electrical resistivity data.

Comparison	Difference	Lower	Upper	P-value
Copper-plated print – inkjet silver print	-4.07×10^{-7}	-4.42×10^{-7}	-3.73×10^{-7}	< 0.0001
Salt-sintered print – inkjet silver print	-7.70×10^{-8}	-1.11×10^{-8}	-4.26×10^{-8}	< 0.0001
UV-flashed print – inkjet silver print	-5.34×10^{-7}	-5.68×10^{-7}	-4.99×10^{-7}	< 0.0001
Salt-sintered print – copper-plated print	3.30×10^{-7}	2.96×10^{-7}	3.65×10^{-7}	< 0.0001
UV-flashed print – copper-plated print	-1.36×10^{-7}	-1.61×10^{-7}	-9.18×10^{-7}	< 0.0001
UV-flashed print – salt-sintered print	-4.57×10^{-7}	-4.91×10^{-7}	-4.22×10^{-7}	< 0.0001

3.4 Conclusions and Recommendations

In Experiment (I), the deposition of silver nanoparticles onto the pretreated PET substrate was successfully done by the conductive inkjet printing, and 10 mm × 0.1 mm line and 20 × 20 mm square prints were obtained. Then, the inkjet silver print was treated by the electroless copper plating, salt sintering and UV-flash sintering, respectively, in order to decrease the electrical resistance and resistivity. Although the salt-sintered print and UV-flashed print retained good print quality after the treatment, the copper-plated print had numerous cracks. This was because the pretreated layer of the PET film dissolved in the solution during the electroless copper plating process.

For all the treatments, statistically significant decrease in electrical resistance was observed at $p < 0.0001$, and the electroless copper plating was found to be the most effective method by the post-hoc test. As a next step, the physical dimensions of the conductive prints were measured by the stereo microscope and SEM. The width of the conductive prints were 0.1 mm regardless of the treatment. On the other hand, the thickness of the inkjet silver print, copper-plated print, salt-sintered print, and the UV-flashed print were 1.3 μm, 4.5 μm, 1.3 μm and 1.0 μm, respectively.

Finally, the electrical resistivity was calculated by the physical dimensions of the conductive prints. For all the treatments, statistically significant decrease in electrical resistivity was obtained at $p < 0.0001$, and the UV-flash sintering was found to be the most effective method. The electrical resistivity obtained by the UV-flash sintering was 7.5×10^{-8} $\Omega{\cdot}$m, and this reaches 22% bulk conductivity of pure silver.

There are several possible factors that attributed to the higher electrical resistivity of the salt-sintered and UV-flash sintered prints compared to the bulk silver. The major reason might be the effects of the sintering. For the salt sintering method, the driving force of the sintering is the surface charges on silver nanoparticles caused by the electrolytes. Hence, it is critical to have a good contact between the salt solution and the silver nanoparticles in order to maximize the sintering effects. Therefore, typically, the printed silver ink is placed in a electrolyte solution for approximately 10 mins (Magdassi et al., 2010). However, in this research, the salt sintering solution was inkjet-printed on the surface of the inkjet silver print to avoid the water solubility issue of the substrate, and this limited the effects of the salt sintering.

For the UV-flash sintering method, the amount of the energy exposed to the substrate in this research was limited by the limited adhesion of the inkjet silver print. When the inkjet silver print was exposed to the maximum energy, the printed ink was blown out. Therefore, the adhesion of the silver ink limited the amount of the energy.

Probably, the most interesting method of decreasing electrical resistance is the electroless plating. Although the electroless copper plating was not successful because of the water solubility issue of the pretreated PET film, the copper-plated print still showed the lowest electrical resistance among all methods. This suggests that electroless plating is potentially advantageous as a method of increasing the thickness and decreasing the electrical resistance of the inkjet silver print.

Chapter 4 EXPERIMENT (II): Design, Fabrication, Measurement and Analysis of a 2.45 GHz Inkjet-Printed Microstrip Patch Antenna

Based on the electrical resistivity investigations of the printed conductors in Experiment (I), a UV-flashed print was selected as the conductor for a rectangular microstrip patch antenna. In this chapter, the design, fabrication, measurement and analysis of a 2.45 GHz microstrip patch antenna were presented. The size of a 2.45 GHz microstrip patch antenna was calculated by MATLAB® based on the empirical equations. Next, 3D full-wave electromagnetic field simulation was followed to optimize the antenna design. Then, the microstrip patch antennas were fabricated by the conductive inkjet printing. Finally, the analysis on comparisons between the simulation and measurement was presented. An overall flowchart of the experiment is shown in Figure 4-1.

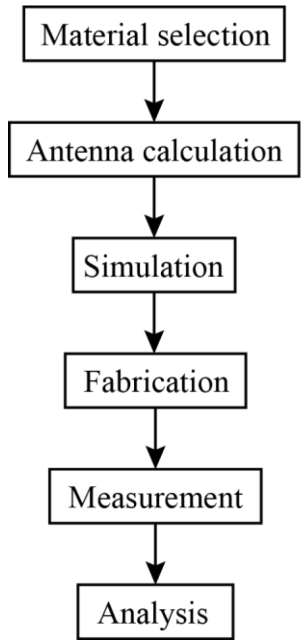

Figure 4-1. Flowchart of Experiment (II).

4.1 Research Question

The research question for Experiment (II) was if the simulated and measured S_{11} plots reasonably agree for an inkjet-printed rectangular microstrip patch antenna.

4.2 Experimental

4.2.1 Material selection

A typical microstrip patch antenna is composed of an antenna plane, ground plane, and dielectric substrate, and the electrical and dielectric properties of these three components determine the overall antenna performance. Hence, a conductor and substrate with low losses are necessary to withdraw the maximum antenna efficiency. Therefore, Experiment (I) was conducted to obtain a low loss conductor.

From Experiment (I), it was found that the copper-plated print has the lowest electrical resistance among all conductive prints. However, numerous cracks were formed in the copper-plated print because of the substrate's susceptibility to the water. On the other hand, the UV-flashed print showed the smallest electrical resistivity with the excellent print quality. Therefore, the UV-flashed print was selected as the conductor for the microstrip patch antenna.

As for the antenna substrate, the pretreated PET film was selected for its capability of adapting the silver nanoparticle ink. Also, the standard PET film has an excellent dielectric properties (Wypych, 2012), and ideal as an antenna material. Figure 4-2 shows the designed substrate for the microstrip patch antenna. Because the pretreated PET film has a one-sided coating layer, it was designed to superimpose two pretreated PET films with an adhesive substance, so that the both sides became printable. The PET-based double-sided tape (Scotch® Double Sided Tape, 3M Company, Maplewood, MN) was selected for its excellent adhesion to the PET film.

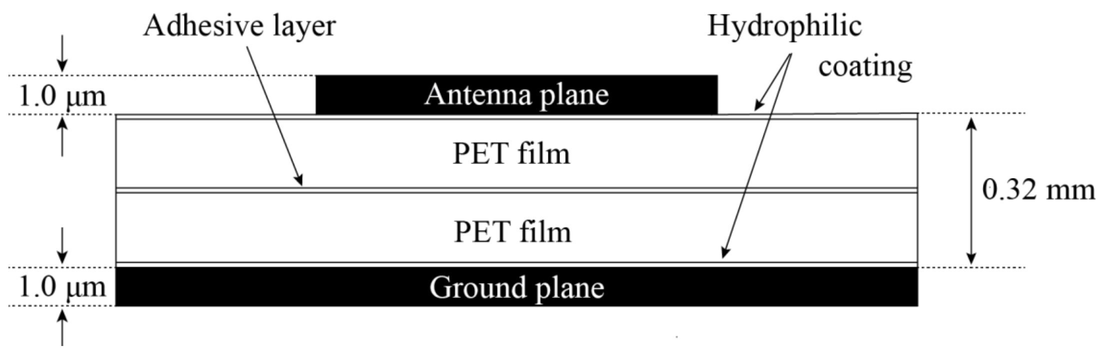

Figure 4-2. Schematic cross-section of the substrate.

Because the dielectric properties of the pretreated PET film was not specified exactly by the manfucturer, it was conveniently assumed that the superimposed substrate had similar dielectric properties to the standard PET film in this research. In other words, the constructed substrate was considered as a single PET layer with a dielectric constant of 2.6 and a loss tangent of 0.001 (Wypych, 2012). The thickness of 0.32 mm measured by the thickness tester (ProGage Thickness Tester, Thwing-Albert Instrument Co., West Berlin, NJ) as shown in Figure 4-3. This simplified model of the substrate was used throughout the antenna design processes and simulation processes in this research.

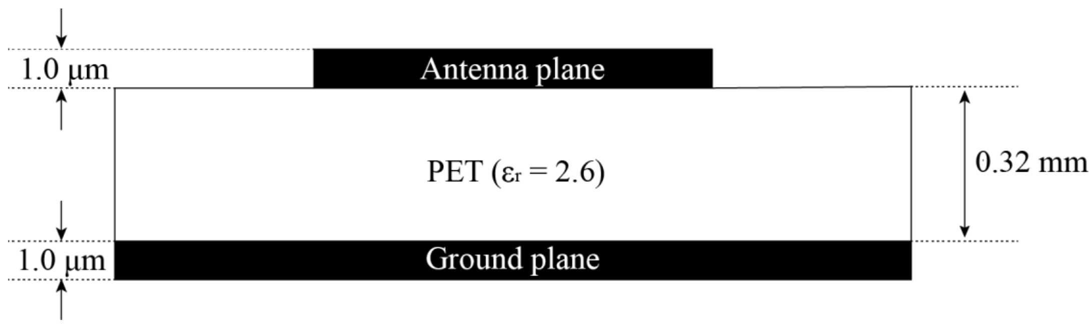

Figure 4-3. Schematic cross-section of the substrate in a simplified model.

4.2.2 Antenna design

Based on the simplified model of the substrate, the size of a 2.45 GHz microstrip patch antenna was calculated based on Equations 2-10 to 2-14 and 2-23 to 2-33. The parameters used for the antenna size calculation were summarized in Table 4-1 . The input impedance was set to 50 Ω. The resonant frequency of 2.45 GHz was selected because it is one of the most commonly used frequencies for the microwave hyperthermia. Then, MATLAB® R2015b (The MathWorks Inc., Natick, MA) was run to calculate the approximate antenna dimension. The MATLAB® code is available in Appendix D.

Table 4-1. Parameters used for the rectangular microstrip patch antenna size calculation.

Input Impedance (Ω)	Resonant frequency (GHz)	Dielectric constant	Substrate thickness (mm)
50	2.45	2.6	0.32

Next, 3D full-wave electromagnetic field simulation was conducted with CST Studio Suite® 2015 (CST-Computer Simulation Technology AG Inc., Darmstadt, Germany). Firstly, a finite antenna element model was created based on the calculated dimension and the measured thickness of the conductor and substrate. The electrical and dielectric properties of the conductor and substrate used for the simulation are shown in Table 4-2. For the conductor properties, the conductivity (1.4×10^7 S/m) and thickness (1.0 μm) of the UV-flashed print obtained in Experiment (I) were used. For the substrate properties, the standard values of dielectric constant (2.6) and loss tangent (0.001) of PET from the literature were used along with the measured thickness. Then, the antenna element was placed in the space, and a waveguide port with a 50 Ω impedance was created to connect to the edges of the microstrip feed line and ground plane. Finally, the frequency domain solver with tetrahedral meshing was run to obtain the S_{11} plot. Also, the optimized dimension of the antenna was obtained by parameter sweep of the antenna lengths.

Table 4-2. Substrate and conductor properties for simulation.

Substrate thickness (mm)	Dielectric constant	Loss tangent	Conductor thickness (μm)	Conductivity (S/m)
0.32	2.6	0.001	1.0	1.4×10^7

4.2.3 Fabrication

A clean ink cartridge was filled with the silver ink, and installed into the inkjet printer. Then, the antenna and ground planes were printed onto the pretreated PET film with the “best photo" and "matte paper" settings in the quality control panel. The printed antenna and ground planes were dried at room temperature for 24 hours to evaporate the ink solvent.

The UV-flash sintering device was operated at 3.8 kV with a lower cutoff wavelength of 370 nm lamp. The distance from the window of the lamp housing to the inkjet silver print was set to the minimum distance of 25.48 mm with the mechanical aperture of 8 mm. All the surface of the antenna and ground planes was treated by a single UV pulse for 520 μs. Then, the antenna and ground planes were superimposed to each other by the double-sided tape. To allow power supply, an SMA connector (Johnson® 142-0701-881, Cinch Connectivity Solutions, Waseca, MN) (Figure 4-4) was edge-mounted on the microstrip feed line using a silver conductive epoxy paste (8331 Silver Conductive Epoxy Adhesive, MG Chemicals®, British Columbia, Canada). Finally, the silver conductive epoxy paste was cured at the room temperature for 24 hours.

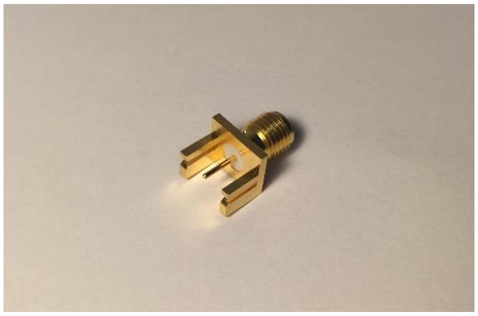

Figure 4-4. SMA connector.

4.2.4 Measurement

In antenna evaluation, S_{11}, or return loss, is an excellent index to understand the performance of an antenna. For microstrip patch antennas, the dimension is usually designed to have the maximum radiation from the antenna plane at a single resonant frequency, and there is little radiation at the non-resonant frequencies. The rest of the energy which are not radiated from the patch are either reflected back to the port, or consumed as conductor and dielectric losses. Therefore, by measuring the returned energy (S_{11}) from the antenna, the radiation from the patch can be conveniently understood.

In this research, therefore, the vector network analyzer (Agilent E5071C, Agilent Technologies Inc, Santa Clara, CA) (Figure 4-5) measured the S_{11} of the microstrip patch antennas at 1.5 to 3.5 GHz with a 50 Ω impedance load. Then, the return loss characteristics were analyzed based on the comparison between the simulation and measurement.

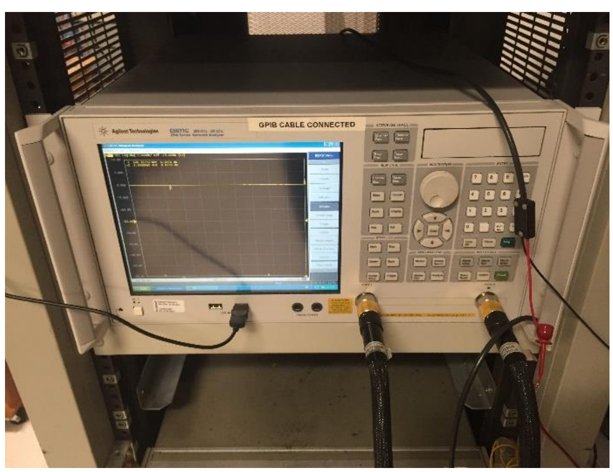

Figure 4-5. Vector network analyzer.

4.3 Results

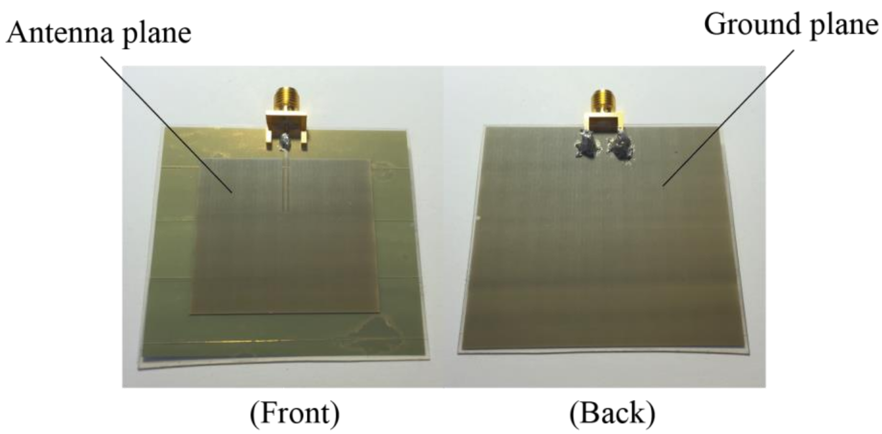

Figure 4-6. Microstrip patch antenna fabricated by the conductive inkjet printing.

Figure 4-6 displays the microstrip patch antenna fabricated by the conductive inkjet printing. The conductive inkjet printing with silver nanoparticles showed an excellent resolution in printing, and 0.25 mm of the gap of the feed line was achieved without a blur or other issues. The only noticeable issue was the snall amount of air trapped between the pretreated PET films.

4.3.1 Antenna geometry

Based on the antenna calculation and optimization, the reasonable antenna dimensions were successfully obtained, and are shown in Table 4-3 and Figure 4-7. From the comparison of the optimized and simulated antenna dimensions, there was a slight reduction in the patch size. This was because of the absence of some important parameters such as the conductor thickness and loss tangent of the substrate in the calculation, and this suggested the limited accuracy of the calculation.

Table 4-3. Calculated and optimized antenna dimensions (mm).

Method	W_P	L_P	W_f	g	F_i	W_g	L_g
Calculation	45.6	37.9	0.89	0.25	13.4	47.5	39.8
Simulation	40.0	36.0	0.89	0.25	14.4	60.0	53.0

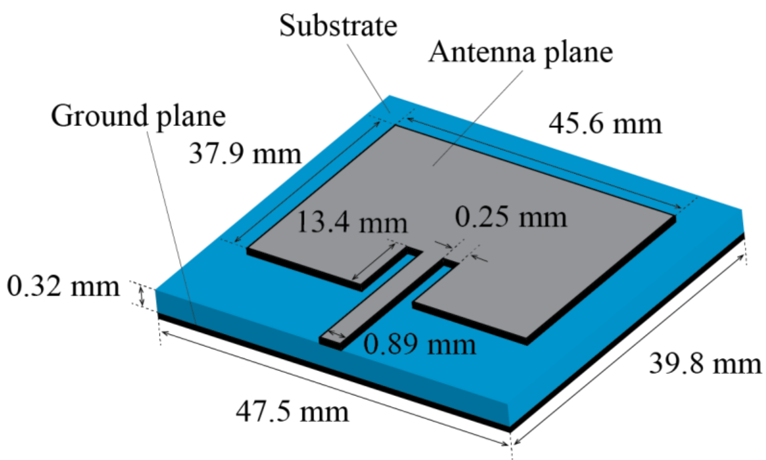

Calculated dimension

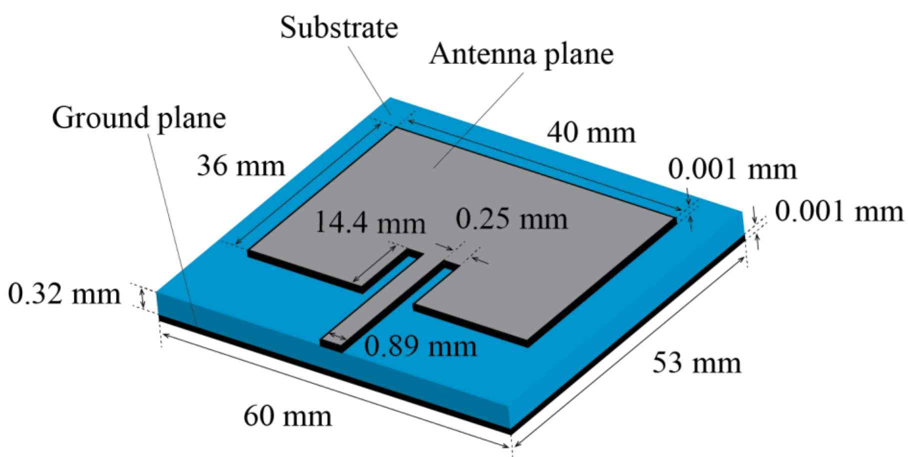

Simulated dimension

Figure 4-7. Calculated and simulated antenna dimensions.

4.3.2 Antenna evaluation

The S_{11} plots obtained by the simulation and measurement are shown in Figure 4-8, and a summary of the S_{11} are shown in Table 4-4. The measured S_{11} at the resonant frequency was -4.8 dB, and this was significantly higher than the simulated value of -10.3 dB. This indicated that a larger amount of the energy supplied to the antenna was returned to the port. On the other hand, the measured S_{11} at the non-resonant frequencies showed significantly lower values than the simulation, and this less reflection came from the larger losses in the antenna.

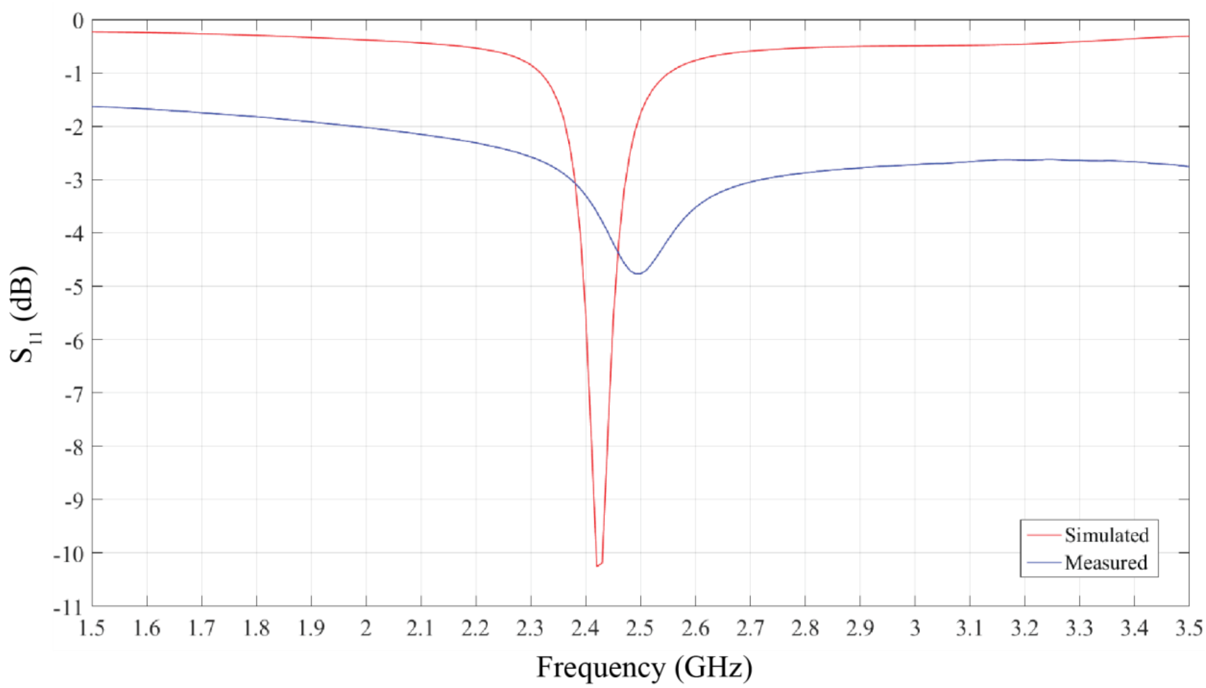

Figure 4-8. S_{11} plots obtained by the simulation and measurement.

Table 4-4. Simulated and measured S_{11} at the resonant frequencies.

Frequency (GHz)	Simulated S_{11} (dB)	Measured S_{11} (dB)
2.42 (Resonant frequency of simulation)	-10.3	-3.6
2.49 (Resonant frequency of measurement)	-2.1	-4.8

There could be a few reasons attributed to the difference between the simulation and measurement. The first factor would be the approximate values of the dielectric properties of the substrate. During the antenna modeling, the substrate was considered a single layer of PET film with the dielectric constant of 2.6 and loss tangent of 0.001. However, those values were the approximate estimations of standard PET films, which might not be exact for the PET film used in the experiment. Also, the fabricated antenna substrate was two PET films with pretreated layers and the adhesive substance.

Another factor could be additional resistive loss by the conductive silver epoxy paste. The conductive silver epoxy paste used in this research had electrical resistivity of 1.7×10^{-4} $\Omega\cdot$m, which was much higher than the electrical resistivity of the printed silver. Since the simulation did not consider the presence of the conductive silver epoxy paste, this might have attributed to the unexpected loss in the fabricated antenna.

In order to eliminate those factors and acquire the simulation closer to the actual measurement, two parameters were modified through the post-simulation. First, to account for the frequency shift, the antenna dimension used in the simulation was replaced by the actual dimension measured by the stereo microscope. The actual antenna dimension was slightly different from the intended dimension as shown in Table 4-5. Then, to account for the larger losses of the fabricated antenna, the loss tangent was increased to 0.08.

Table 4-5. Modeled and physical dimensions of the antenna (mm).

Dimension	W_P	L_P	W_f	g	F_i	W_g	L_g
Intended	40.0	36.0	0.89	0.25	14.4	60.0	53.0
Actual	39.8	35.2	0.90	0.25	14.0	59.8	52.8

The simulated S_{11} with the modified parameters is shown in Figure 4-9, and a summary of the S_{11} is shown in Table 4-6. From the comparison between the modified simulation and the measurement, it can be said that similar behavior of S_{11} at the both resonant and non-resonant frequencies were obtained. This implied that the substrate of the fabricated antenna be better represented with larger dielectric loss than the standard PET. In addition, the resonant frequency of the modified simulation was 2.47 GHz, and this was close to the measured value of 2.49 GHz. This suggested that the frequency shift was most likely due to the accuracy of the inkjet printing.

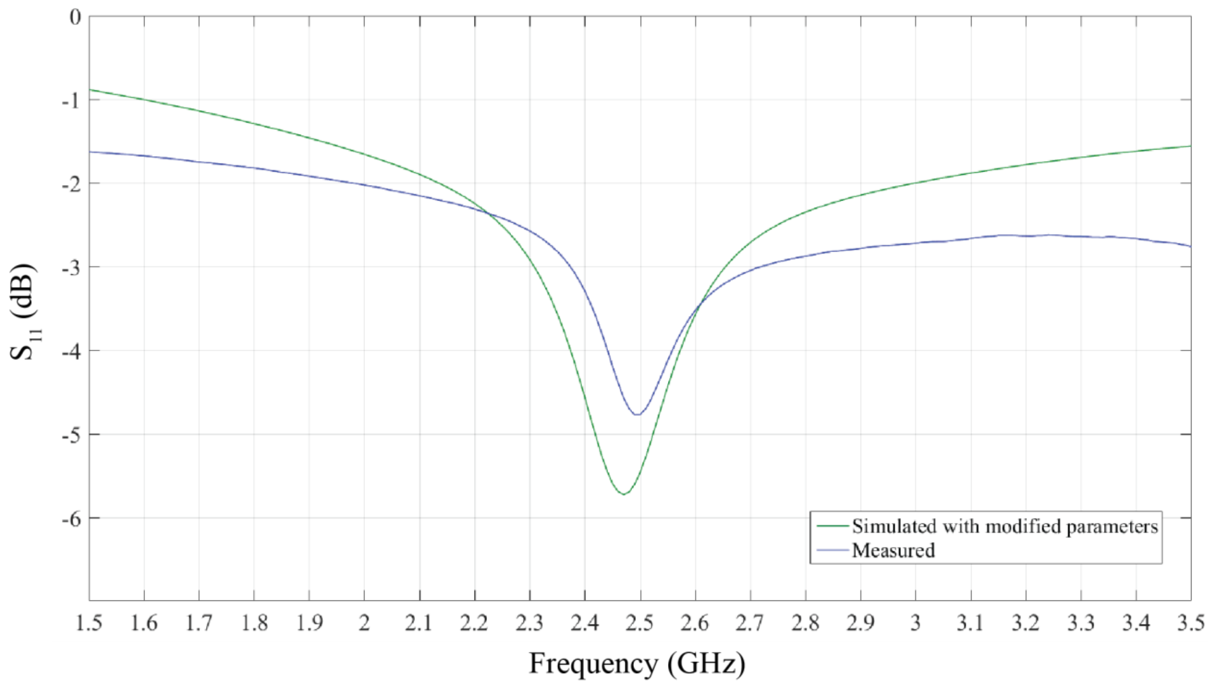

Figure 4-9. S_{11} of the simulation with the modified parameters and measurement.

Table 4-6. S_{11} obtained by the modified simulation and the measurement.

Frequency (GHz)	Simulated S_{11} (dB)	Measured S_{11} (dB)
2.47 (Resonant frequency of simulation)	-5.7	-4.6
2.49 (Resonant frequency of measurement)	-5.6	-4.8

4.4 Conclusions and Recommendations

In Experiment (II), the 2.45 GHz microstrip patch antenna was designed with the MATLAB® calculation and 3D full-wave electromagnetic field simulation. The approximate dielectric properties of the substrate was employed to ease the antenna design process. Then, the antenna and ground planes were successfully constructed by the combination of conductive inkjet printing and UV-flash sintering. The measurement revealed that the fabricated antenna had a S_{11} of -4.8 dB at 2.49 GHz, and this was significantly higher than the simulated S_{11} value of -10.3 dB at 2.42 GHz, indicating the large reflection from the fabricated antenna. On the other hand, lower S_{11} at the non-resonant frequencies was observed for the fabricated antenna, indicating the evidence of larger losses of the fabricated antenna.

There were several possibilities that the fabricated antenna showed an inferior performance to the simulation. The major reason might be the approximate estimation of the dielectric properties of the substrate. The actual dielectric constant and loss tangent might be significantly different from the typical values for PET. Another reason might be additional resistive loss due to the silver conductive epoxy paste. In a typical microstrip patch fabrication, an SMA connector is edge-mounted by high-temperature soldering, where the resistive loss of the filler material is not critical. However, in this research, the room-temperature-cured silver conductive epoxy paste was used to avoid damaging the substrate by heat.

Although all of the possibilities listed above would be the reasons for the inferior performance of the fabricated antenna, it was most likely due to the high dielectric loss of the substrate. This could be said because dielectric losses generally become more dominant at higher frequencies, whereas conductor losses become most critical at a direct current (Thierauf, 2011).

Therefore, to account for the frequency shift and larger losses of the fabricated antenna, the simulation with the measured dimension and a higher value of the loss tangent was performed. The simulation with the modified parameters gave a closer S_{11} plot to the measurement, implying that the frequency shift was due to the accuracy of the inkjet printing, and the substrate had a larger dielectric loss than the standard PET. Therefore, it was concluded that further investigations with a low-loss substrate was encouraged for a better antenna performance.

Chapter 5 EXPERIMENT (III): Investigations of the Effects of the Conductor Thickness of a 2.45 GHz Inkjet-Printed Microstrip Patch Antenna.

From Experiment (II), it was found that the fabricated inkjet-printed microstrip patch antenna had an inferior performance to the simulation because of the presence of the large losses from the conductor and dielectric substrate. However, the substrate selection for the conductive inkjet printing was quite challenging (Hutchings & Martin, 2013). The requirements for the inkjet-printable substrate include a controlled surface wettability, reasonable adhesion properties to hold inkjet-printed silver nanoparticles, and flexibility to feed into an inkjet printer. Hence, only limited numbers of inkjet-printable substrates are commercially available on the current market.

Therefore, Experiment (III) was undertaken to improve the antenna performance by decreasing the conductor loss. Firstly, a microstrip patch antenna was re-designed with a wider feed line and gaps to facilitate repetitive printing. Then, three microstrip patch antennas with different conductor thickness were fabricated by printing the antenna twice. Finally, the S_{11} of the fabricated antennas was measured by the vector network analyzer, and the effects of the conductor thickness on the S_{11} were examined. An overall flowchart is shown in Figure 5-1.

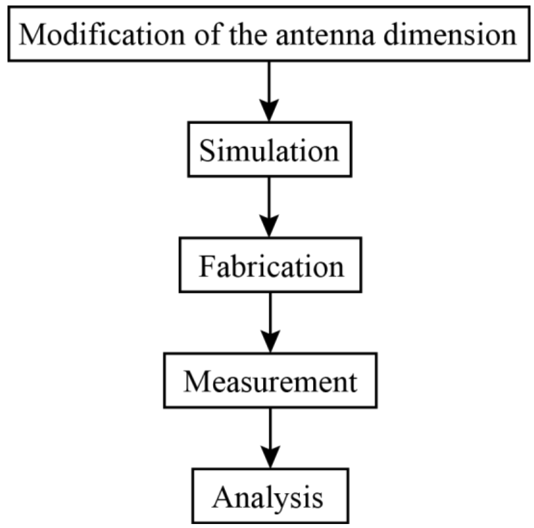

Figure 5-1. Flowchart of Experiment (III).

5.1 Research Question

The research question for Experiment (III) was if the S_{11} of a microstrip patch antenna could be improved by increasing the conductor thickness.

5.2 Experimental

5.2.1 Material selection

In this research, a single-printed and double-printed conductors were prepared to investigate the effects of the conductor thickness on S_{11}. For the single-printed conductor, the 1.0 μm-thick UV-flashed print, which was obtained in Experiment (I), was selected for its low electrical resistivity (7.5×10^{-8} Ω·m). A double-printed conductor was also prepared by the UV-flash sintering, but out of the double-printed silver ink. The thickness of the double-printed conductor was 1.5 μm measured by the SEM as shown in Figure 5-2, and the electrical resistivity was assumed to be the same as the single-printed conductor.

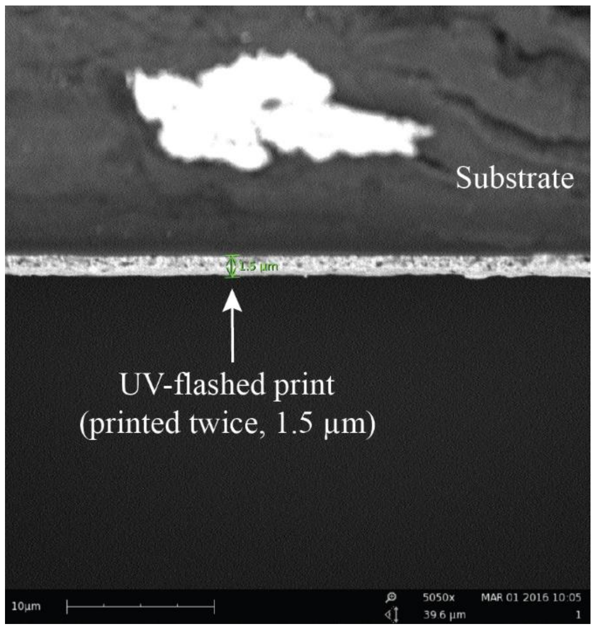

Figure 5-2. Cross section of the double-printed conductor sintered by an UV flash.

As for the substrate, the same pretreated PET film was selected for its capability of adapting the printed silver nanoparticles. Then, two pretreated PET films were superimposed with the double-sided tape in the exact same manner to Experiment (II).

5.2.2 Antenna design

In order to facilitate repetitive printing, another antenna dimension needed to be developed. During the second printing, it was not feasible to deposit the conductive ink at the exactly same location over the first print. As a consequence, the geometry of the antenna and ground planes were slightly changed by the repetition of the printing. Therefore, the antenna dimension obtained in Experiment (II) was modified to a new design with a wider feed line and gaps in order to minimize the geometrical changes caused by the repetitive printing. Having a wider feed line could be also beneficial to reduce the conductor loss for a feed line with a rough surface (Hutchings & Martin, 2013). In order to design the new antenna dimension with a wider feed line and gaps, 3D full-wave electromagnetic field simulation was repeated with CST Studio Suite®. The simulation and parameter settings were the same as the ones used in Experiment (II).

Next, in order to investigate the effect of the conductor thickness, the thickness of the antenna was modified into three different levels. The first antenna had both antenna and ground planes printed once (S-antenna), and the second antenna had both antenna and ground planes printed twice (D-antenna). The last antenna had an antenna plane printed once but a ground plane printed twice (DG-antenna). All of these three antennas had the same antenna geometry except the conductor thickness.

Table 5-1. Printing cycles.

Antenna	Printing cycle of the antenna plane	Printing cycle of the ground plane
S-antenna	1	1
D-antenna	2	2
DG-antenna	1	2

5.2.3 Fabrication

A clean ink cartridge was filled with the silver ink, and installed into the inkjet printer. Then, the antenna and ground planes were printed onto the pretreated PET film with the "best photo" and "matte paper" settings in the quality control panel for the designated cycles. The printed antenna and ground planes were dried at room temperature for 24 hours to evaporate the ink solvent.

The UV-flash sintering device was operated at 3.8 kV with a flash lamp with lower cutoff wavelength of 370 nm. The distance from the window of the lamp housing to the inkjet silver print was set to the minimum distance of 25.48 mm with the mechanical aperture of 8 mm. All the surface of the antenna and ground planes was treated by a single UV pulse for 520 μs. Then, the antenna and ground planes were superimposed to each other by the double-sided tape. To allow power supply, an SMA connector was edge-mounted on the microstrip feed line using the silver conductive epoxy paste. The silver conductive epoxy paste was cured at the room temperature for 24 hours.

5.2.4 Measurement

The vector network analyzer measured the S_{11} of the microstrip patch antennas from 1.5 to 3.5 GHz with a 50 Ω impedance load. Then, the effects of the conductor thickness were analyzed based on the return loss characteristics.

5.3 Results

Figure 5-3 displays the fabricated microstrip patch antennas with different conductor thickness.

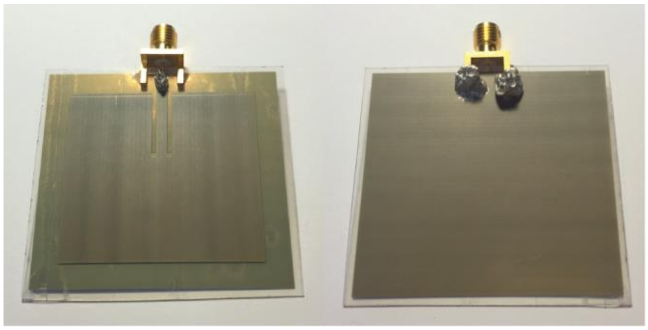

S-antenna

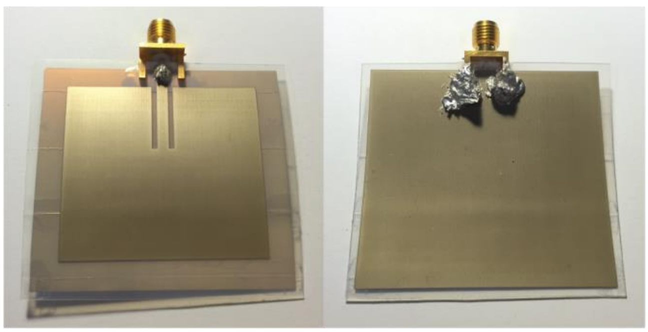

D-antenna

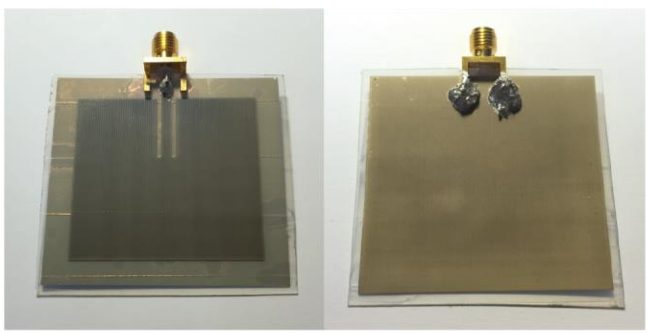

DG-antenna

Figure 5-3. Inkjet-printed microstrip patch antennas with different conductor thickness.

5.3.1 Antenna geometry

The antenna dimension was optimized with CST Studio Suite®, and is shown in Table 5-2 and Figure 5-4. It was only the gaps and feed line which became 3-4 times larger, where as other dimensions of the antenna plane kept same.

Table 5-2. Optimized antenna dimension (mm).

W_P	L_P	W_f	g	F_i	W_g	L_g
40.0	36.0	2.4	1.0	14.5	49.6	45.6

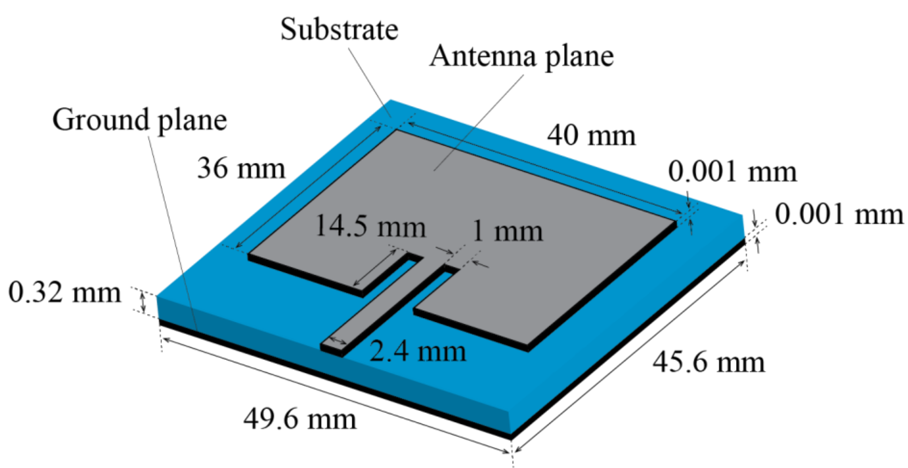

Figure 5-4. Antenna dimensions obtained by the simulation.

5.3.2 Effects of the conductor thickness

The skin depth (δ) was calculated as below:

$$\delta = \sqrt{\frac{\rho}{\pi f \mu}} = \sqrt{\frac{7.5 \times 10^{-8}}{\pi \times 2.450 \times 10^{9} \times 1.26 \times 10^{-6}}} \approx 2.8 \times 10^{-6}\ \mathrm{m} = 2.8\ \mu\mathrm{m}$$

where ρ is the electrical resistivity of the conductor, f is the frequency of the current, and μ is the permeability of the conductor, 1.26×10^{-6} H/m for pure silver (Gilmour, 1986). The skin depth of the UV-flashed print was 2.8 μm at 2.45 GHz, and this indicated that the current UV-flashed print with 1.0 μm thickness still had a limitation in terms of a high resistive loss. Because the thickness changes around/within the skin depth is very critical, the increase in conductor thickness from 1.0 μm to 1.5 μm was expected to contribute to the decrease in conductor loss. However, it could be also said that even the thickness of the double-printed conductor was not sufficient in terms of the skin depth. Ideally, the conductor should have at least a few times larger thickness than the skin depth (Sridhar et al., 2009).

Figure 5-5 shows the comparative plots of the simulated S_{11} with the different conductor thickness, and a summary of the S_{11} is shown in Table 5-3. The simulation revealed that there was a significant decrease in S_{11} from -10.4 dB to -12.6 dB by increasing the ground plane thickness, which suggested that a thicker conductor was a good approach to a better antenna performance. On the other hand, there was little difference in S_{11} between the D-antenna and DG-antenna. This indicated that it would be enough to increase the ground plane thickness, and not necessarily, both antenna and ground planes needed to be double-printed.

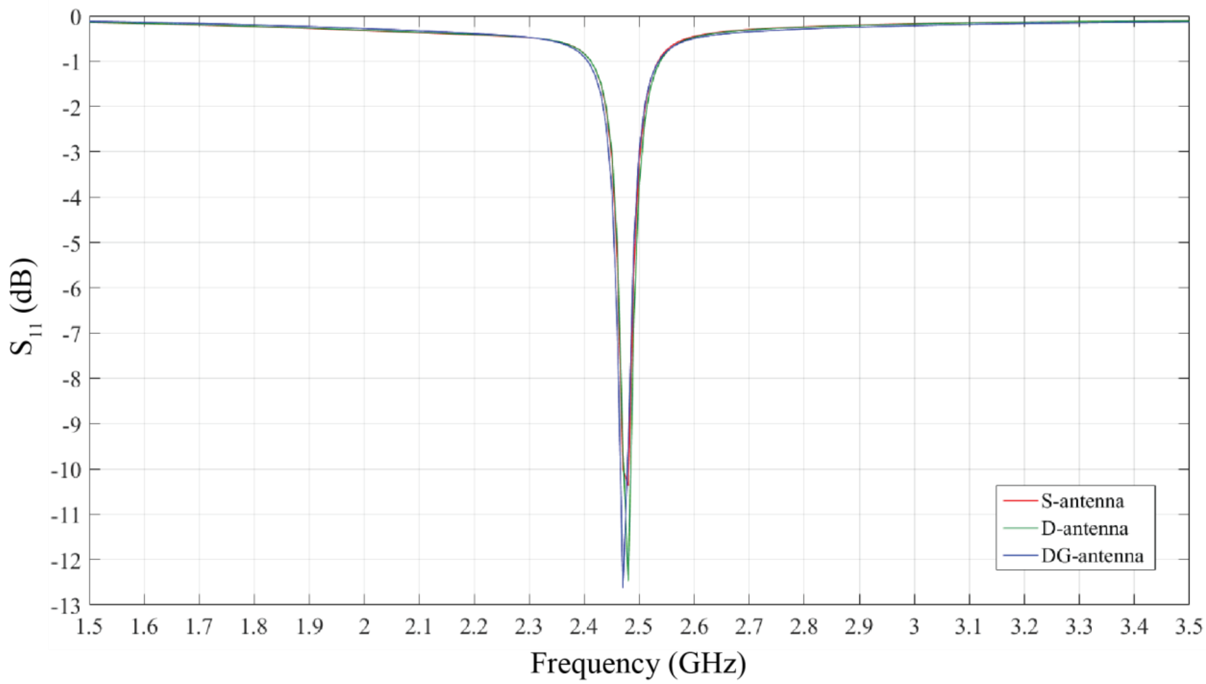

Figure 5-5. S_{11} plots obtained by the simulation with different conductor thickness.

Table 5-3. Simulated S_{11} at the resonant frequency.

Antenna	S_{11} (dB)	Resonant frequency (GHz)
S-antenna	-10.4	2.48
D-antenna	-12.5	2.48
DG-antenna	-12.6	2.47

The comparative plots of the measured S_{11} with the different conductor thickness are shown in Figure 5-6, and a summary of the S_{11} is shown in Table 5-4. From the comparison of the measured S_{11}, it was found that both of D-antenna and DG-antenna showed lower S_{11} than S-antenna, and this agreed with the simulation results. Therefore, it was shown that better S_{11}

was obtained by increasing the conductor thickness. On the other hand, the fabricated antennas had significantly different resonant frequencies from each other. Typically, a frequency shift is observed when there is a difference in antenna geometries. Thus, the frequency shift from 2.49 to 2.45 GHz between S- and DG-antennas would be due to the accuracy of the inkjet printing, as examined in Experiment (II). As for the shift from 2.49 to 2.34 GHz between S- and D-antennas, it was most likely due to the geometrical changes caused by the repetitive printing.

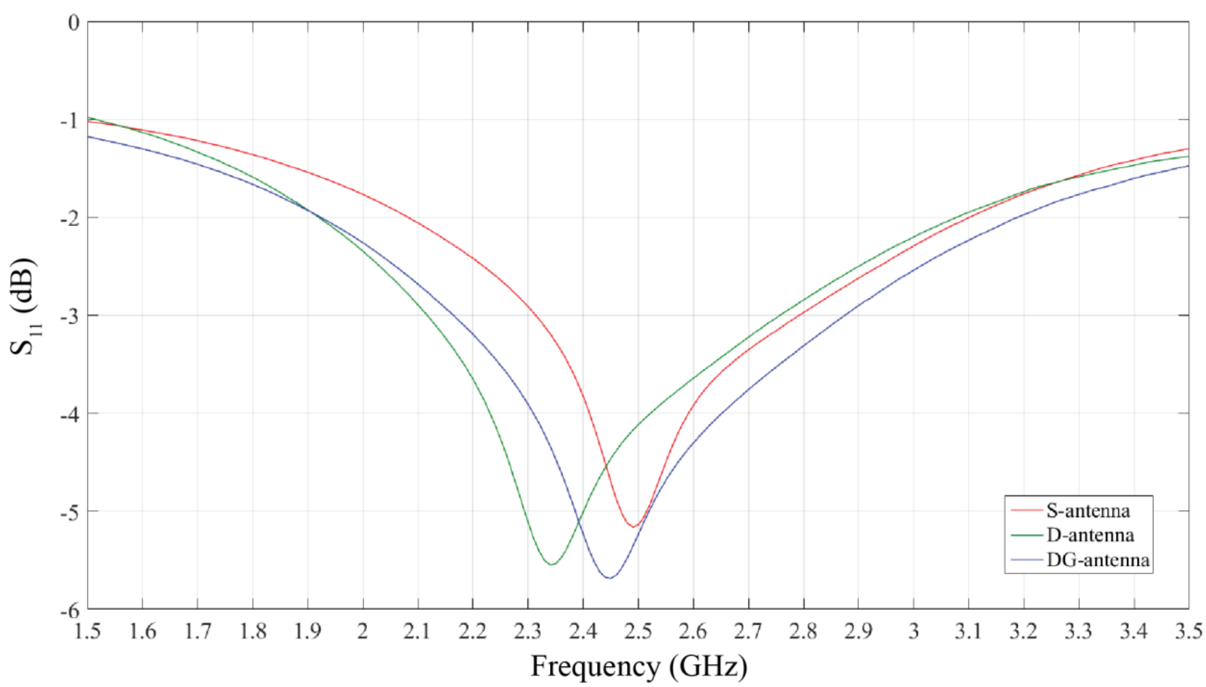

Figure 5-6. S_{11} plots obtained by the measurement with different conductor thickness.

Table 5-4. Measured S_{11} at the resonant frequency.

Antenna	S_{11} (dB)	Resonant frequency (GHz)
S-antenna	-5.2	2.49
D-antenna	-5.5	2.34
DG-antenna	-5.7	2.45

5.4 Conclusions and Recommendations

In Experiment (III), the effects of the conductor thickness on S_{11} were investigated. The skin depth calculation revealed that the UV-flashed print obtained in Experiment (I) would have a large loss at 2.45 GHz due to the skin effect. To ease this issue, it was proposed to increase the conductor thickness by repetitive printing. In order to minimize the geometrical changes caused by the second printing, the antenna design was modified into the one with wider feed line and gaps. Then, three antennas with different conductor thickness were designed and fabricated.

The simulation results showed that S_{11} was lowered from -10.4 dB to -12.6 dB by adding 0.5 μm layer of silver on the ground plane. From the measurement, S_{11} was decreased from -5.2 dB to -5.7 dB by increasing the thickness of the ground plane. Therefore, it could be concluded that a thicker conductor would be a possible approach to a better antenna performance.

Although thickness increase of the conductor demonstrated a better antenna performance, there was more space for improvement. For example, the double-printed conductor was still very thin in terms of the skin depth, and it was encouraged to have a conductor at least 5.6 to 8.4 μm in thickness (two to three times to the skin depths). However, during the fabrication process, it was experienced that further repetitions of the inkjet printing gave low adhesion of the silver nanoparticles, and as a consequence, the printed layer was blown out during the UV-flash sintering. Therefore, in order to have a sufficient conductor thickness, investigations to achieve better ink adhesion is recommended.

Chapter 6 CONCLUSIONS AND RECOMMENDATIONS

This research presented a series of experiments with the inkjet-printed microstrip patch antennas for a hyperthermia device. The first part of this research investigated the electrical properties of the printed conductors. Because the inkjet silver print had a high electrical resistivity, additional treatments, such as electroless copper plating, salt sintering, and UV-flash sintering, were incorporated to decrease the electrical resistivity. For all the treatments, statistically significant decrease in electrical resistivity was observed, and the UV-flashed print showed the lowest value of 7.5×10^{-8} Ω·m. Therefore, the UV-flashed print was chosen as the antenna conductor.

However, it needed to be noted that the copper-plated print gave the lowest electrical resistance due to the huge increase of conductor thickness after the electroless plating. Although the electroless copper plating was not successful within the current scope of this research because of the incompatible characteristics of the materials, electroless plating might be considered as an additional technique. Therefore, further investigations on electroless plating with different substrates are recommended.

The second phase of this research presented the design, fabrication, measurement and analysis of the inkjet-printed microstrip patch antenna. Firstly, the microstrip patch antenna was designed with the MATLAB® calculation and 3D full-wave electromagnetic field simulation, based on the approximate dielectric properties of the substrate for easier antenna design process. Then, the antenna and ground planes were successfully constructed by conductive inkjet printing and UV-flash sintering. The fabricated antenna had a S_{11} of -4.8 dB at 2.49 GHz, and this was significantly higher than the simulated S_{11} value of -10.3 dB at 2.42 GHz, indicating the more reflection from the fabricated antenna. On the other hand, lower S_{11} at the non-resonant frequencies was observed for the fabricated antenna, and this was the evidence of larger losses in the fabricated antenna. Several possible factors attributed for these losses include the approximate estimation of the dielectric properties and the additional resistive loss by the silver conductive epoxy. It was suggested by the additional simulation that the major loss might have come from the substrate.

Finally, the last phase of this research was incorporated to investigate the effects of the conductor thickness on the return loss. Firstly, the skin effect was considered to evaluate the conductor thickness obtained in Experiment (I), and it was suggested that the electrical resistance of the printed conductor could be decreased by having a thicker conductor. To facilitate repetitive printing, the antenna dimension needed to be modified for a wider feed line and gaps. Antennas with different antenna and/or ground plane thickness were designed and fabricated. The simulation results showed that S_{11} was lowered from -10.4 dB to -12.6 dB by adding 0.5 μm more layer of silver to the ground plane. The measurement also revealed that there was an improvement from -5.2 dB to -5.7 dB by having the thicker conductor. Therefore, it was concluded that having a thicker conductor would be a possible approach for a better antenna performance.

Although inkjet printing with a conductive ink was a method of quick, simple and high resolution at lower manufacturing costs, there were several drawbacks to be addressed. The first issue was the nozzle clogging. Because of the presence of the solid particles in the ink solution, the printer nozzles became clogged after several times of use. Hence, frequent replacement of the nozzles was required to maintain the decent printing quality. Another issue was printing accuracy as a fabrication device. Although inkjet technology itself has accurate ink deposition capability with a great droplet control, the accuracy of the printing was limited by the substrate placement and this decreased the overall printing quality especially for repetitive printing. Therefore, it is recommended to employ a better feeding method for less fabrication error.

One of the major issues encountered during this research was the selection of the substrate. Because the inkjet silver ink did not contain any adhesive substance, it was required for a substrate to have adhesive properties to hold the printed ink. In addition, there were other technical factors to be considered, including the wettability, mechanical flexibility and dielectric properties. Because of these unique requirements, printable substrates for inkjet conductive printing are limited in the current market. Investigations on the printable substrates are highly encouraged for a further implementation of a wearable hyperthermia device.

REFERENCES

Alagirusamy, R., Eichhoff J., Gries, T. & Jockenhoevel, S. (2013). Coating of conductive yarns for electro-textile applications. Journal of the Textile Institute, 104(3), 270-277.

Bahl, I., Bhartia, P., & Stuchly, S. (1980). Microstrip antennas covered with a dielectric layer. Antennas and Propagation Society International Symposium.

Balanis, C. A. (1989). Advanced engineering electromagnetics. New York, NY: Wiley.

Balanis, C. A. (1997). Antenna theory: Analysis and design (2nd ed.). Hoboken, NJ: Wiley.

Balanis, C. A. (2005). Antenna theory: Analysis and design (3rd ed.). Hoboken, NJ: Wiley.

Bancroft, R. (2009). Microstrip and printed antenna design, Raleigh, NC: SciTech.

Brooks, D. (2009). Skin effect, UP Media. Retrieved February 18, 2016, from: http://www.ultracad.com/articles/skin%20effect.pdf

Busch W. (1866). Uber den Einfluss, welchen heftigere Erysipelin zuweilig auf organisierte Neubildungen ausuben. Verhandlugen des naturhistorischen Vereines der preussischen Rheinlande und Westphalens. 23-28.

Bunch, J. S., van der Zande, A. M., Verbridge, S. S., Frank, I. W., Tanenbaum, D. M., Parpia, J. M., … McEuen, P. L. (2007). Electromechanical resonators from graphene sheets. Science, 315(5811), 490-493.

Carver, K.R., Mink, J.W. (1981). Microstrip antenna technology. IEEE Transactions on Antennas and Propagation, 29, 2-24.

Chang, S. H., Chang, C. C., & Liang, C. (2014). Improving the surface hardness and wear resistance of S45C carbon steel via various heat treatments and pH values of electroless Ni-P deposition. Engineering Materials, 1-13.

Chen, Y & Wang, C. F. (2015). Characteristic models: Theory and applications in antenna engineering. Hoboken, NJ: Wiley.

Cauchois, R., Saadaoui, M., Yakoub, A., Inal, K., Dubois-Bonvalot, B., & Fidalgo, J.-C. (2012). Impact of variable frequency microwave and rapid thermal sintering on microstructure of inkjet-printed silver nanoparticles. Journal of Materials Science, 47(20), 7110-7116.

Cheng, L. F., Ong, C. K., Neo, C. P., Varadan, V. V. & Varadan, V. K. (2004). Microwave electronics: Measurement and materials characterization, West Sussex, England: Wiley.

Collier, R. J. (2007). Microwave measurements. London, UK: Institution of Engineering and Technology.

Collin, R. E. (2001). Foundations for microwave engineering (2^{nd} ed.), New York, NY: Wiley.

Cummins, G., & Desmulliez, M. P. Y. (2012). Inkjet printing of conductive materials: A review. Circuit World, 38(4), 193-213.

Curto, S., Ramasamy, M., Suh, M., & Prakash, P. (2015). Design and analysis of a conformal patch antenna for a wearable breast hyperthermia treatment system. Energy-Based Treatment of Tissue and Assessment VIII.

Dalvi, V. H., & Rossky, P. J. (2010). Molecular origins of fluorocarbon hydrophobicity. Proceedings of the National Academy of Sciences, 107(31), 13603-13607.

Derby, B. (2010). Inkjet printing of functional and structural materials: Fluid property requirements, feature stability, and resolution. Annual Review of Materials Research, 40(1), 395-414.

Derneryd, A. G. (1978). A theoretical investigation of the rectangular microstrip antenna element. IEEE Transactions on Antennas and Propagation, 26(4), 532-535.

Dewey, W. C. (2009). Arrhenius relationships from the molecule and cell to the clinic. International Journal of Hyperthermia, 25(1), 3-20.

Dewey, W. C., Hopwood, L. E., Sapareto, S. A., & Gerweck, L. E. (1977). Cellular responses to combinations of hyperthermia and radiation. Radiology, 123(2), 463-474.

Dewhirst, M. W., Jones, E., Samulski, T., Vujaskovic, Z., Li, C., Prosnitz, L. (2003). Hyperthermia: Hyperthermia physics. In Kufe, D. W., Pollock, R. E., Weichselbaum, R.R., Bast R. C., Gansler, T. S., ……… & Frei, E, Holland, Frei Cancer medicine, New York, NY: Decker.

Dharmadasa, R., Dharmadasa, I., & Druffel, T. (2014). Intense pulsed light sintering of electrodeposited CdS thin films. Advanced Engineering Materials, 16(11), 1351-1361.

Diederich, C. J., & Hynynen, K. (1999). Ultrasound technology for hyperthermia. Ultrasound in Medicine & Biology, 25(6), 871-887.

Elliott, R. S. (2003). Antenna theory & design. Hoboken, New Jersey: Wiley.

El-Radhi, A. S., Carroll, J., & Klein, N. (2009). Clinical manual of fever in children. Berlin, Germany: Springer.

Ensminger, D. & Bond, L. J. (2011). Ultrasonics: fundamentals, technologies, and applications, 3rd ed., Boca Raton, FL: CRC Press.

Ericson, L. M., Fan, H., Peng, H., Davis, V. A., Zhou, W., Sulpizio, J., … Smalley, R. E. (2004). Macroscopic, neat, single-walled carbon nanotube fibers. Science, 305(5689), 1447-1450.

Foroughi, J., Spinks, G. M., Ghorbani, S. R., Kozlov, M. E., Safaei, F., Peleckis, G., … Baughman, R. H. (2012). Preparation and characterization of hybrid conducting polymer-carbon nanotube yarn. Nanoscale, 4(3), 940-945.

Fugetsu, B., Akiba, E., Hachiya, M., & Endo, M. (2009). The production of soft, durable, and electrically conductive polyester multifilament yarns by dye-printing them with carbon nanotubes. Carbon, 47(2), 527-530.

Garge, R., Bhartia, P., Bahl, L. & Lttipiboon., I. (2001). Microstrip antenna design handbook, Boston, MI: Artech House.

Geim, A. K. & Novoselov, K. S. (2007). The rise of graphene. Nature Materials, 6, 183-191.

German, R. M. (2010). Thermodynamics of sintering. In Z. Z. Fang (Ed.), Sintering of advanced materials, Cambridge, UK: Woodhead.

German, R. M. (2014). Sintering: From empirical observations to scientific principles. Oxford: Elsevier, 413-432.

Ghali, E. (2010). Corrosion resistance of aluminum and magnesium alloys: Understanding performance, and testing, Hoboken, NJ: Wiley.

Gilchrist, R. K., Medal, R., Sorey, W. D., Hanselman, R. C., parrott, J. C. & Taylor, C. B. (1957). Selective inductive heating of lymph nodes. Annals of Surgery, 146(4), 596-606.

Gilmour, A. S. (1986). Microwave tubes. Dedham, MA: Artech House.

Glisson, T. H., Jr. (2011). Introduction to circuit analysis and design. Raleigh, NC: Springer.

Gordon, R., Hines, J., & Gordon, D. (1979). Intracellular hyperthermia a biophysical approach to cancer treatment via intracellular temperature and biophysical alterations. Medical Hypotheses, 5(1), 83-102.

Grieg, D. D., & Engelmann, H. F. (1952). Microstrip-a new transmission technique for the klilomegacycle range. Proceedings of the IRE, 40(12), 1644-1650.

Gupta, A. K., & Gupta, M. (2005). Synthesis and surface engineering of iron oxide nanoparticles for biomedical applications. Biomaterials, 26(18), 3995-4021.

Haemmerich, D., & Wood, B. J. (2006). Hepatic radiofrequency ablation at low frequencies preferentially heats tumour tissue. International Journal of Hyperthermia, 22(7), 563-574.

Haemmerich, D., & Schutt, D. J. (2011). RF ablation at low frequencies for targeted tumor heating: In vitro and computational modeling results. IEEE Transactions on Biomedical Engineering IEEE Transaction on Biomedical Engineering, 58(2), 404-410.

Hammerstad, E. O. (1975). Equations for microstrip circuit design. 1975 5th European Microwave Conference, 268-272.

Huang, Y., & Boyle, K. (2008). Antennas: From theory to practice. Chichester, UK: Wiley.

Huang, L., Huang, Y., Liang, J., Wan, X., & Chen, Y. (2011). Graphene-based conducting inks for direct inkjet printing of flexible conductive patterns and their applications in electric circuits and chemical sensors. Nano Research, 4(7), 675-684.

Hutchings, I. M., & Martin, G. (2013). Inkjet technology for digital fabrication, West Sussex: UK: Wiley.

Hurwitz, M. D., Kaplan, I. D., Hansen, J. L., Prokopios-Davos, S., Topulos, G. P., Wishnow, K., … Hynynen, K. (2005). Hyperthermia combined with radiation in treatment of locally advanced prostate cancer is associated with a favourable toxicity profile. International Journal of Hyperthermia, 21(7), 649-656.

Jayasinghe, C., Chakrabarti, S., Schulz, M. J., & Shanov, V. (2011). Spinning yarn from long carbon nanotube arrays. Journal of Materials Research, 26(05), 645-651.

Ji, H., Chen, G., Hu, J., Wang, M., Min, C., & Zhao, Y. (2013). Biomimetic superhydrophobic surfaces. Journal of Dispersion Science and Technology, 34(1), 1-21.

Kappe, C. O., Dallinger, D. & Murphree, S. S. (2009). Practical microwave synthesis for organic chemists. Darmstadt, Germany: Wiley.

Kao, C., & Chou, K. (2007). Electroless copper plating onto printed lines of nanosized silver seeds. Electrochemical and Solid-State Letters, 10(3), D32-D34.

Kazani, I., Hertleer, C., De Mey, G., Schwarz, A., Guxho, G. & Van Langenhove, L. (2012). Electrical conductive textiles obtained by screen printing. Fibers and Textiles in Eastern Europe 20, 1(90) 57-63.

Khumpuang, S., Miyake, K. & Itoh, T. (2011). Characterization of a SWNT-reinforced conductive polymer and patterning technique for application of electronic textile. Sensors and Actuators A: Physical, 169, 378-382.

Kim, B., Koncar, V., Devaux, E., Dufour, C., & Viallier, P. (2004). Electrical and morphological properties of PP and PET conductive polymer fibers. Synthetic Metals, 146(2), 167-174.

Kim, K. S., Hernandez, D. & Lee, S. Y. (2015) Time-multiplexed two-channel capacitive radiofrequency hyperthermia with nanoparticle mediation. Biomedical Engineering Online, 14(1), 1-15.

Kozissnik, B., Bohorquez, A. C., Dobson, J., & Rinaldi, C. (2013). Magnetic fluid hyperthermia: Advances, challenges, and opportunity. International Journal of Hyperthermia, 29(8), 706-714.

Krucińska, I., Skrzetuska, E., & Urbaniak-Domagała, W. (2011). The use of carbon nanotubes in textile printing. Journal of Applied Polymer Science, 121(1), 483-490.

Krucińska, I., Skrzetuska, E. & Urbaniak-Domagała, W. (2012). Prototypes of carbon nanotube-based textile sensors manufactured by the screen printing method. Fibers and Textiles in Eastern Europe, 20, 2(91), 79-83.

Krucińska, I., Surma, B., Chrzanowski, M. (2010). Study on sensing properties of electro-spun PEO/MWNT non-woven fabric. Research Journal of Textile and Apparel. 89-96.

Kumar, G. & Ray, K. P. (2003). Broadband microstrip antennas. Artech House Print on Demand.

Layani, M., Grouchko, M., Shemesh, S., & Magdassi, S. (2012). Conductive patterns on plastic substrates by sequential inkjet printing of silver nanoparticles and electrolyte sintering solutions. Journal of Materials Chemistry, 22(29), 14349-14352.

Lee, J. H., Jang, J., Choi, J., Moon, S. H., Noh, S., Kim, J., … Cheon, J. (2011). Exchange-coupled magnetic nanoparticles for efficient heat induction. Nature Nanotechnology, 6(7), 418-422.

Lepró, X., Lima, M. D., & Baughman, R. H. (2010). Spinnable carbon nanotube forests grown on thin, flexible metallic substrates. Carbon, 48(12), 3621-3627.

Liang, P., Yu, X. L. & Yu, J. (2015). Microwave ablation treatment of solid tumors. (2015). Dordrecht, Netherlands: Springer.

Li, D. & Kaner, R. B. (2008). Graphene-based materials. Science, 320, 1170-1171.

Li, F., & Pan, J. (2012). Modelling "nano-effects" in sintering. Engineering Materials. 35.

Lii, D. F., Huang, J. L., Tsui, L. J., & Lee, S. M. (2002). Formation of BN films on carbon fibers by dip-coating. Surface and Coatings Technology, 150(2-3), 269-276.

Li, X. H., Rong, P. F., Jin, H. K., Wang, W. & Tan, J.T. (2011). Magnetic fluid hyperthermia induced by radiofrequency capacitive field for the treatment of transplanted subcutaneous tumors in rats. Experimental and Therapeutic Medicine, 3(2), 279-284.

Lin, Z., Le, T., Song, X., Yao, Y., Li, Z., Moon, K., … Wong, C. (2013). Preparation of water-based carbon nanotube inks and application in the inkjet printing of carbon nanotube gas sensors. Journal of Electronic Packaging, 135(1), 011001.

Lo, Y. T., Solomon, D. & Richards, W. F. (1979). Theory and experiment on microstrip antennas. IEEE Transactions on Antennas and Propagation, 27(2), 137-145.

Locher, I & Troster, G. (2007). Screen-printed textile transmission lines. Textile Research Journal, 77(11), 837-842.

Losito, O. & Dimiccoli, V. (2012). Traveling planar wave antenna for wireless communications. In Eksim, A., Wireless communications and networks: recent advances, published online: Intech. Retrieved January 09, 2016, from: http://www.intechopen.com/books/wireless-communications-and-networks-recent-advances/travelling-planar-wave-antenna-for-wireless-communications

Lou, C. W. (2005). Process of complex core spun yarn containing a metal wire. Textile Research Journal, 75(6), 466-473.

Lyth, S. M., & Silva, S. R. P. (2015). Electron field emission from water-based carbon nanotube inks. ECS Journal of Solid State Science and Technology, 4(4), P3034-P3043.

Ma, G., & Jiang, G. (2010). Review of tumor hyperthermia technique in biomedical engineering frontier. 3rd International Conference on Biomedical Engineering and Informatics.

Ma, S., Bromberg, V., Liu, L., Egitto, F. D., Chiarot, P. R., & Singler, T. J. (2014). Low temperature plasma sintering of silver nanoparticles. Applied Surface Science, 293, 207-215.

Ma, S., Wang, Y., Min, Z., & Zhong, L. (2013). Intrinsically conducting polymer-based fabric strain sensors. Polymer International, 62, 983-990.

Magdassi, S., Grouchko, M., Berezin, O. & Kamyshny, A. (2010), Triggering the sintering of silver nanoparticles at room temperature, American Chemical Society, 4(4), 1943-1948.

Mallory, G. O. & Hajdu, J. B. (1990). Electroless plating: fundamentals and applications. Norwich, New York: Noyes Publications.

Matin, M. A. & Sayeed, A. I. (2010). A design rule for inset-fed rectangular microstrip patch antenna. WSEAS Transactions on Communications. 9(1), 63-72.

National Cancer Institute. (2011). Hyperthermia in cancer treatment. Retrieved January 09, 2016, from: http://www.cancer.gov/cancertopics/treatment/types/surgery /hyperthermia-fact-sheet#r1

Ohguri, T., Yahara, K., Moon, S. D., Yamaguchi, S., Imada, H., Terashima, H., & Korogi, Y. (2011). Deep regional hyperthermia for the whole thoracic region using 8 MHz radiofrequency-capacitive heating device: Relationship between the radiofrequencyoutput power and the intra-oesophageal temperature and predictive factors for a good heating in 59 patients. International Journal of Hyperthermia, 27(1), 20-26.

Olkkonen, J., Leppaeniemi, J., Mattila, T., & Eiroma, K. (2014). Sintering of inkjet printed silver tracks with boiling salt water. Journal of Materials Chemistry C, 2(18), 3577-3582.

Pang, C. L. K. (2016). Hyperthermia in oncology. Boca Raton, FL: CRC Press.

Park, H. Y., Kang, B. J., Lee, D., & Oh, J. H. (2013). Control of surface wettability for inkjet printing by combining hydrophobic coating and plasma treatment. Thin Solid Films, 546, 162-166.

Park, J., & Lee, K. H. (2012). Carbon nanotube yarns. Korean Journal of Chemical Engineering, 29(3), 277-287.

Parkinson, R. (1997). Properties and applications of electroless nickel, Toronto, Canada: Nickel Development Institute. Retrieved November 01, 2015, from: http://www.nickelinstitute.org/~/Media/Files/TechnicalLiterature /PropertiesAndApplicationsOfElectrolessNickel_10081_.pdf

Paul, G., Torah, R., Beeby, S, Yang, K. & Tudor, J. (2014). An investigation into the durability of screen-printed conductive tracks on textiles. Measurement Science and Technology, 25, 1-11.

Paul, G., Torah, R., Beeby, S. & Tudor, J. (2014) The development of screen printed conductive networks on textiles for biopotential monitoring applications, Sensors and Actuators A, 206, 35-41.

Pelosi, G. (2014). A Tribute to James Clerk Maxwell on the 150th Anniversary of His Equations (1864-2014). IEEE Antennas and Propagation Magazine, 56(6), 295-298.

Petukhov, D. I., Kirikova, M. N., Bessonov, A. A. & Bailey, M. J. A. (2014). Nickel and copper conductive patterns fabricated by reactive inkjet printing combined with electroless plating. Materials Letters, 132, 302-306.

Perelaer, J., Klokkenburg, M., Hendriks, C. E. and Schubert, U. S. (2009), Microwave flash sintering of inkjet-printed silver tracks on polymer substrates, Advanced Materials, 21(47), 4830-4.

Perelaer, J., Abbel, R., Wunscher, S., Jani, R., van Lammeren, T. and Schubert, U.S. (2012), Roll-to-roll compatible sintering of inkjet printed features by photonic and microwave exposure: from non-conductive ink to 40% bulk silver conductivity in less than 15 seconds, Advanced Materials, 24(19), 2620-5.

Perinka, N., Kim, C. H., Kaplanova, M., & Bonnassieux, Y. (2013). Preparation and characterization of thin conductive polymer films on the base of pedot:pss by ink-jet printing. Physics Procedia, 44, 120-129.

Poulou, L. S., Botsa, E., Thanou, I. Ziakas, P. D. & Thanos, L. (2015). Percutaneous microwave ablation vs radiofrequency ablation in the treatment of hepatocellular carcinoma. World Journal of Hepatology, 7(8), 1054.

Pozar, D. M. (1990). Rigorous closed-form expressions for the surface wave loss of printed antennas. Electronics Letters, 26(13), 954.

Rahaman, M. N. (2010). Kinetics and mechanism of densification. In Z. Z. Fang (Ed.), Sintering of advanced materials, Cambridge, UK: Woodhead.

Romaguera, Madec, & Yeates (2009). Inkjet printing of conductive materials for smart textiles and flexible electronics. MRS Proceedings, 1192.

Qin, G., & Watanabe, A. (2014). Conductive network structure formed by laser sintering of silver nanoparticles. Journal of Nanoparticle Research, 16(11).

Saito, K., Takahashi, M., & Ito, K. (2013). Generation of controllable heating patterns for interstitial microwave hyperthermia by coaxial-dipole antennas. IEICE Transactions on Electronics, E96.C(9), 1178-1183.

Salahi, S., Maccarini, P. F., Rodrigues, D. B., Etienne, W., Landon, C. D., Inman, B. A., … Stauffer, P. R. (2012). Miniature microwave applicator for murine bladder hyperthermia studies. International Journal of Hyperthermia, 28(5), 456-465.

Salunkhe, A. B., Khot, V. M., & Pawar, S. H. (2014). Magnetic hyperthermia with magnetic nanoparticles: A status review. Current Topics in Medicinal Chemistry, 14(5), 572-594.

Sandmann, A., Notthoff, C., & Winterer, M. (2013). Continuous wave ultraviolet-laser sintering of ZnO and TiO2 nanoparticle thin films at low laser powers. Journal of Applied Physics, 113(4), 044310.

Sankaralingam, S., & Gupta, B. (2010). Determination of dielectric constant of fabric materials and their use as substrates for design and development of antennas for wearable applications. IEEE Transactions on Instrumentation and Measurement, 59(12), 3122-3130.

Schwarz, A., Kazani, I., Cuny, L., Hertleer, C., Ghekiere, F., De Clercq, G., ... Van Langenhove, L. (2011). Electro-conductive and elastic hybrid yarns–the effects of stretching, cyclic straining and washing on their electro-conductive properties. Materials & Design, 32(8-9), 4247-4256.

Schmuki, P., & Virtanen, S. (2009). Electrochemistry at the nanoscale: Nanostructure science and technology. New York, NY: Springer.

Seeberg, T. M., Røyset, A., Jahren, S., & Strisland, F. (2011). Printed organic conductive polymers thermocouples in textile and smart clothing applications. 2011 Annual International Conference of the IEEE Engineering in Medicine and Biology Society.

Simo, K. A., Tsirline, V. B., Sindram, D., McMillan, M. T., Thompson, K. J., Swan, R. Z., … Iannitti, D. A. (2013). Microwave ablation using 915-MHz and 2.45-GHz systems: what are the differences, HPB, 15(12), 991-996.

Soares, I. P. P., Ferreira, M. M. I., Igreja, A. G. B. N. R, Novo, M. M. C., & Borges, P.M.R. J. (2012). Application of hyperthermia for cancer treatment: Recent patents review. PRA, 7(1), 64-73.

Society of Interventional Radiology. (2015). Nonsurgical treatments for metastatic cancer in bones. Retrieved September 10, 2015, from: http://www.sirweb.org/patients/bone-cancer/

Sridhar, A., Reiding, J., Adelaar, H., Achterhoek, F., Dijk, D. J., & Akkerman, R. (2009). Inkjet-printing- and electroless-plating-based fabrication of RF circuit structures on high-frequency substrates. Journal of Micromechanics and Microengineering, 19(8), 085020.

Suarez, M., Fernandez, A., Menendez, J. L., Torrecillas, R., U., H., Hennicke, J., … Kessel, T. (2013). Challenges and opportunities for spark plasma sintering: A key technology for a new generation of materials. In B. Ertuğ (Ed.), Sintering applications (pp. 319-342), published online: Intech. Retrieved May 22, 2015, from: http://www.intechopen.com/books/sintering-applications/challenges-and-opportunities-for-spark-plasma-sintering-a-key-technology-for-a-new-generation-of-mat

Sugitani, T., Kubota, S., Kuroki, S., Sogo, K., Arihiro, K., Okada, M., … Kikkawa, T. (2014). Complex permittivities of breast tumor tissues obtained from cancer surgeries. Applied Physics Letters, 104(25), 253702.

Suh, M. (2011). Development of wireless transmission between inductively coupled layers in smart clothing. Unpublished doctoral dissertation, North Carolina State University, Raleigh, NC. Retrieved November 21, 2014 from: http:www.lib.ncsu.edu/resolver /1840.16/7758

Suh, M., Carroll, K. E., Grant, E., & Oxenham, W. (2013). Effect of fabric substrate and coating material on the quality of conductive printing. Journal of the Textile Institute, 104(2), 213-222.

Shirakawa, H., Louis, E. J., MacDiarmid, A. G., Chiang, C. K., & Heeger, A. J. (1977). Synthesis of electrically conducting organic polymers: Halogen derivatives of polyacetylene, (CH)x. Journal of Chemical Society, Chemical Communication, (16), 578.

Tang, S. L. P., & Stylios, G. K. (2006). An overview of smart technologies for clothing design and engineering. International Journal of Clothing Science and Technology, 18(2), 108-128.

Tang, Y., & McGoron, A. J. (2010). The role of temperature increase rate in combinational hyperthermia chemotherapy treatment. Biophotonics and Immune Responses V.

Thierauf, S. T. (2011). Understanding signal integrity. Norwood, MA: Artech House.

Topsakal, E., Asili, M., Chen, P., Demirci, U., & Younan, N. (2014). Flexible microwave antenna applicator for chemothermotherapy of the breast. Proceedings of the 4th International Conference on Wireless Mobile Communication and Healthcare - Transforming Healthcare through Innovations in Mobile and Wireless Technologies.

Van der Zee, J. (2002). Heating the patient: a promising approach. Annals of Oncology, 13(8), 1173-1184.

Van der Zee, J., González, D., Van Rhoon, G. C., Van Dijk, J. D., Van Putten, W. L., & Hart, A. A. (2000). Comparison of radiotherapy alone with radiotherapy plus hyperthermia in locally advanced pelvic tumours: a prospective, randomised, multicentre trial. The Lancet, 355(9210), 1119-1125.

Varnaite-Zuravliova, S., Kavaliauskiene, L., Baltusnikaite, J., Valaseviciute, L., & Verbiene, R. (2014). Investigation of shielding properties of yarns, twisted with metal wire.

Materials Science, 20(1).

Vasilantone, M. (1969). US Patent No. US3427964A. United States Patent and Trademark Office.

Vernon, C., Hand, J., Field, S., Machine, D., Whaley, J., … Vandijk, J. (1996). Radiotherapy with or without hyperthermia in the treatment of superficial localized breast cancer: Results from five randomized controlled trials. International Journal of Radiation Oncology Biology Physics, 35(4), 731-744.

Vigolo, B. Penicaud, A., Coulon, C., Sauder, C., Pailler, R., Journet, C., … Poulin, P. (2000). Macroscopic fibers and ribbons of oriented carbon nanotubes. Science, 290(5495), 1331-1334.

Visser, H. J. (2012). Antenna Theory and Applications, West Sussex, U.K.: Wiley.

Volkman, S. K., Yin, S., Bakhishev, T., Puntambekar, K., Subramanian, V., & Toney, M. F. (2011). Mechanistic studies on sintering of silver nanoparticles. Chemistry of Materials, 23(20), 4634-4640.

Wang, L., Yin, D., Li, M., & Li, L. (2014). Microstrip near-field focusing for microwave non-invasive breast cancer thermotherapy. 2014 XXXIth URSI General Assembly and Scientific Symposium (URSI GASS).

Warren, S. L. (1935). Preliminary study of the effect of artificial fever upon hopeless tumor cases. American Journal of Roentgenol, 33, 75-87.

Wei, X. & Roper, D. K. (2014). Tin sensitization for electroless plating review. Electrochemical Society, 161(5), D235-D242.

Wypych, G. (2012). Handbook of polymers. Toronto, Canada: ChemTech.

Wu, J. T., Hsu, S. L. C., Tsai, M. H. & Hwang W. S. (2010). Direct inkjet printing of silver nitrate/poly (N-vynyl-2-pyrrolidone) inks to fabricate silver conductive lines, Journal of Physical Chemistry C, 114, 4659-4662.

Zapka, W., Voit, W., Loderer, C. & Lang, P. (2008). Low temperature chemical post-treatment of inkjet printed nano-particle silver inks. Digital Fabrication, 906-911.

Zorbas, G., & Samaras, T. (2014). Simulation of radiofrequency ablation in real human anatomy. International Journal of Hyperthermia, 30(8), 570-578.

Zubir, F., Rahim, M. K. A., Ayop, O. B., & Majid, H. A. (2010). Design and analysis of microstrip reflectarray antenna with minkowski shape radiating element. Progress in Electromagnetics Research B, 24, 317-331.

APPENDICES

Appendix A. Print designs for Experiment (I)

The print designs used in Experiment (I) are shown below.

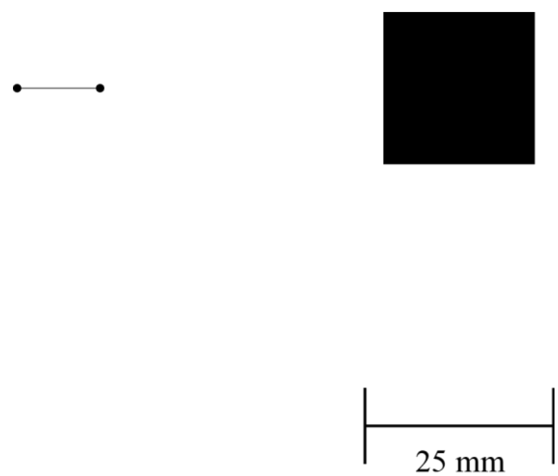

Appendix B. Electrical resistance of the conductive prints

Electrical resistance of the conductive prints (0.1 mm × 10 mm) on PET film (n=20).

Inkjet silver print (Ω)	Copper-plated print (Ω)	Salt-sintered print (Ω)	UV-flashed print (Ω)
47.6	4.7	39.8	7.6
44.9	6.6	40.1	7.6
46.0	4.3	37.7	7.8
46.1	3.5	36.1	7.3
45.8	3.4	35.2	7.7
46.9	3.4	40.4	7.5
47.0	3.3	35.6	7.4
48.9	3.6	40.2	7.3
48.8	4.9	39.7	7.5
47.5	4.6	38.4	7.2
49.5	6.0	38.3	7.4
46.0	4.8	40.9	7.5
45.6	5.3	37.2	7.4
46.6	4.2	35.8	7.4
45.3	2.8	33.4	7.5
45.8	7.6	36.9	7.4
45.9	4.1	37.5	7.4
45.2	3.4	40.4	7.9
48.6	3.1	34.5	7.4
47.1	5.7	39.5	7.8

Appendix C. Electrical resistivity of the conductive prints

Electrical resistivity of the conductive prints (0.1 mm × 10 mm) on PET film (n=20).

Inkjet-silver print (Ω·m)	Copper-plated print (Ω·m)	Salt-sintered print (Ω·m)	UV-flashed print (Ω·m)
6.2×10^{-7}	2.1×10^{-7}	5.6×10^{-7}	7.6×10^{-8}
5.8×10^{-7}	3.0×10^{-7}	5.6×10^{-7}	7.6×10^{-8}
6.0×10^{-7}	1.9×10^{-7}	5.3×10^{-7}	7.8×10^{-8}
6.0×10^{-7}	1.6×10^{-7}	5.1×10^{-7}	7.3×10^{-8}
6.0×10^{-7}	1.5×10^{-7}	4.9×10^{-7}	7.7×10^{-8}
6.1×10^{-7}	1.5×10^{-7}	5.7×10^{-7}	7.5×10^{-8}
6.1×10^{-7}	1.5×10^{-7}	5.0×10^{-7}	7.4×10^{-8}
6.4×10^{-7}	1.6×10^{-7}	5.6×10^{-7}	7.3×10^{-8}
6.3×10^{-7}	2.2×10^{-7}	5.6×10^{-7}	7.5×10^{-8}
6.2×10^{-7}	2.0×10^{-7}	5.4×10^{-7}	7.3×10^{-8}
6.4×10^{-7}	2.7×10^{-7}	5.4×10^{-7}	7.4×10^{-8}
6.0×10^{-7}	2.2×10^{-7}	5.7×10^{-7}	7.5×10^{-8}
5.9×10^{-7}	2.4×10^{-7}	5.2×10^{-7}	7.4×10^{-8}
6.1×10^{-7}	1.9×10^{-7}	5.0×10^{-7}	7.4×10^{-8}
5.9×10^{-7}	1.3×10^{-7}	4.7×10^{-7}	7.5×10^{-8}
6.0×10^{-7}	3.4×10^{-7}	4.2×10^{-7}	7.4×10^{-8}
6.0×10^{-7}	1.9×10^{-7}	5.3×10^{-7}	7.4×10^{-8}
5.9×10^{-7}	1.5×10^{-7}	5.7×10^{-7}	7.9×10^{-8}
6.3×10^{-7}	1.4×10^{-7}	4.8×10^{-7}	7.4×10^{-8}
6.1×10^{-7}	2.6×10^{-7}	5.5×10^{-7}	7.8×10^{-8}

Appendix D. MATLAB® Code

The MATLAB® code used for the antenna size calculation was written based on the empirical formulas (Equations 2-10 to 2-14 and 2-23 to 2-33). The full code is shown below:

```
% Microstrip patch antenna size calculation
clear all
format long
er = input('Dielectric constant: ');
h = input('Substrate thickness(in mm): ');
f = input('Frequency(in GHz): ');
z_in = input('Input impedance(in ohms): ');
disp('Please wait...');
f = f*1e9;

% Calculate the width of the patch
Wp = ((2.998e8/(2*f))*sqrt(2/(er+1)))*1000;

% Calculate the effective dielectric constant
e_eff = ((er+1)/2)+(((er-1)/2)*(1+(12*h/Wp))^-0.5);
```

```
% Calculate the extension length
del_l = (((e_eff+0.3)*((Wp/h)+0.264))/((e_eff-0.258)*((Wp/h)+0.8)))*(0.412*h);

% Calculate the effective length
l_eff = (2.998e8/(2*f*sqrt(e_eff)))*1000;

% Calculate the lemgth of the patch
Lp = l_eff-(2*del_l);

%Calculate the conductance g1
k0 = (2*pi*f)/(2.998e8*1000);
x = k0*Wp;
I = -2+cos(x)+(x*sinint(x))+(sin(x)/x);
g1 = I/(120*pi*pi);

% Calculate the conductance g12
a = @(th)(((sin((x./2).*cos(th))./cos(th)).^2).*(besselj(0,(k0.*Lp.*sin(th)))).*(sin(th)).^3);
g12 = integral(a,0,pi)/(120*pi*pi);

% Calculate the resonant input resistance
r_in = 1/(2*(g1+g12));
```

```
% Calculate the inset feed

Fi = (Lp/pi)*(acos(sqrt(z_in/r_in)));


% Calculate the minimum size of the ground plane

Lg_min = 6*h+Lp;

Wg_min = 6*h+Wp;


% Calculate the width of the feed line

B = 377*pi/(2*z_in*sqrt(er));

m1 = 2*B-1;

m = log(m1);

n1 = B-1;

n = log(n1);

Wf = ((2*h)/pi)*(B-1-m+((er-1)/(2*er)*(n+0.39-(0.61/er))));


% Calculate the gap

g = (2.998e8*4.65e-9)/(sqrt(2*e_eff)*f*10^-9);


disp('Rectangular microstrip patch antenna:');

disp(['Width of the patch (Wp) is: ',num2str(Wp),' mm']);

disp(['Length of the patch(Lp) is: ',num2str(Lp),' mm']);
```

```
disp(['Inset feed (Fi) is: ',num2str(Fi),' mm']);

disp(['Gap (g) is: ',num2str(g),' mm']);

disp(['With of the feed line(Wf)is: ',num2str(Wf),' mm']);

disp(['Minimum length of the ground plane is: ',num2str(Lg_min),' mm']);

disp(['Minimum width of the ground plane is: ',num2str(Wg_min),' mm']);
```

Appendix E. Print designs for Experiment (II)

The print designs used for the antenna fabrication are shown below.

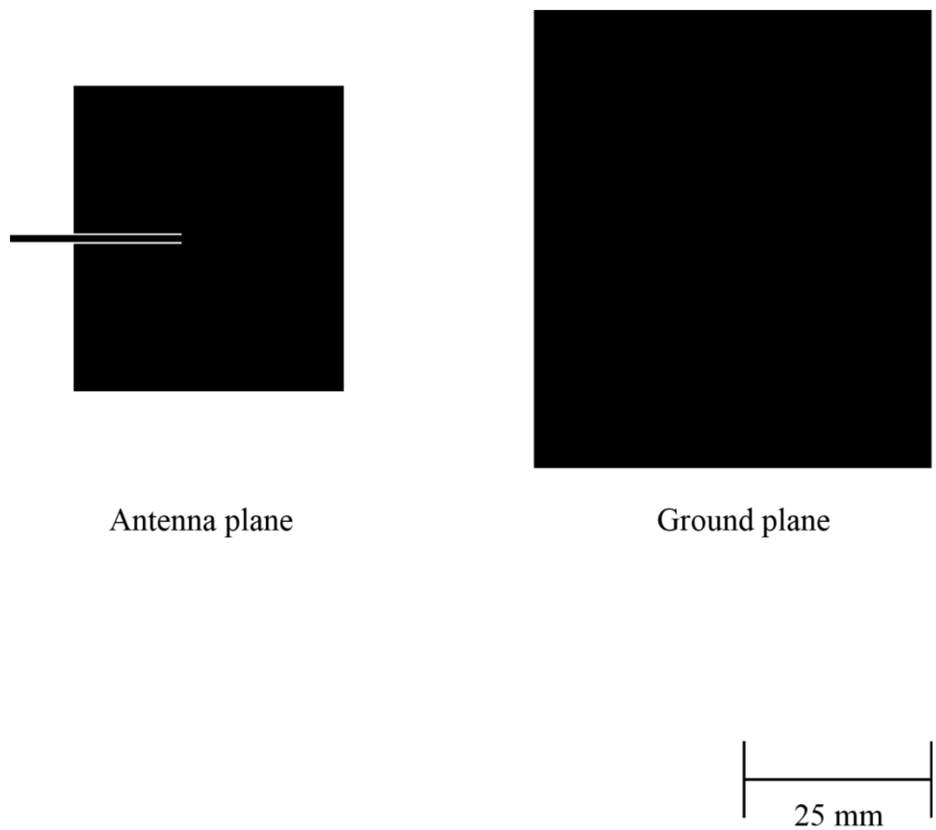

Appendix F. Simulation and measurement results for Experiment (II)

Simulated and measured S_{11}.

Frequency (GHz)	Simulated S_{11} (dB)	Measured S_{11} (dB)	Simulated S_{11} (dB) with modified parameters	Frequency (GHz)	Simulated S_{11} (dB)	Measured S_{11} (dB)	Simulated S_{11} (dB) with modified parameters	Frequency (GHz)	Simulated S_{11} (dB)	Measured S_{11} (dB)	Simulated S_{11} (dB) with modified parameters
1.50	-0.234	-1.628	-0.886	2.17	-0.500	-2.258	-2.124	2.84	-0.518	-2.827	-2.257
1.51	-0.235	-1.633	-0.897	2.18	-0.511	-2.276	-2.163	2.85	-0.516	-2.819	-2.236
1.52	-0.236	-1.639	-0.909	2.19	-0.523	-2.294	-2.204	2.86	-0.513	-2.813	-2.217
1.53	-0.237	-1.642	-0.920	2.20	-0.537	-2.314	-2.247	2.87	-0.511	-2.804	-2.198
1.54	-0.238	-1.646	-0.932	2.21	-0.552	-2.334	-2.294	2.88	-0.509	-2.798	-2.180
1.55	-0.239	-1.653	-0.944	2.22	-0.568	-2.356	-2.343	2.89	-0.507	-2.792	-2.163
1.56	-0.240	-1.658	-0.956	2.23	-0.588	-2.377	-2.396	2.90	-0.505	-2.783	-2.146
1.57	-0.242	-1.660	-0.968	2.24	-0.609	-2.399	-2.454	2.91	-0.504	-2.773	-2.129
1.58	-0.243	-1.665	-0.980	2.25	-0.634	-2.424	-2.516	2.92	-0.502	-2.765	-2.113
1.59	-0.245	-1.672	-0.993	2.26	-0.664	-2.449	-2.583	2.93	-0.501	-2.758	-2.098
1.60	-0.246	-1.677	-1.005	2.27	-0.699	-2.478	-2.656	2.94	-0.500	-2.751	-2.083
1.61	-0.248	-1.684	-1.018	2.28	-0.740	-2.509	-2.736	2.95	-0.499	-2.748	-2.069
1.62	-0.250	-1.691	-1.031	2.29	-0.791	-2.541	-2.824	2.96	-0.498	-2.744	-2.054
1.63	-0.252	-1.698	-1.044	2.30	-0.853	-2.577	-2.920	2.97	-0.497	-2.737	-2.041
1.64	-0.254	-1.703	-1.058	2.31	-0.930	-2.613	-3.025	2.98	-0.496	-2.732	-2.027
1.65	-0.256	-1.713	-1.071	2.32	-1.029	-2.658	-3.142	2.99	-0.495	-2.727	-2.014
1.66	-0.258	-1.718	-1.085	2.33	-1.157	-2.707	-3.271	3.00	-0.495	-2.722	-2.001
1.67	-0.261	-1.725	-1.098	2.34	-1.326	-2.760	-3.412	3.01	-0.494	-2.714	-1.988
1.68	-0.263	-1.732	-1.112	2.35	-1.554	-2.821	-3.569	3.02	-0.493	-2.709	-1.976
1.69	-0.265	-1.743	-1.126	2.36	-1.872	-2.893	-3.740	3.03	-0.492	-2.704	-1.963
1.70	-0.268	-1.750	-1.141	2.37	-2.327	-2.972	-3.927	3.04	-0.491	-2.702	-1.951
1.71	-0.271	-1.756	-1.155	2.38	-2.996	-3.066	-4.130	3.05	-0.491	-2.702	-1.940
1.72	-0.274	-1.762	-1.170	2.39	-4.006	-3.174	-4.347	3.06	-0.490	-2.696	-1.928
1.73	-0.276	-1.771	-1.184	2.40	-5.552	-3.299	-4.574	3.07	-0.489	-2.687	-1.916
1.74	-0.279	-1.778	-1.199	2.41	-7.815	-3.443	-4.807	3.08	-0.488	-2.680	-1.905
1.75	-0.282	-1.784	-1.214	2.42	-10.254	-3.606	-5.038	3.09	-0.486	-2.676	-1.894
1.76	-0.286	-1.792	-1.230	2.43	-10.182	-3.788	-5.255	3.10	-0.485	-2.664	-1.883
1.77	-0.289	-1.799	-1.245	2.44	-7.782	-3.988	-5.446	3.11	-0.484	-2.655	-1.872
1.78	-0.292	-1.807	-1.261	2.45	-5.629	-4.195	-5.596	3.12	-0.482	-2.648	-1.862
1.79	-0.296	-1.816	-1.277	2.46	-4.158	-4.392	-5.692	3.13	-0.480	-2.640	-1.851
1.80	-0.299	-1.822	-1.293	2.47	-3.185	-4.569	-5.726	3.14	-0.478	-2.638	-1.841
1.81	-0.303	-1.831	-1.309	2.48	-2.531	-4.702	-5.695	3.15	-0.476	-2.627	-1.831
1.82	-0.306	-1.841	-1.325	2.49	-2.078	-4.770	-5.603	3.16	-0.474	-2.627	-1.821
1.83	-0.310	-1.851	-1.342	2.50	-1.755	-4.768	-5.460	3.17	-0.471	-2.626	-1.811
1.84	-0.314	-1.861	-1.359	2.51	-1.519	-4.702	-5.279	3.18	-0.468	-2.628	-1.801
1.85	-0.317	-1.873	-1.375	2.52	-1.342	-4.582	-5.075	3.19	-0.465	-2.632	-1.792
1.86	-0.321	-1.881	-1.393	2.53	-1.205	-4.436	-4.859	3.20	-0.462	-2.634	-1.782
1.87	-0.325	-1.891	-1.410	2.54	-1.098	-4.278	-4.643	3.21	-0.458	-2.636	-1.773
1.88	-0.329	-1.901	-1.428	2.55	-1.013	-4.125	-4.432	3.22	-0.455	-2.629	-1.764
1.89	-0.333	-1.910	-1.445	2.56	-0.944	-3.974	-4.232	3.23	-0.451	-2.629	-1.755
1.90	-0.338	-1.920	-1.463	2.57	-0.887	-3.840	-4.045	3.24	-0.446	-2.621	-1.746
1.91	-0.342	-1.932	-1.482	2.58	-0.840	-3.718	-3.873	3.25	-0.442	-2.622	-1.737
1.92	-0.346	-1.942	-1.500	2.59	-0.800	-3.614	-3.716	3.26	-0.437	-2.627	-1.728
1.93	-0.351	-1.951	-1.519	2.60	-0.766	-3.522	-3.573	3.27	-0.432	-2.633	-1.720
1.94	-0.355	-1.963	-1.538	2.61	-0.737	-3.443	-3.444	3.28	-0.427	-2.639	-1.711
1.95	-0.360	-1.972	-1.558	2.62	-0.712	-3.376	-3.327	3.29	-0.422	-2.640	-1.703
1.96	-0.364	-1.982	-1.577	2.63	-0.690	-3.313	-3.221	3.30	-0.416	-2.640	-1.695
1.97	-0.369	-1.993	-1.597	2.64	-0.671	-3.261	-3.126	3.31	-0.411	-2.643	-1.687
1.98	-0.374	-2.004	-1.618	2.65	-0.654	-3.215	-3.039	3.32	-0.405	-2.649	-1.679
1.99	-0.379	-2.015	-1.638	2.66	-0.639	-3.175	-2.961	3.33	-0.399	-2.649	-1.671
2.00	-0.384	-2.027	-1.659	2.67	-0.625	-3.138	-2.890	3.34	-0.394	-2.651	-1.663
2.01	-0.389	-2.038	-1.681	2.68	-0.613	-3.104	-2.825	3.35	-0.388	-2.643	-1.656
2.02	-0.394	-2.050	-1.703	2.69	-0.603	-3.075	-2.766	3.36	-0.382	-2.646	-1.649
2.03	-0.399	-2.062	-1.725	2.70	-0.593	-3.047	-2.712	3.37	-0.376	-2.654	-1.641
2.04	-0.405	-2.076	-1.748	2.71	-0.584	-3.019	-2.662	3.38	-0.370	-2.656	-1.634
2.05	-0.410	-2.091	-1.772	2.72	-0.576	-3.001	-2.616	3.39	-0.364	-2.663	-1.627
2.06	-0.416	-2.101	-1.796	2.73	-0.568	-2.981	-2.574	3.40	-0.358	-2.666	-1.620
2.07	-0.422	-2.114	-1.821	2.74	-0.561	-2.962	-2.535	3.41	-0.353	-2.677	-1.614
2.08	-0.428	-2.127	-1.846	2.75	-0.555	-2.944	-2.499	3.42	-0.348	-2.683	-1.607
2.09	-0.435	-2.140	-1.873	2.76	-0.550	-2.929	-2.465	3.43	-0.342	-2.699	-1.601
2.10	-0.441	-2.154	-1.900	2.77	-0.544	-2.912	-2.433	3.44	-0.337	-2.704	-1.594
2.11	-0.448	-2.168	-1.928	2.78	-0.540	-2.900	-2.403	3.45	-0.333	-2.711	-1.588
2.12	-0.456	-2.183	-1.957	2.79	-0.535	-2.888	-2.376	3.46	-0.328	-2.716	-1.582
2.13	-0.464	-2.198	-1.988	2.80	-0.531	-2.876	-2.349	3.47	-0.324	-2.720	-1.576
2.14	-0.472	-2.213	-2.019	2.81	-0.528	-2.865	-2.324	3.48	-0.321	-2.736	-1.571
2.15	-0.481	-2.227	-2.053	2.82	-0.524	-2.850	-2.301	3.49	-0.317	-2.745	-1.565
2.16	-0.490	-2.242	-2.088	2.83	-0.521	-2.839	-2.278	3.50	-0.314	-2.764	-1.560

Appendix G. Print designs for Experiment (III)

The print designs used for the antenna fabrication are shown below.

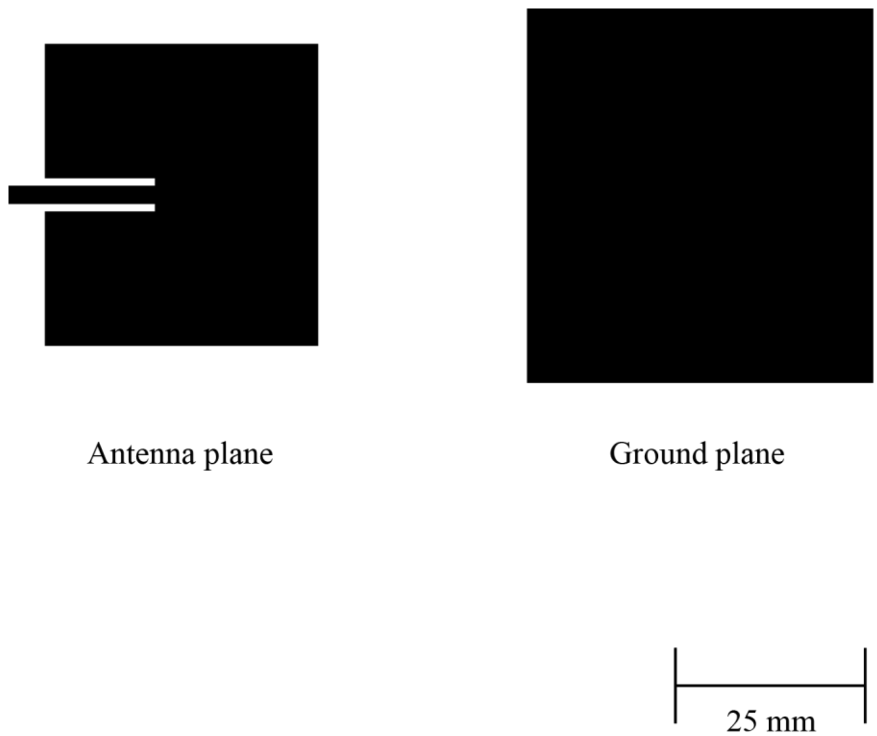

Appendix H. Simulation results for Experiment (III)

Simulated S_{11}.

Frequency (GHz)	S_{11} (dB) of S-antenna	S_{11} (dB) of D-antenna	S_{11} (dB) of DG-antenna	Frequency (GHz)	S_{11} (dB) of S-antenna	S_{11} (dB) of D-antenna	S_{11} (dB) of DG-antenna	Frequency (GHz)	S_{11} (dB) of S-antenna	S_{11} (dB) of D-antenna	S_{11} (dB) of DG-antenna
1.50	-0.145	-0.144	-0.120	2.17	-0.404	-0.397	-0.370	2.84	-0.222	-0.229	-0.271
1.51	-0.148	-0.146	-0.122	2.18	-0.409	-0.402	-0.376	2.85	-0.218	-0.225	-0.267
1.52	-0.150	-0.148	-0.124	2.19	-0.414	-0.406	-0.382	2.86	-0.214	-0.221	-0.262
1.53	-0.153	-0.151	-0.126	2.20	-0.418	-0.411	-0.388	2.87	-0.210	-0.217	-0.258
1.54	-0.155	-0.153	-0.128	2.21	-0.423	-0.416	-0.395	2.88	-0.207	-0.213	-0.254
1.55	-0.158	-0.155	-0.130	2.22	-0.428	-0.422	-0.402	2.89	-0.203	-0.210	-0.251
1.56	-0.160	-0.158	-0.132	2.23	-0.433	-0.427	-0.409	2.90	-0.200	-0.206	-0.247
1.57	-0.163	-0.160	-0.134	2.24	-0.439	-0.433	-0.416	2.91	-0.197	-0.203	-0.243
1.58	-0.165	-0.162	-0.136	2.25	-0.444	-0.439	-0.424	2.92	-0.194	-0.200	-0.239
1.59	-0.168	-0.165	-0.138	2.26	-0.450	-0.445	-0.433	2.93	-0.191	-0.196	-0.236
1.60	-0.171	-0.168	-0.141	2.27	-0.457	-0.452	-0.442	2.94	-0.188	-0.193	-0.233
1.61	-0.174	-0.170	-0.143	2.28	-0.464	-0.460	-0.452	2.95	-0.185	-0.190	-0.229
1.62	-0.177	-0.173	-0.145	2.29	-0.472	-0.468	-0.463	2.96	-0.182	-0.187	-0.226
1.63	-0.179	-0.176	-0.148	2.30	-0.482	-0.478	-0.476	2.97	-0.179	-0.185	-0.223
1.64	-0.182	-0.178	-0.150	2.31	-0.492	-0.490	-0.490	2.98	-0.177	-0.182	-0.220
1.65	-0.185	-0.181	-0.153	2.32	-0.505	-0.503	-0.507	2.99	-0.174	-0.179	-0.217
1.66	-0.188	-0.184	-0.155	2.33	-0.520	-0.519	-0.526	3.00	-0.172	-0.177	-0.214
1.67	-0.191	-0.187	-0.158	2.34	-0.538	-0.538	-0.549	3.01	-0.169	-0.174	-0.211
1.68	-0.195	-0.190	-0.160	2.35	-0.561	-0.561	-0.578	3.02	-0.167	-0.172	-0.208
1.69	-0.198	-0.193	-0.163	2.36	-0.590	-0.591	-0.613	3.03	-0.165	-0.169	-0.205
1.70	-0.201	-0.196	-0.166	2.37	-0.626	-0.628	-0.658	3.04	-0.163	-0.167	-0.203
1.71	-0.204	-0.200	-0.169	2.38	-0.675	-0.678	-0.717	3.05	-0.161	-0.165	-0.200
1.72	-0.208	-0.203	-0.172	2.39	-0.741	-0.744	-0.797	3.06	-0.159	-0.163	-0.198
1.73	-0.211	-0.206	-0.174	2.40	-0.833	-0.836	-0.909	3.07	-0.157	-0.161	-0.195
1.74	-0.214	-0.209	-0.177	2.41	-0.966	-0.969	-1.072	3.08	-0.155	-0.159	-0.193
1.75	-0.218	-0.213	-0.181	2.42	-1.169	-1.167	-1.322	3.09	-0.153	-0.157	-0.190
1.76	-0.222	-0.216	-0.184	2.43	-1.497	-1.483	-1.731	3.10	-0.151	-0.155	-0.188
1.77	-0.225	-0.220	-0.187	2.44	-2.064	-2.020	-2.453	3.11	-0.149	-0.153	-0.186
1.78	-0.229	-0.224	-0.190	2.45	-3.139	-3.017	-3.854	3.12	-0.148	-0.151	-0.184
1.79	-0.233	-0.227	-0.193	2.46	-5.381	-5.065	-6.860	3.13	-0.146	-0.149	-0.182
1.80	-0.236	-0.231	-0.197	2.47	-10.010	-9.576	-12.632	3.14	-0.145	-0.147	-0.179
1.81	-0.240	-0.235	-0.200	2.48	-10.367	-12.474	-9.438	3.15	-0.143	-0.146	-0.177
1.82	-0.244	-0.239	-0.204	2.49	-5.539	-6.644	-4.966	3.16	-0.142	-0.144	-0.176
1.83	-0.248	-0.243	-0.207	2.50	-3.153	-3.675	-2.937	3.17	-0.140	-0.143	-0.174
1.84	-0.252	-0.247	-0.211	2.51	-2.021	-2.298	-1.949	3.18	-0.139	-0.141	-0.172
1.85	-0.256	-0.251	-0.215	2.52	-1.430	-1.593	-1.418	3.19	-0.137	-0.140	-0.170
1.86	-0.261	-0.255	-0.219	2.53	-1.091	-1.195	-1.106	3.20	-0.136	-0.138	-0.168
1.87	-0.265	-0.259	-0.222	2.54	-0.881	-0.952	-0.909	3.21	-0.135	-0.137	-0.167
1.88	-0.269	-0.263	-0.226	2.55	-0.742	-0.793	-0.777	3.22	-0.134	-0.135	-0.165
1.89	-0.273	-0.267	-0.230	2.56	-0.646	-0.684	-0.685	3.23	-0.133	-0.134	-0.163
1.90	-0.278	-0.272	-0.234	2.57	-0.576	-0.606	-0.618	3.24	-0.131	-0.133	-0.162
1.91	-0.282	-0.276	-0.239	2.58	-0.524	-0.548	-0.567	3.25	-0.130	-0.132	-0.160
1.92	-0.287	-0.280	-0.243	2.59	-0.483	-0.503	-0.528	3.26	-0.129	-0.130	-0.159
1.93	-0.291	-0.285	-0.247	2.60	-0.450	-0.467	-0.496	3.27	-0.128	-0.129	-0.157
1.94	-0.296	-0.289	-0.251	2.61	-0.424	-0.438	-0.470	3.28	-0.127	-0.128	-0.156
1.95	-0.300	-0.294	-0.256	2.62	-0.402	-0.415	-0.449	3.29	-0.126	-0.127	-0.155
1.96	-0.305	-0.298	-0.260	2.63	-0.383	-0.395	-0.431	3.30	-0.125	-0.126	-0.153
1.97	-0.310	-0.303	-0.265	2.64	-0.367	-0.378	-0.415	3.31	-0.124	-0.125	-0.152
1.98	-0.314	-0.308	-0.270	2.65	-0.353	-0.363	-0.402	3.32	-0.123	-0.124	-0.151
1.99	-0.319	-0.312	-0.274	2.66	-0.340	-0.350	-0.389	3.33	-0.122	-0.123	-0.150
2.00	-0.324	-0.317	-0.279	2.67	-0.329	-0.338	-0.379	3.34	-0.122	-0.122	-0.148
2.01	-0.329	-0.322	-0.284	2.68	-0.319	-0.327	-0.369	3.35	-0.121	-0.121	-0.147
2.02	-0.334	-0.326	-0.289	2.69	-0.310	-0.318	-0.360	3.36	-0.120	-0.120	-0.146
2.03	-0.338	-0.331	-0.294	2.70	-0.301	-0.309	-0.351	3.37	-0.119	-0.119	-0.145
2.04	-0.343	-0.336	-0.299	2.71	-0.293	-0.301	-0.344	3.38	-0.118	-0.119	-0.144
2.05	-0.348	-0.340	-0.304	2.72	-0.286	-0.293	-0.336	3.39	-0.117	-0.118	-0.143
2.06	-0.353	-0.345	-0.309	2.73	-0.279	-0.286	-0.329	3.40	-0.116	-0.117	-0.142
2.07	-0.357	-0.350	-0.314	2.74	-0.273	-0.280	-0.323	3.41	-0.116	-0.117	-0.141
2.08	-0.362	-0.354	-0.319	2.75	-0.266	-0.273	-0.317	3.42	-0.115	-0.116	-0.141
2.09	-0.367	-0.359	-0.325	2.76	-0.261	-0.267	-0.311	3.43	-0.114	-0.115	-0.140
2.10	-0.372	-0.364	-0.330	2.77	-0.255	-0.262	-0.305	3.44	-0.113	-0.115	-0.139
2.11	-0.376	-0.369	-0.335	2.78	-0.250	-0.256	-0.300	3.45	-0.112	-0.114	-0.138
2.12	-0.381	-0.373	-0.341	2.79	-0.245	-0.251	-0.295	3.46	-0.111	-0.113	-0.137
2.13	-0.386	-0.378	-0.346	2.80	-0.240	-0.246	-0.290	3.47	-0.111	-0.113	-0.137
2.14	-0.390	-0.383	-0.352	2.81	-0.235	-0.242	-0.285	3.48	-0.110	-0.112	-0.136
2.15	-0.395	-0.387	-0.358	2.82	-0.231	-0.237	-0.280	3.49	-0.109	-0.112	-0.135
2.16	-0.400	-0.392	-0.364	2.83	-0.226	-0.233	-0.275	3.50	-0.108	-0.111	-0.135

Appendix I. Measurement results for Experiment (III)

Measured S_{11}.

Frequency (GHz)	S_{11} (dB) of S-antenna	S_{11} (dB) of D-antenna	S_{11} (dB) of DG-antenna	Frequency (GHz)	S_{11} (dB) of S-antenna	S_{11} (dB) of D-antenna	S_{11} (dB) of DG-antenna	Frequency (GHz)	S_{11} (dB) of S-antenna	S_{11} (dB) of D-antenna	S_{11} (dB) of DG-antenna
1.50	-1.021	-0.981	-1.177	2.17	-2.305	-3.387	-3.031	2.84	-2.828	-2.702	-3.144
1.51	-1.029	-0.994	-1.189	2.18	-2.341	-3.470	-3.084	2.85	-2.792	-2.666	-3.100
1.52	-1.037	-1.009	-1.201	2.19	-2.381	-3.558	-3.139	2.86	-2.758	-2.632	-3.059
1.53	-1.045	-1.025	-1.214	2.20	-2.420	-3.653	-3.195	2.87	-2.724	-2.600	-3.020
1.54	-1.054	-1.039	-1.224	2.21	-2.461	-3.758	-3.255	2.88	-2.690	-2.565	-2.979
1.55	-1.062	-1.055	-1.237	2.22	-2.504	-3.867	-3.315	2.89	-2.654	-2.532	-2.938
1.56	-1.070	-1.068	-1.249	2.23	-2.548	-3.989	-3.377	2.90	-2.620	-2.500	-2.899
1.57	-1.081	-1.084	-1.262	2.24	-2.593	-4.118	-3.443	2.91	-2.585	-2.466	-2.861
1.58	-1.090	-1.100	-1.276	2.25	-2.641	-4.260	-3.511	2.92	-2.554	-2.437	-2.828
1.59	-1.101	-1.117	-1.290	2.26	-2.689	-4.415	-3.580	2.93	-2.521	-2.406	-2.789
1.60	-1.109	-1.135	-1.303	2.27	-2.743	-4.584	-3.656	2.94	-2.490	-2.372	-2.751
1.61	-1.120	-1.151	-1.316	2.28	-2.796	-4.759	-3.735	2.95	-2.457	-2.342	-2.714
1.62	-1.130	-1.170	-1.331	2.29	-2.853	-4.939	-3.820	2.96	-2.422	-2.312	-2.678
1.63	-1.139	-1.188	-1.345	2.30	-2.911	-5.113	-3.909	2.97	-2.388	-2.284	-2.640
1.64	-1.152	-1.207	-1.361	2.31	-2.975	-5.276	-4.004	2.98	-2.355	-2.255	-2.605
1.65	-1.162	-1.227	-1.377	2.32	-3.042	-5.408	-4.105	2.99	-2.324	-2.230	-2.573
1.66	-1.172	-1.248	-1.393	2.33	-3.114	-5.503	-4.216	3.00	-2.292	-2.201	-2.540
1.67	-1.183	-1.267	-1.407	2.34	-3.189	-5.544	-4.336	3.01	-2.259	-2.172	-2.505
1.68	-1.194	-1.290	-1.425	2.35	-3.273	-5.535	-4.465	3.02	-2.230	-2.145	-2.472
1.69	-1.206	-1.312	-1.442	2.36	-3.362	-5.474	-4.604	3.03	-2.198	-2.118	-2.439
1.70	-1.218	-1.335	-1.460	2.37	-3.461	-5.382	-4.753	3.04	-2.168	-2.095	-2.408
1.71	-1.232	-1.359	-1.478	2.38	-3.570	-5.262	-4.911	3.05	-2.138	-2.067	-2.377
1.72	-1.245	-1.381	-1.497	2.39	-3.693	-5.134	-5.072	3.06	-2.110	-2.043	-2.346
1.73	-1.258	-1.405	-1.517	2.40	-3.827	-5.005	-5.233	3.07	-2.082	-2.018	-2.318
1.74	-1.269	-1.428	-1.534	2.41	-3.978	-4.878	-5.386	3.08	-2.058	-1.995	-2.290
1.75	-1.286	-1.455	-1.557	2.42	-4.145	-4.761	-5.517	3.09	-2.030	-1.970	-2.262
1.76	-1.300	-1.480	-1.577	2.43	-4.321	-4.653	-5.616	3.10	-2.003	-1.948	-2.233
1.77	-1.314	-1.506	-1.598	2.44	-4.509	-4.552	-5.674	3.11	-1.977	-1.926	-2.205
1.78	-1.330	-1.533	-1.619	2.45	-4.699	-4.461	-5.685	3.12	-1.951	-1.904	-2.178
1.79	-1.346	-1.562	-1.641	2.46	-4.878	-4.380	-5.651	3.13	-1.925	-1.885	-2.153
1.80	-1.360	-1.589	-1.664	2.47	-5.022	-4.304	-5.576	3.14	-1.900	-1.864	-2.127
1.81	-1.376	-1.620	-1.688	2.48	-5.122	-4.236	-5.475	3.15	-1.875	-1.843	-2.100
1.82	-1.393	-1.651	-1.712	2.49	-5.161	-4.172	-5.358	3.16	-1.853	-1.822	-2.074
1.83	-1.411	-1.682	-1.737	2.50	-5.137	-4.114	-5.234	3.17	-1.829	-1.800	-2.044
1.84	-1.429	-1.715	-1.763	2.51	-5.060	-4.060	-5.110	3.18	-1.803	-1.779	-2.018
1.85	-1.446	-1.747	-1.789	2.52	-4.944	-4.010	-4.992	3.19	-1.781	-1.758	-1.996
1.86	-1.466	-1.783	-1.818	2.53	-4.799	-3.961	-4.881	3.20	-1.760	-1.740	-1.973
1.87	-1.484	-1.817	-1.844	2.54	-4.646	-3.910	-4.777	3.21	-1.740	-1.717	-1.952
1.88	-1.503	-1.851	-1.871	2.55	-4.497	-3.864	-4.682	3.22	-1.720	-1.699	-1.927
1.89	-1.521	-1.888	-1.901	2.56	-4.355	-3.819	-4.595	3.23	-1.700	-1.683	-1.902
1.90	-1.541	-1.925	-1.929	2.57	-4.226	-3.774	-4.514	3.24	-1.679	-1.668	-1.882
1.91	-1.561	-1.962	-1.959	2.58	-4.111	-3.730	-4.439	3.25	-1.659	-1.655	-1.859
1.92	-1.582	-2.001	-1.990	2.59	-4.009	-3.684	-4.367	3.26	-1.642	-1.640	-1.837
1.93	-1.604	-2.041	-2.021	2.60	-3.919	-3.642	-4.302	3.27	-1.625	-1.626	-1.818
1.94	-1.625	-2.081	-2.052	2.61	-3.837	-3.598	-4.240	3.28	-1.606	-1.612	-1.802
1.95	-1.647	-2.122	-2.086	2.62	-3.763	-3.555	-4.177	3.29	-1.587	-1.599	-1.783
1.96	-1.670	-2.164	-2.118	2.63	-3.699	-3.515	-4.119	3.30	-1.570	-1.586	-1.765
1.97	-1.694	-2.208	-2.151	2.64	-3.639	-3.472	-4.062	3.31	-1.552	-1.574	-1.749
1.98	-1.717	-2.252	-2.187	2.65	-3.583	-3.429	-4.008	3.32	-1.533	-1.561	-1.730
1.99	-1.742	-2.298	-2.223	2.66	-3.532	-3.388	-3.957	3.33	-1.516	-1.548	-1.715
2.00	-1.766	-2.345	-2.259	2.67	-3.485	-3.347	-3.905	3.34	-1.498	-1.538	-1.700
2.01	-1.793	-2.395	-2.298	2.68	-3.438	-3.306	-3.856	3.35	-1.483	-1.525	-1.686
2.02	-1.818	-2.444	-2.337	2.69	-3.393	-3.264	-3.807	3.36	-1.469	-1.514	-1.670
2.03	-1.846	-2.496	-2.376	2.70	-3.350	-3.223	-3.757	3.37	-1.454	-1.501	-1.652
2.04	-1.875	-2.549	-2.419	2.71	-3.311	-3.182	-3.710	3.38	-1.442	-1.491	-1.636
2.05	-1.903	-2.603	-2.460	2.72	-3.269	-3.143	-3.664	3.39	-1.431	-1.480	-1.619
2.06	-1.932	-2.657	-2.503	2.73	-3.233	-3.103	-3.618	3.40	-1.417	-1.468	-1.602
2.07	-1.963	-2.715	-2.547	2.74	-3.193	-3.063	-3.572	3.41	-1.403	-1.456	-1.588
2.08	-1.994	-2.771	-2.590	2.75	-3.158	-3.028	-3.529	3.42	-1.389	-1.444	-1.572
2.09	-2.026	-2.832	-2.636	2.76	-3.119	-2.988	-3.483	3.43	-1.376	-1.433	-1.561
2.10	-2.058	-2.894	-2.683	2.77	-3.081	-2.951	-3.441	3.44	-1.363	-1.424	-1.549
2.11	-2.091	-2.956	-2.730	2.78	-3.044	-2.916	-3.399	3.45	-1.351	-1.417	-1.536
2.12	-2.124	-3.021	-2.777	2.79	-3.007	-2.880	-3.354	3.46	-1.340	-1.409	-1.524
2.13	-2.159	-3.089	-2.828	2.80	-2.971	-2.843	-3.311	3.47	-1.331	-1.401	-1.511
2.14	-2.194	-3.158	-2.877	2.81	-2.935	-2.806	-3.268	3.48	-1.321	-1.393	-1.497
2.15	-2.230	-3.231	-2.926	2.82	-2.900	-2.772	-3.228	3.49	-1.308	-1.385	-1.486
2.16	-2.267	-3.307	-2.977	2.83	-2.864	-2.736	-3.185	3.50	-1.301	-1.378	-1.474